

Titre: Passive Aeroelastic Control of Aircraft Wings Via Nonlinear
Title: Oscillators

Auteur: Claudia Fernandez Escudero
Author:

Date: 2021

Type: Mémoire ou thèse / Dissertation or Thesis

Référence: Fernandez Escudero, C. (2021). Passive Aeroelastic Control of Aircraft Wings Via
Citation: Nonlinear Oscillators [Thèse de doctorat, Polytechnique Montréal]. PolyPublie.
<https://publications.polymtl.ca/6578/>

 **Document en libre accès dans PolyPublie**
Open Access document in PolyPublie

URL de PolyPublie: <https://publications.polymtl.ca/6578/>
PolyPublie URL:

**Directeurs de
recherche:** Annie Ross, Guilhem Michon, & Éric Laurendeau
Advisors:

Programme: Génie mécanique
Program:

POLYTECHNIQUE MONTRÉAL

affiliée à l'Université de Montréal

ET

Institut supérieur de l'aéronautique et de l'espace

affiliée à l'Université de Toulouse

Passive aeroelastic control of aircraft wings via nonlinear oscillators

CLAUDIA FERNANDEZ ESCUDERO

Département de génie mécanique

Thèse présentée en vue de l'obtention du diplôme de Philosophiae Doctor

Génie mécanique

Mai 2021

POLYTECHNIQUE MONTRÉAL

affiliée à l'Université de Montréal

ET

Institut supérieur de l'aéronautique et de l'espace

affiliée à l'Université de Toulouse

Cette thèse intitulée:

Passive aeroelastic control of aircraft wings via nonlinear oscillators

présentée par **Claudia FERNANDEZ ESCUDERO**

en vue de l'obtention du diplôme de Philosophiae Doctor

a été dûment acceptée pour une thèse par le jury d'examen constitué de :

Frédéric GOSSELIN, président

Annie ROSS, membre et directrice de recherche

Guilhem MICHON, membre et codirecteur de recherche

Eric LAURENDEAU, membre et codirecteur de recherche

Emmanuel DE LANGRE, membre

Grigorios DIMITRIADIS, membre externe

« Jump and you will find out how to unfold your wings as you fall »

-Ray Bradbury

ACKNOWLEDGEMENTS

The research work presented in this thesis is the result of a double degree program from ISAE-Supaero in France and Polytechnique Montreal. The work was financially supported by the Natural Sciences and Engineering Research Council of Canada, the Canada Research Chair program, the French Initiative d'Excellence (IDEX) and the Université de Toulouse.

I would like to start by expressing my gratitude to my four co-directors: Sébastien Prothin, Guilhem Michon, Eric Laurendeau and Annie Ross. Thank you for your support and guidance during these years and for the trust and encouragement you have given me.

This thesis would have not been possible without the expertise of the technical team at ISAE-Supaero and ICA. Special thanks to Rémy Chanton, Henri Dedieu, Jean-Benoît Alibet and Leonardo Sanches. In the same way, I would like to express my gratitude to the students of Eric Laurendeau's Lab for their advice concerning numerical analysis. Thank you Fred, Simon, Matthieu, Réda, Vincent and the rest and special thank you to Miguel Gagnon, with whom I had the great pleasure of working for some months, for his valuable help.

Thank you to the PhD students at ISAE-Supaero with whom I shared this adventure, for the good ambiance, the laughs, the debates...Some of you have become close friends and I am very grateful for this. Big thanks to Marta M., Victoria, Marta R., Anaïs, Yuchen, Nikola and all the rest. I would also like to thank the great friends I made in Montréal: Jesus, Antonio, Léa, Delphine, Raquel and Yao for becoming my overseas family and helping me survive my coldest of winters and my numerous "demenagements". To my friends in Spain for always sticking around through the ups and downs, thank you Elisa, Anita, Helena, Ying, Gabri, Kike and to my friends in Toulouse for all the good moments, thank you Sergio, Roberto, Mauro, Pablo, Pili...

To my parents Raquel and Hector and to my sister Carlota, I could write another thesis on how much I love and admire you and how much you have helped me, not only this time but every time. Let me try to summarize: *Gracias, gracias por tanto, ¡lo conseguimos!*

Last but not least, thank you Ekhi for your love and your endless encouragement. I am forever grateful to have crossed your path and to get to walk by your side. *Mila esker, maite zaitut.*

RÉSUMÉ

Les phénomènes aéroélastiques ont lieu lorsqu'une structure interagit avec un écoulement qui l'entoure et ils sont une des principaux facteurs qui limitent l'enveloppe de vol des avions. Cette interaction fluide-structure peut entraîner de l'endommagement structurel, immédiat ou dû à la fatigue. Depuis le début de l'histoire aéronautique, l'aéroélasticité a toujours été un facteur important dans la conception des avions. De nos jours, les progrès de l'industrie aéronautique conduisent à la conception d'ailes plus efficaces, présentant généralement des géométries plus allongées et l'utilisation de matériaux plus légers et plus flexibles. Ces nouvelles ailes sont plus sujettes que jamais à un comportement aéroélastique, ce qui signifie que le contrôle aéroélastique reste un domaine d'étude important. De plus, les nouveaux designs des drones peuvent poser de grands défis en termes d'aéroélasticité.

L'objectif de ce travail est de présenter, analyser et tester une solution innovante qui contrôle le comportement aéroélastique d'une aile d'avion pour des conditions de vol plus sûres et/ou une enveloppe de vol élargie. La solution présentée est basée sur des absorbeurs secondaires utilisés sur d'autres applications, comme les ponts suspendus. Les absorbeurs secondaires sont des systèmes masse-ressort-amortisseurs qui sont rattachés au système principal afin de modifier son comportement dynamique. Ce système de contrôle est passif, ce qui signifie qu'aucun apport d'énergie externe n'est requis. Le système présenté est intégré dans l'aile, à l'intérieur d'un volet qui oscille librement dans l'écoulement. Les avantages de ce volet sont que l'oscillateur secondaire est placé dans l'écoulement pour bénéficier d'un amortissement aérodynamique et qu'il ajoute une masse négligeable, ce qui est toujours une priorité en aéronautique. Le système de contrôle peut présenter une rigidité non linéaire le rendant efficace sur une plus large plage de fréquences. C'est une caractéristique importante, car les fréquences de l'aile évoluent avec la vitesse du vent.

Afin de valider ce dispositif de contrôle innovant dans le domaine complexe de l'aéroélasticité non linéaire, une double approche est suivie utilisant à la fois l'analyse expérimentale et des simulations numériques. Concernant l'approche expérimentale, deux bancs d'essai sont créés et testés en soufflerie: une aile bidimensionnelle et une aile tridimensionnelle.

Le premier banc expérimental consiste en une configuration d'aile bidimensionnelle à deux degrés de liberté, avec un volet qui peut être bloqué ou débloqué comme troisième degré de

liberté, agissant comme oscillateur secondaire. Cette maquette permet de réaliser une preuve de concept du système de contrôle et met en évidence les avantages des caractéristiques non linéaires par rapport à une version linéaire. On observe que l'aile bidimensionnelle présente du flottement classique par coalescence de ses deux modes structuraux. Lorsque le système de contrôle est débloqué, la vitesse de flottement augmente, élargissant ainsi l'enveloppe de vol. De plus, le système de contrôle montre de bonnes performances de mitigation des vibrations pendant le régime post-flottement, en particulier lorsqu'il est équipé d'une rigidité non linéaire.

Le deuxième banc expérimental consiste en une configuration d'aile élastique tridimensionnelle, encastrée à une extrémité et libre à l'autre extrémité. De manière similaire au premier banc d'essai, l'aile a un volet qui peut être bloqué ou débloqué et équipé du système de contrôle passif. Cette fois-ci le volet a un effet plus localisé et donc plus réaliste. L'objectif de la configuration est de faire une deuxième preuve de concept du système de contrôle, mais cette fois en tenant compte des effets structurels et aérodynamiques tridimensionnels. Les caractéristiques non linéaires, avantageuses dans la preuve de concept précédente sont retenues pour le dispositif de contrôle. L'aile tridimensionnelle présente des « vortex induced vibration » (vibration induite par tourbillon) et la mitigation des vibrations a été observée en débloquent le dispositif de commande. L'importance du dimensionnement est démontrée en faisant varier les paramètres du volet de contrôle.

Le besoin de réaliser une optimisation paramétrique du dispositif de contrôle fait des simulations numériques un atout majeur. Tout d'abord, différentes méthodes numériques ont été comparées afin d'identifier leur capacité à capturer le comportement aéroélastique non linéaire complexe d'une aile bidimensionnelle. À cela s'est rajoutée une évaluation du temps et du coût de calcul. Pour cela, quatre méthodes différentes sont adaptées aux cas tests sélectionnés de la littérature. Les méthodes vont du code analytique basé sur le modèle de Theodorsen à basse fidélité, aux codes « computer fluid dynamics » de haute-fidélité couplée avec un maillage mobile avec les méthodes Euler et « unsteady Reynolds averaged Navier-Stokes » (moyenne de Reynolds). Une méthode de fidélité moyenne, « unsteady vortex lattice method », est également sélectionnée pour fin de comparaison. Les méthodes ont toutes montré une bonne concordance pour les cas de test sélectionnés et les méthodes de fidélité inférieure gagnent plusieurs ordres de grandeur en vitesse de calcul par rapport aux méthodes de fidélité plus élevée. Le développement

et la comparaison de ces outils sont une première étape pour compléter la preuve de concept expérimentale du système de contrôle par des simulations numériques.

Dans l'ensemble, le travail présente une nouvelle solution de contrôle innovante et montre son efficacité dans le contrôle aéroélastique des ailes à la fois bidimensionnelles et tridimensionnelles. Les forces et les faiblesses du système de contrôle sont mises en évidence et les outils nécessaires au développement ultérieur du dispositif sont mis en place.

ABSTRACT

Aeroelastic behavior occurs when an elastic structure interacts with a flow surrounding it and is one of the main limiting factors regarding aircraft flight envelopes. This fluid-structure interaction can lead to fatal structural damage either immediate or from fatigue. Since the beginning of aeronautical history, aeroelasticity has always been an important factor in aircraft design. Nowadays, progress in the aeronautics industry is leading to more efficient wing designs, generally featuring more elongated geometries and the use of lighter and more flexible materials. These new designs are more prone than ever to aeroelastic behavior which means that aeroelastic control remains an important area of study. Furthermore, new flying devices such as drones are constantly challenging aeroelasticity.

The objective of this work is to present, analyze and test an innovative solution which controls the aeroelastic behavior of an aircraft wing leading to safer flight conditions and/or to a larger flight envelope. The solution presented is based on secondary absorbers used on other applications, such as suspension bridges. These consist of mass-system-damping elements which are attached to the original system in order to alter its dynamic behavior. The control system is passive, meaning no external energy input is required. The system is integrated in the wing by means of a flap which will oscillate freely in the flow. The advantages of this flap are that the secondary oscillator is placed in the flow and therefore benefits from aerodynamic damping and adds negligible mass, which is always a priority in aeronautics. The control system can feature a nonlinear stiffness making it efficient at a larger range of frequencies. This is an important feature as the wing's frequencies will evolve with changing wind speed.

In order to validate this innovative control device within the complex field of nonlinear aeroelasticity, a double approach is followed using both experimental analysis and numerical simulations. Regarding the experimental approach, two test benches are created and tested in the wind tunnel: a bidimensional and a tridimensional wing.

The first experimental setup consists of a bidimensional wing setup with 2 degrees of freedom with a flap which can be blocked or unblocked as the third degree of freedom acting as the secondary oscillator. This test bench enables a proof of concept of the control system and highlights the advantages of its nonlinear features with respect to a linear version. The

bidimensional wing is observed to present classic flutter by coalescence of its two structural modes. When the control system is unblocked, the flutter speed increases, enlarging the flight envelope. Additionally the control system shows good vibration mitigation performances during the post flutter regime, especially when equipped with nonlinear stiffness.

The second experimental setup consists of a tridimensional elastic wing setup, clamped at one end and free at the other. Similarly to the first test bench, the wing has a flap which can be unblocked and equipped as the passive control system. In this case the flap has a more localized realistic effect which is therefore more realistic. The objective of the setup was to make a second proof of concept of the control system but this time considering tridimensional structural and aerodynamic effects. The nonlinear features, advantageous in the previous proof of concept, are retained for the control device. The tridimensional wing presents vortex induced vibration and vibration mitigation was observed by unblocking the control device. The importance of a correct design was highlighted by varying as some of the parameters in the passive control flap.

The need to carry out parametric optimization of the control device makes numerical simulations a strong asset. First, different numerical methods were compared in order to identify the ability of them to capture complex nonlinear aeroelastic behavior of a bidimensional wing, as well as to assess computational time and cost. For this, four different methods are adapted to literature test cases. The methods range from low fidelity analytic Theodorsen model based code, to higher fidelity CFD codes coupled with a moving mesh with Euler and URANS methods. A medium fidelity method, UVLM, is also selected for comparison. The methods all showed good agreement for the test cases selected and the lower fidelity methods gain several orders of magnitude in computational speed with respect to the higher fidelity methods. The development and comparison of these methods is an important first step to complementing the experimental proof of concepts of the control system with numerical simulations.

Overall, the work presents a new innovative control solution and shows its efficiency in wing aeroelastic control both bidimensional and tridimensional. The strengths and weaknesses of the control system are highlighted and numerical methods for complementary analysis and development and optimization of the device are developed.

TABLE OF CONTENTS

ACKNOWLEDGEMENTS	IV
RÉSUMÉ.....	V
ABSTRACT	VIII
TABLE OF CONTENTS	X
LIST OF TABLES	XIII
LIST OF FIGURES.....	XIV
LIST OF SYMBOLS AND ABBREVIATIONS.....	XVII
LIST OF APPENDICES	XIX
CHAPTER 1 INTRODUCTION.....	1
1.1 Context	1
1.1.1 Aeroelasticity	1
1.1.2 Dynamic aeroelastic phenomena.....	3
1.2 Experimental Control and Vibration Mitigation Systems.....	6
1.2.1 Active aeroelastic control.....	7
1.2.2 Passive Aeroelastic Control	8
1.3 Numerical Methods for Aeroelasticity	11
1.3.1 Equations of motion	12
1.3.2 Theodorsen model	14
1.3.3 Boundary element methods.....	15
1.3.4 Volumetric methods	16
1.4 Research objectives	20
1.5 Methodology	21

1.6	Outline.....	23
CHAPTER 2 ARTICLE 1: NONLINEAR FLAP FOR PASSIVE FLUTTER CONTROL OF BIDIMENSIONAL WING		
		25
2.1	Introduction.....	26
2.2	Experimental setup.....	29
2.2.1	Wind tunnel.....	30
2.2.2	2D wind setup.....	30
2.2.3	Flap.....	32
2.2.4	Instrumentation.....	34
2.3	Results.....	35
2.3.1	Zero wind speed	36
2.3.2	Varying wind speed.....	38
2.4	Conclusion.....	45
CHAPTER 3 ARTICLE 2: PASSIVE CONTROL OF VORTEX INDUCED VIBRATION IN FLEXIBLE WING USING NONLINEAR FLAP		
		47
3.1	Introduction.....	48
3.2	Flap-NES.....	50
3.3	Experiments.....	53
3.3.1	3D Flexible Wing Set-up.....	53
3.3.2	Instrumentation.....	54
3.3.3	Wing Mass Distributions.....	54
3.3.4	Flap-NES Configurations.....	56
3.3.5	Ground vibration tests	57
3.3.6	Wind tunnel testing	58

3.4	Results	59
3.4.1	Ground vibration tests	59
3.4.2	Wind tunnel tests	62
3.4.3	Conclusion.....	65
CHAPTER 4	ARTICLE 3: COMPARISON OF LOW, MEDIUM AND HIGH FIDELITY NUMERICAL METHODS FOR UNSTEADY AERODYNAMICS AND NONLINEAR AEROELASTICITY	67
4.1	Introduction	69
4.2	Structural Model.....	71
4.3	Aerodynamic Models	73
4.3.1	Theodorsen approach	73
4.3.2	UVLM.....	74
4.3.3	Computation time.....	76
4.4	Unsteady Aerodynamics	77
4.5	Linear Aeroelasticity.....	79
4.6	Non-Linear Aeroelasticity.....	85
4.7	Conclusion.....	91
CHAPTER 5	GENERAL DISCUSSION.....	92
CHAPTER 6	CONCLUSION AND PERSPECTIVE	94
APPENDICES	95

LIST OF TABLES

Table 1.1 : Assumptions in the CFD models	19
Table 2.1 : Actual sensitivity of sensors in 2D wing	35
Table 2.2 : Natural frequencies and damping coefficient of each individual DOF.....	37
Table 2.3 : Range of wind speeds in which flutter speed (U_F) appears for different wing configurations.....	39
Table 3.1 : Different mass configurations.....	56
Table 3.2 : Springs used in flap-NES	57
Table 3.3 : GVT wing modes for three mass configurations with blocked NES	60
Table 4.1 : Approximate computation time for each method	77
Table 4.2 : Steady aerodynamic coefficient	78
Table 4.3 : Values of parameters for test cases	80
Table 4.4 : Comparison of dimensionless flutter velocities for the 2DOF linear case	82
Table 4.5 : Comparison of linear flutter velocities for the 3DOF linear case	84

LIST OF FIGURES

Figure 1.1 : Collar’s Triangle	2
Figure 1.2 : Examples of the recent aeroelastic challenges.....	3
Figure 1.3 : 2DOF typical aeroelastic section	4
Figure 1.4 : Frequency and damping against wind speed for a system presenting classic flutter....	4
Figure 1.5 : Nonlinear aeroelastic systems a) supercritical bifurcation (soft flutter) b) subcritical bifurcation (hard flutter).....	6
Figure 1.6 : Nonlinear aeroelastic system control a) supercritical bifurcation (soft flutter) b) subcritical bifurcation (hard flutter)	7
Figure 1.7 : Schematic representation of a system with a secondary absorber	9
Figure 1.8 : Hardening cubic stiffness force	10
Figure 1.9 : Amplitude pulsation diagram of a linear oscillator of 1 DOF.....	10
Figure 1.10 : General mass spring system with resulting cubic stiffness schema	11
Figure 1.11 : Typical aeroelastic sections a) 2DOF b) 3DOF.....	12
Figure 1.12 : Flat plate section used in original Theodorsen model	14
Figure 1.13 : UVLM airfoil discretization with free wake	15
Figure 1.14 : Aircraft wing with NES schema	20
Figure 1.15 : Schematic overview of advances carried out throughout the PhD research work ...	21
Figure 1.16 : CADs of experimental setups a) bidimensional wing b) tridimensional wing.....	22
Figure 2.1: Flap-NES concept in a bidimensional wing, showing the cubic relationship of the control force (F) relative to the flap angle (β).....	29
Figure 2.2 : The experimental wind tunnel setup.....	30
Figure 2.3 : CAD view of the 2D wing setup.....	31
Figure 2.4 : Mechanical system a) View from under the wind tunnel b) Diagram.....	32

Figure 2.5 : General mass spring system with resulting cubic stiffness schema	32
Figure 2.6 : Flap-NES design. a) CAD view b) Schema.....	33
Figure 2.7 : Diagram of the sensor distribution in 2D wing	35
Figure 2.8 : A sensor signal and fitted damped sinusoidal function comparison.....	36
Figure 2.9 : Response of the flap-TMD and flap-NES to a manually imposed initial displacement in zero wind speed.....	37
Figure 2.10 : Comparison of alpha rotation sensor signal above and below wind tunnel	38
Figure 2.11 : Frequency evolution of h and α with wind speed (2DOF)	40
Figure 2.12 : Frequency evolution of h , α and β with wind speed in flap-TMD configuration.....	40
Figure 2.13 : Frequency evolution of h , α and β with wind speed in NES-flap configuration	40
Figure 2.14 : Response of 2DOF system at wind speed of 15.35 m/s	41
Figure 2.15 : Response of 3DOF flap-TMD system at wind speed 16.09 m/s	42
Figure 2.16 : Response of 3DOF flap-NES system at wind speed 16.20 m/s.....	42
Figure 2.17 : Average LCO peak h amplitude	43
Figure 2.18 : Average LCO peak α amplitude	44
Figure 2.19 : Average LCO peak β amplitude	44
Figure 3.1 : Schema of the flap-NES concept in aircraft wing	50
Figure 3.2 : General mass spring system (left) with resulting nonlinear stiffness (right).....	51
Figure 3.3 : Flap-NES design a) CAD view b) schema	51
Figure 3.4 : Design of the 3D wing: a) CAD model b) Instrumentation.....	54
Figure 3.5 : System used to add masses to the leading edge and/or the trailing edge	55
Figure 3.6 : 3D Wing setup mounted on shaker a) without skin b) with skin.....	58
Figure 3.7 : a) Wind tunnel used for tests b) wing in wind tunnel.....	59

Figure 3.8 : Modal shapes of wing in mass configuration 1 with blocked flap-NES. a) lift bending, b) drag bending c) torsion	60
Figure 3.9 : Wing tip FRF in lift direction a) mass config. 1, b) mass config. 2, c) mass config. 3	62
Figure 3.10 : Mass config. 1: a) Evolution of the energy the wing, b) Ratio of flap-NES A to blocked flap-NES of the energy of the wing.....	64
Figure 3.11 : Mass config. 2a) Evolution of the energy of the wing, b) Ratio of flap-NES B to blocked flap-NES of the energy of the wing.....	65
Figure 4.1 : a) 2DOF and b) 3DOF typical aeroelastic sections. [41].....	71
Figure 4.2 : Schema for loosely coupled Fluid-Structure interaction [40].....	72
Figure 4.3 : Non-linear pitch stiffness: (a) cubic stiffness with freeplay; (b) freeplay. [100]	73
Figure 4.4 : UVLM airfoil discretization. (a) free wake (b) rigid wake (c) flat wake	75
Figure 4.5 : Plunge motion.....	78
Figure 4.6 : Pitch motion.....	79
Figure 4.7 : Dimensionless oscillation frequency against dimensionless wind speed for 2DOF linear case.....	81
Figure 4.8 : Damping against dimensionless wind speed for the 2DOF linear case.....	82
Figure 4.9 : Dimensionless oscillation frequency against dimensionless wind speed for 3DOF linear case.....	83
Figure 4.10 : Damping against dimensionless wind speed for the 3DOF linear case.....	84
Figure 4.11 : Change of phase trajectory of subcritical LCO for 2DOF airfoil.....	88
Figure 4.12 : RMS amplitudes as a function of speed over linear flutter speed.	90

LIST OF SYMBOLS AND ABBREVIATIONS

Symbols

$x_{\beta}b$	Centre of gravity to elastic axis distance of the control surface
f_a	Aerodynamic force vector
$x_{\alpha}b$	Centre of gravity to elastic axis distance of the airfoil
B_s	Damping matrix
U_{∞}	Incident flow speed
M_s	Inertial matrix
q	Position vector
f_s	Restoring force vector
K_s	Stiffness matrix
ab	Midchord to elastic axis of the airfoil
b	Semi chord length
c	Airfoil chord
cb	Midchord to elastic axis of the control surface
h	Heave displacement
K	Dimensionless reduced frequency
k	Spring constant
U_F	Flutter speed
α	Pitch deflection
β	Flap deflection
ζ	Damping ratio
ω	Oscillating frequency

M	Mach number
Re	Reynolds number
$\eta_{\alpha,k}$	Non-linear stiffness power
E	Total signal energy
φ	Phase angle

Abbreviations

ABS	Acrylonitrile Butadiene Styrene
ABS	Acrylonitrile Butadiene Styrene
AIC	Aerodynamic Influence Coefficients
ALE	Arbitrary Lagrangian Eulerian
CAD	Computer Aided Design
CFD	Computational Fluid Dynamics
CPU	Central Processing Unit
DLM	Doublet Lattice
DOF	Degree Of Freedom
DTS	Dual-Time Stepping
FFT	Fast-Fourier Transform
FRF	Frequency Response Function
FVT	Flight Vibration Tests
GVT	Ground Vibration Test
HSPM	Hess Smith Panel Method
LCO	Limit Cycle Oscillation

LUSGS	Lower-Upper Symmetric Gauss-Seidel
LUVLM	Linear Unsteady Vortex Lattice Method
NACA	National Advisory Committee for Aeronautics
NASA	National Aeronautics and Space Administration
NES	Non-linear Energy Sink
NLFD	Non-Linear Frequency Domain
NLTVA	Nonlinear Tuned Vibration Absorber
RANS	Reynolds Averaged Navier-Stokes
RHS	Right Hand Side
RMS	Root Mean Square
TMD	Tuned Mass Damper
URANS	Unsteady Reynolds Averaged Navier-Stokes
UVLM	Unsteady Vortex Lattice Method
VIV	Vortex Induced Vibration
VLM	Unsteady Vortex Lattice Method

LIST OF APPENDICES

Appendix A – Development of equations of motion	95
Appendix B – Theodorsen MODEL	102

CHAPTER 1 INTRODUCTION

In this chapter, the work is put into context, important definitions are made and a bibliographical review of pertinent previous studies is presented. The research objectives are presented and the methodology is introduced. Finally, an outline of the thesis structure is given.

1.1 Context

This section presents the global field of study in order to set the context of the work. The area of aeroelasticity defined with its several applications and effects which justify its importance. The focus is then on aeroelasticity within the aeronautics domain and a brief history and its current challenges are presented. Some of the main aeroelastic phenomena are then presented and defined.

1.1.1 Aeroelasticity

The work presented is encompassed within the field of dynamic aeroelasticity. Aeroelasticity is the area of physics which studies the interaction between a flexible body and a surrounding fluid field. Often represented with Collar's triangle (fig. 1.1), dynamic aeroelasticity brings together the effects of aerodynamics, elasticity and inertia. The contexts in which aeroelastic phenomena appear are varied and include, for example, bridges, offshore platforms, wind turbines and turbo machinery. The area of focus of this work in aeronautics and the system considered is a flexible aircraft wing in a wind flow.

Fluid structure interaction often leads to undesired phenomena which will be presented further on. In some cases these phenomena lead to unstable dynamics or to strong structural vibrations. This means that many attempts have been made regarding aeroelastic control and vibration mitigation to avoid undesirable events

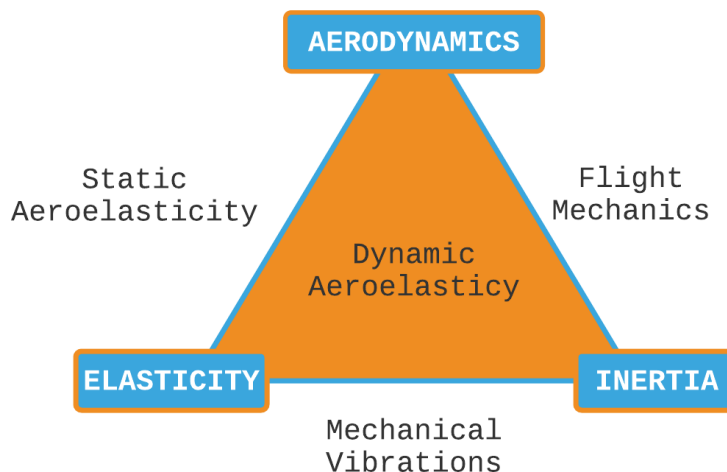


Figure 1.1 : Collar's Triangle [1]

Throughout the history of aeronautics, aeroelasticity has been an important factor regarding aircraft design. This is because aeroelastic phenomena can cause undesired behavior which may result in structural failure. For this reason, aeroelasticity is one of the main flight envelope limiting factors. Since the start of aviation, it was observed by pilots and engineers how aircraft, which are actually elastic structures, interacted with the airflow during flight causing undesired behavior, such as strong vibrations or control loss, and, in some unfortunate cases, leading to accidents. One of the first cases was the Langley's tandem monoplane which was destroyed during flight in 1903 due, most probably, to aeroelastic effects. Similarly, the DH-9 in 1917 and the Caproni CA. 48 in 1919 were also lost in flight [1]. During the Second World War, many military aircraft such as the Mitsubishi A6M "Zero" also experienced serious problems due to aeroelastic effects as their design wasn't yet considering the possible negative outcome of the fluid-structure coupling [2].

Although knowledge in this field has progressed substantially, the modern airplane still requires many efforts for negative aeroelastic phenomena to be avoided including ground vibration tests (GVT), flight vibration tests (FVT) and theoretical analysis. Furthermore, in the last years, progress in aerospace engineering has made aeroelasticity a heavily researched topic. In order to achieve more efficient aircraft, which consume less fuel, a new tendency to design higher aspect ratio wings [3] and to use lighter materials has emerged. On one hand, these factors result in an important gain of aerodynamic efficiency and a significant weight reduction of the

wings but, on the other hand, they increase fluid structure interactions since the wings become more flexible [4]. Another area of progress has been high-altitude long-endurance aircrafts, which have become more common. These aircrafts also tend to experience larger deflections in flight. Finally, the appearance and popularization of drones, as well as disruptive aircraft designs, constantly challenge the aerospace industry with completely new designs and applications and require parallel developments in the field of aeroelasticity (fig. 1.2).



Figure 1.2 : Examples of the recent aeroelastic challenges a) highly flexible rotor blades [5] b) Helios high-altitude flying wing by NASA [6] c) high Aspect Ratio wings in Boeing Sugar Volt

1.1.2 Dynamic aeroelastic phenomena

In this section the main aeroelastic phenomena of interest for this work are presented. General aeroelastic phenomena can be divided into static and dynamic. The main static effects to consider are divergence and control surface reversal. The divergence occurs when a wing presents a progressively high angle of attack until structural failure is reached due to the impossibility to sustain the increasing aerodynamic forces caused by the growing angle of attack. Control reversal takes place when the flexibility of the wing causes its control surface to generate an undesired force. These phenomena are not further discussed in this section since the present work focuses on dynamic aeroelasticity. The notions of classic flutter and vortex induced vibration are presented as they will appear in this research work.

1.1.2.1 Classic Flutter

Within fluid structure interactions in dynamic aeroelastic systems, classic flutter appears when the system is linear and, in a wing; it is typically caused by the coalescence of two modes:

flexion and torsion. Figure 1.3 presents a typical two degrees of freedom aeroelastic section, a bidimensional simplification of a wing where the flexion and torsion are represented by the heave (h) and pitch (α) respectively. Flutter speed separates the flight regimes as stable or unstable: below the flutter speed, vibrations are damped whereas above the flutter speed the wing's response becomes unstable and grows in amplitude until structural failure is reached. This phenomenon is due to the extraction of energy of the structure from the fluid. These oscillations are therefore considered to be auto-enhanced as they are not caused by an external source but from the fluid-structure interaction itself. Classic flutter can be identified at the speed at which at least one mode's structural damping becomes negative (fig.1.4).

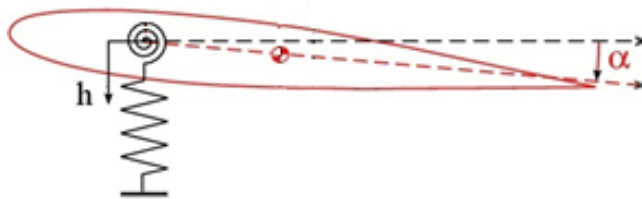


Figure 1.3 : 2DOF typical aeroelastic section

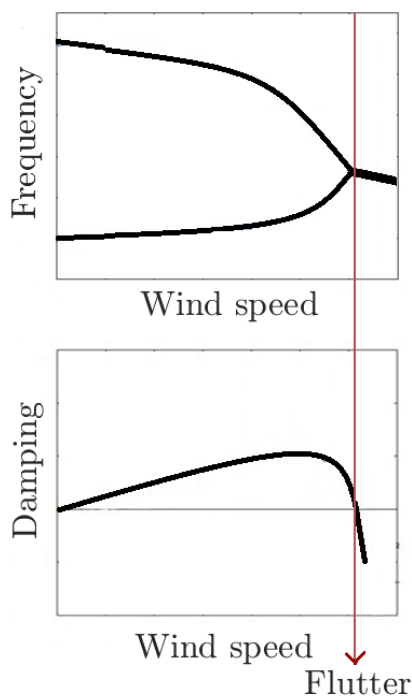


Figure 1.4 : Frequency and damping against wind speed for a system presenting classic flutter

1.1.2.2 Limit cycle oscillations

In the post flutter regime, as the vibration amplitude grows, if the structural limit is not reached before, the flow may become detached from the wing giving rise to nonlinear aerodynamic effects. This nonlinearity causes the response to become a constant or modulated amplitude oscillation called limit cycle oscillation (LCO). LCOs are a steady response of the system where the oscillation remains periodic unless the wind speed changes. Although LCO are steady, if they have high amplitude they can still cause structural failure by fatigue. This phenomenon not only occurs as previously described but can also be observed if there is another source of nonlinearity.

Nonlinearities can mainly have two different types of sources: aerodynamic or structural. Regarding aerodynamic nonlinearities their presence is commonly due to transonic flight regimes or to flow separation due to high angles of attack or to large amplitude oscillations, as previously mentioned. Structural nonlinearities can have distributed sources such as rivets in the fuselage or concentrated sources such as free play in a control surface [7]. It has been found that when nonlinearities govern the system's behavior, initial conditions may cause the system's response to change between two or more possible stable outcomes [8].

1.1.2.3 Nonlinear Flutter

As previously described, LCO can appear in the supercritical regime if nonlinearities are present in the system. The LCO will have constant average amplitude which will gradually increase with wind speed. This is known as “soft flutter” because the LCO amplitude grows slowly and since the wind speed is over the flutter speed they can be easily avoided. Another possibility, more difficult to predict and therefore more dangerous for the structure, is known as “hard flutter”. In “hard flutter” the nonlinear system encounters a stable LCO response in the subcritical regime, and as a result, encounters high amplitude oscillations at a wind speed at which the system would be expected to be damped for any given initial condition in the absence of nonlinearities. These two phenomena are presented in fig. 1.5 where the mean amplitude of the oscillation is presented against wind speed, U_F is the soft flutter speed and in b) U_A represents the beginning of hard flutter.

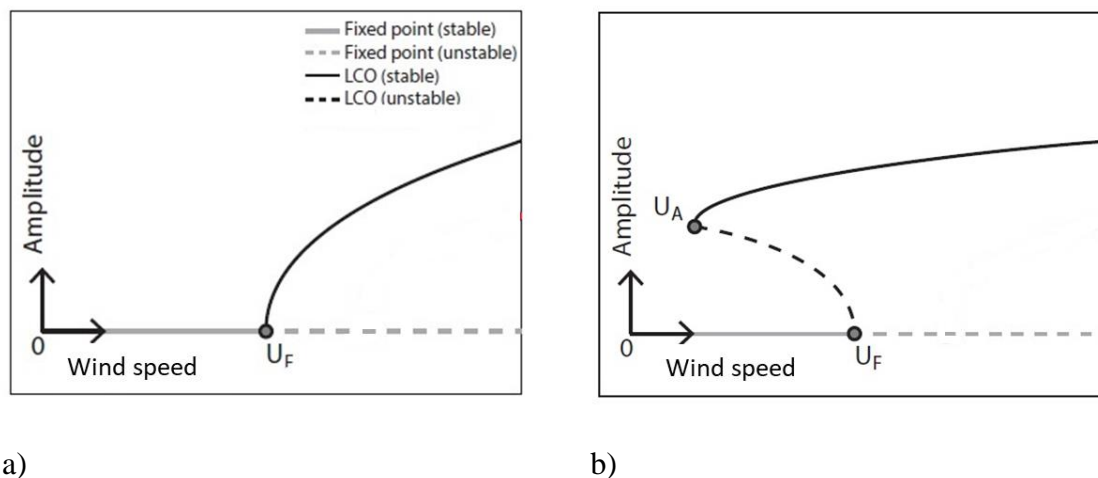


Figure 1.5 : Nonlinear aeroelastic systems a) supercritical bifurcation (soft flutter) b) subcritical bifurcation (hard flutter)

1.1.2.4 Vortex induced vibration

As mentioned earlier, limit cycle oscillations do not only occur as a result of high angles of attack due to flutter. Another phenomenon which may lead to LCOs is vortex induced vibration (VIV). VIV is an oscillation of the structure in response to the Von Karman (VK) vortex sheet shed due to the detached flow. In the case of the aircraft wing which is a streamlined body, this detachment of the flow is a consequence of high angles of attack. However, VIV is a common phenomenon in bluff bodies where the flow is always detached. Regarding the nature of the VIV there are two possible states: lock-in and lock-out. When the frequency of the VK vortices and the structure's natural frequency are very close, lock-in is observed and the VIV occur at the natural frequency. If this is not the case, the VIV are said to be in lock-out and occur at the VK vortices frequency [9].

1.2 Experimental Control and Vibration Mitigation Systems

As presented in the previous section, aeroelastic phenomena can cause undesired structural effects and can even lead to either immediate structural failure or failure by fatigue. Therefore, many different attempts have been made regarding aeroelastic control and vibration mitigation. One of the global objectives of aeroelastic control is to delay flutter to higher wind speeds enlarging the aircraft's flight envelope. Another control objective could be avoiding "hard flutter"

in the system (fig. 1.6). Regarding vibration mitigation, achieving lower amplitude LCOs in a system would avoid problems associated with fatigue. This section focuses on the progress of control and vibration mitigation within the context of aeroelasticity. The solutions are divided into passive and active approaches.

In active control, a sensor measures the motion, forces, accelerations, etc. of the moving part and a powered actuator which generates a force to resist the unwanted motion. Passive vibration control does not require power input; it relies on the damping properties of materials and components used in its design. This makes passive control suitable in emergency cases (i.e. power shortage).

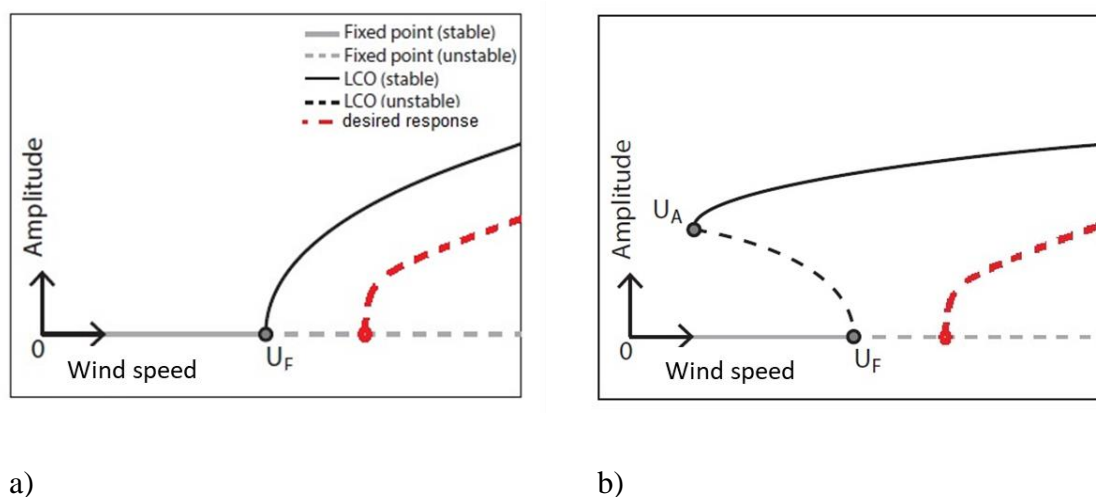


Figure 1.6 : Nonlinear aeroelastic system control a) supercritical bifurcation (soft flutter) b) subcritical bifurcation (hard flutter)

1.2.1 Active aeroelastic control

In order to increase the system's flutter speed, the most common solutions are active approaches. One of the simplest ways of applying control forces is to use the aircraft's control surfaces, which means fewer modifications of the structure [10]. [11] and [12] achieved an increase in flutter speed of 50% and 13.4%, respectively, numerically and experimentally using actioned control surfaces. Another approach, which has been explored, is the use of piezoelectric actuators. [13] were able to increase flutter speed of between 6 and 11% in this way. [14] performed wind tunnel tests on a 1/6 scale model of a F-18 with tail buffeting vibrations of the

structure due to unsteady aerodynamic loads and were able to decrease around 60% the root mean square (RMS) amplitude of the vibrations using piezoelectric and control surfaces actuators. Although active methods are very efficient, they have the important drawback of being obsolete in emergency cases (i.e. lack of power).

1.2.2 Passive Aeroelastic Control

Regarding passive control, which solves the energy dependency problem, there are several solutions. For instance, damping can be achieved via the choice of materials of the structure. By attempting to separate the flexion and torsion modes of a wing, [15] showed the effect of viscoelastic materials in a sandwich configuration to mitigate panel flutter. This is known as aeroviscoelascity. Viscoelastic materials have shown to be very efficient in vibration mitigation and an important advantage is that they are reasonably easy to install in existing structures. However, the disadvantage is that their performance is highly affected by many factors, mainly temperature and vibration frequencies. [16] carried out experiments on an aeroelastic set up using springs made out of shape memory alloys in order to introduce hysteretic mitigation which increased flutter speed and decreased LCO amplitude. The rate of energy mitigated was very high compared to other solutions; however, it was highly dependent on the vibration frequency.

Another possibility regarding passive approaches is the use of dynamic absorbers. Figure 1.7 shows a schematic representation of a one degree of freedom system (main system), with a dynamic absorber which is a mass attached to it with linear or nonlinear springs and dampers. Depending whether the absorber's stiffness is linear or nonlinear, its properties and scope vary.

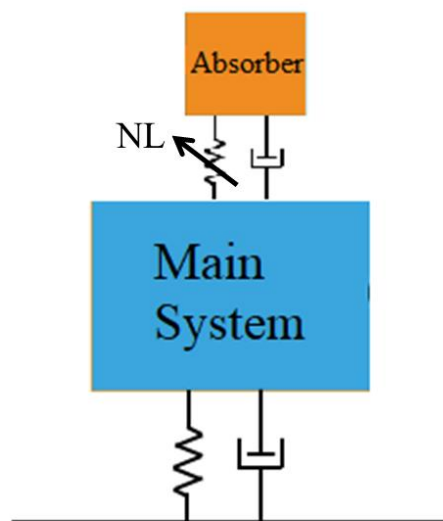


Figure 1.7 : Schematic representation of a system with a secondary absorber

The simplest absorbers are tuned mass dampers (TMD) which are a good option for vibration control in certain cases, for instance they are widely used in civil engineering [17]. This absorber can split the main system's large amplitude resonance peak into two smaller amplitude peaks; as long as it is correctly tuned. Methods have been developed in order to tune the absorber in accordance to the main system's natural frequency [18] [19]. The classic linear TMD is simple and efficient but it has the important limitation of only being useful close to a single frequency due to its linear characteristics. In the case of an aeroelastic wing, the system's natural frequencies change with the wind speed and also with the fuel mass embedded in the wing, therefore TMDs are not the ideal solution. Also, for TMDs to be efficient, a non-negligible mass (around 10% of the modal mass of the mode to be controlled) must be added which is not ideal in the aerospace industry where weight minimization is always a priority.

A solution which is more appropriate for wings is the Nonlinear Tuned Vibration Absorber (NLTVA) [20]. Due to its nonlinear stiffness, the NLTVA becomes efficient not only for a single frequency, but for broadband frequency control [21]. The Nonlinear Energy Sink (NES) [22] is a particular type of NLTVA with a purely nonlinear stiffness (fig. 1.8) and linear damping that presents high vibration absorption skills for a broadband frequency range and a low added mass (around 1% of the modal mass of the mode to be controlled). It is able to absorb energy from the main system and mitigate it via targeted energy transfers, also known as energy

pumping, as long as the minimum activation energy is reached [23]. This means that it is efficient for a larger frequency band than other dynamic absorbers. (fig. 1.9).

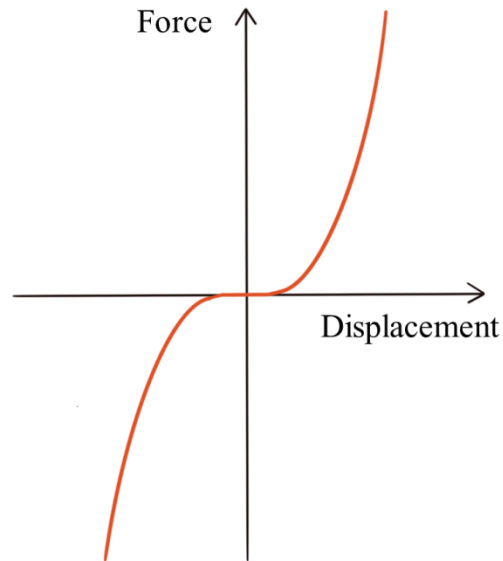


Figure 1.8 : Hardening cubic stiffness force

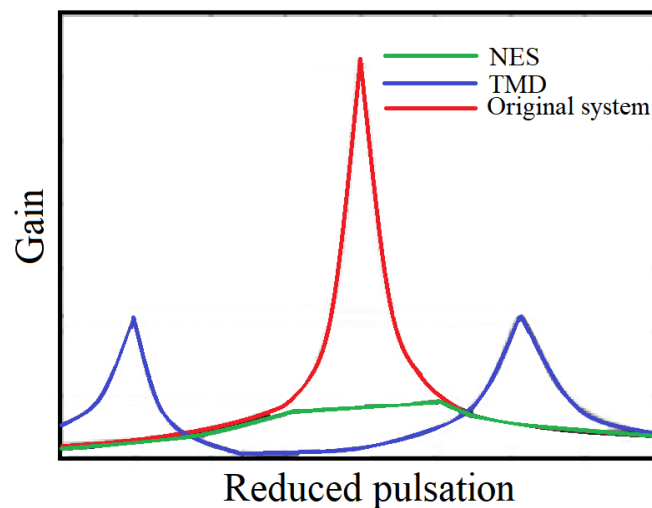


Figure 1.9 : Amplitude pulsation diagram of a linear oscillator of 1 DOF [24]

The simplest way to create the cubic stiffness required in a NES design is to place the traction springs joining the secondary absorber to the main system in parallel (see fig. 1.10) instead of using a torsion spring or traction springs in parallel which would give rise to a linear stiffness.

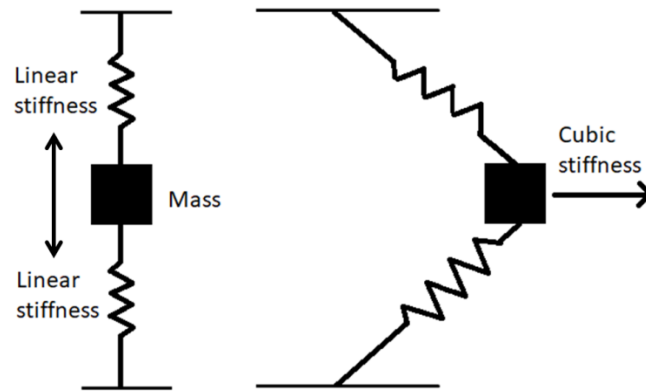


Figure 1.10 : General mass spring system with resulting cubic stiffness schema

The NES is already used in civil engineering and its only drawback is that it can be difficult to design. Some of the current applications of the NES are: shock isolation [25], seismic vibration control [26], energy harvesting [27], suppression of the stick-slip phenomenon in machining [28]. Regarding aeroelastic control it has been used to control VIV by [29]. Within flutter suppression in aeroelastic profiles, the use of NES has been studied in [30], [31] and [32] and in tridimensional wings in [33] and [34]. The NES is concluded to be appropriate for flutter control in these publications.

1.3 Numerical Methods for Aeroelasticity

Concerning the numerical simulation of passive control using a nonlinear absorber, the main challenge remains the modeling of the aerodynamic efforts. The objective of this subsection is to present the evolution and the state of the art of some of the main aerodynamic methods which have been developed. A summary of these methods, together with the advantages, disadvantages and references, can be found in table 1.1, presented in ascending calculation fidelity. A general overview of the methods used in the aerospace industry and the main challenges can be found in [35].

The idea of aeroelastic numerical simulations is that the equations of motion consider the effects of the aerodynamic forces on the structure and vice versa. The structural and the aerodynamic models can vary but the global equations of motion remain the same throughout the different approaches. Due to the hypothesis made by the aerodynamic model, the way in which the structure is modeled is affected. For example, in the case of the aeroelastic profile of interest,

it is modeled as a flat plate for lower fidelity methods and as a 2D profile with thickness for higher fidelity methods. In the same way, the wake will be modeled differently from one aerodynamic model to the other.

The aeroelastic coupling between the structure and the fluid may be either strongly coupled, where the structural and aerodynamic equations are solved simultaneously, or loosely coupled where the two systems are solved iteratively. In the loosely coupled scheme for each time step first, the aerodynamic forces are computed and interpolated onto the structure whose new position velocity and acceleration are calculated [36]. The interpolation of the aerodynamic forces on the structure and of the displacement, velocity and structure on the fluid can be computed in different ways [37, 38]. In order to achieve higher accuracy in loosely coupled schemes, the equations of the structure and the fluid can be iterated until convergence is achieved in each time step [39]. In general, loosely coupled models are easier to implement since they can be created from previously existing fluid and structure solvers and they present lower computational time and cost. An important feature is that the aero-structural interpolations must be conservative, i.e. virtual work in the structure and aerodynamic models must be the same [40].

1.3.1 Equations of motion

In order to present the equations of motion, a 2D profile is first presented, the particularities and simplifications of this profile and its resulting wake will then be subsequently given as the aerodynamic models are presented.

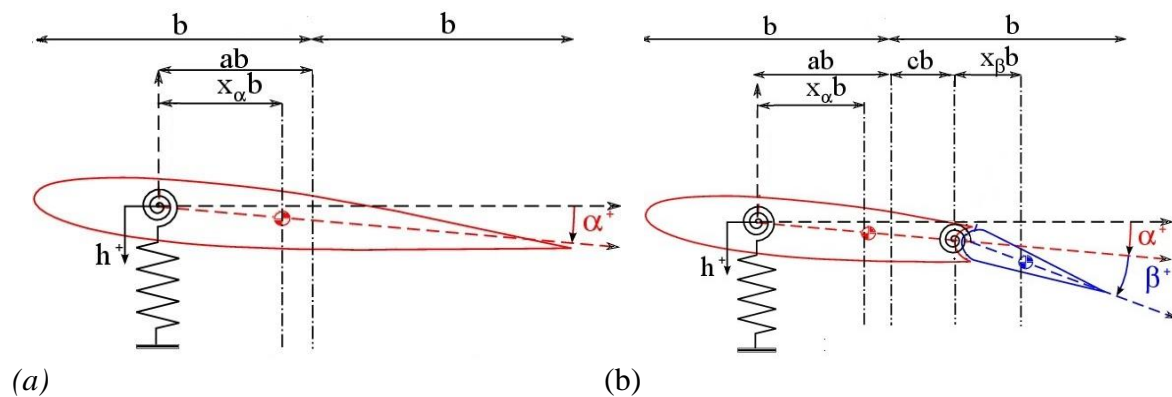


Figure 1.11 : Typical aeroelastic sections a) 2DOF b) 3DOF [41]

Figure 1.11 represents the 2DOF and 3DOF typical aeroelastic sections where h , α and β represent the plunge, pitch and deflection of the control surface. The other parameters represented are b , the semichord, ab which is the distance between the elastic axis, the midchord and $x_\alpha b$ is the distance between the elastic chord and the center of gravity, $x_\beta b$ is the distance between the elastic chord of the aileron and its center of gravity and cb is the distance between the midchord and the elastic axis of the aileron. The general equation of motion is:

$$M_s \ddot{q} + B_s \dot{q} + K_s q = F_a \quad (1.1)$$

M_s , B_s and K_s are the mass, damping and stiffness matrix respectively, q is the position vector containing all the degrees of freedom and F_a is the aerodynamic force vector. For the 3DOF aeroelastic airfoil case, the matrices and vectors are given by:

$$M_s = \begin{bmatrix} M & S_\alpha & S_\beta \\ S_\alpha & I_\alpha & I_\beta b(c-a)S_\beta \\ S_\beta & I_\beta b(c-a)S_\beta & I_\beta \end{bmatrix} \quad (1.2)$$

$$B_s = \frac{1}{\omega} \begin{bmatrix} g_h M \omega_h^2 & 0 & 0 \\ 0 & g_\alpha I_\alpha \omega_\alpha^2 & 0 \\ 0 & 0 & g_\beta I_\beta \omega_\beta^2 \end{bmatrix} \quad (1.3)$$

$$K_s = \begin{bmatrix} M \omega_h^2 & 0 & 0 \\ 0 & I_\alpha \omega_\alpha^2 & 0 \\ 0 & 0 & I_\beta \omega_\beta^2 \end{bmatrix} \quad (1.4)$$

$$F_a = \begin{pmatrix} L \\ M_\alpha \\ M_\beta \end{pmatrix} \quad (1.5)$$

$$q = \begin{pmatrix} h \\ \alpha \\ \beta \end{pmatrix} \quad (1.6)$$

Where M is the mass of the profile, S_α is the static moment of the entire airfoil around the elastic axis, S_β is the static moment of the aileron around its elastic axis. I_α is the moment of inertia of

the entire airfoil around the elastic axis and I_β is the moment of inertia of the aileron around its elastic axis. The full development of these equations of motion can be found in [2] and in annex A.

1.3.2 Theodorsen model

Theodorsen model is often taken as a reference method due to its simplicity. It is an analytical method, initially developed in 1935 [42] and further developed in [43], which originally solves the aeroelastic equations of a simplified profile, represented by a flat plate section of semichord b , (fig. 1.12) presenting pitch (α) and plunge (h) movement in an incompressible and inviscid flow of speed U . The original formulation is in the frequency domain. The equations are valid for thin profile, small displacement and linear wake. Although many simplifications and hypotheses are made, Theodorsen model is able to predict flutter speed accurately in many cases with a very low computation time and cost and even the limit cycle response of nonlinear systems [44] [45]. In the presence of nonlinearities, the equations are more easily solved in the time domain so the original method is transformed by the Jones approximation [46]. In this transformation, the original Theodorsen function $C(k)$ which is a complex transform function of the reduced frequency $k = \frac{\omega b}{U}$ is replaced the Wagner function, its inverse Fourier transform [47].

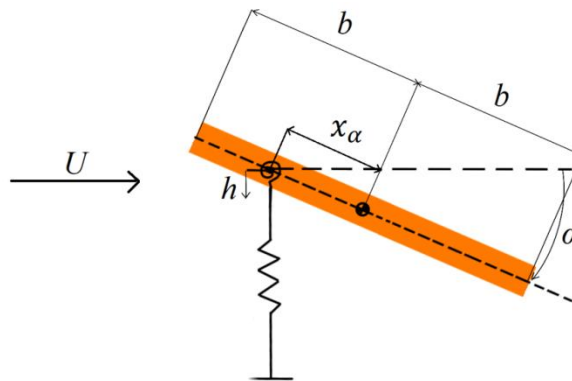


Figure 1.12 : Flat plate section used in original Theodorsen model

The aerodynamic forces in Theodorsen model and $C(k)$, the so-called Theodorsen function, whose exact expression can be found in [48] and in annex B.

1.3.3 Boundary element methods

Potential solvers also have reasonably low computational times and costs. They consist of numerical schemes which present the solutions to Laplace equation (mass conservation for irrotational flows): either source, doublet or vortex singularities [49]. They can be used to solve linear inviscid and irrotational flows and are largely used in the aeronautics industry. Some of the methods in this category include the Hess Smith Panel Method (HSPM) [50], the Doublet Lattice Method (DLM) [51] [52] and the unsteady vortex lattice method (UVLM) [53, 54]. Regarding bidimensional aeroelastic simulations, the three methods are only appropriate for thin profiles. However the UVLM is the only method appropriate for nonlinear structures. This is why it will be retained for the present research work where structural nonlinearities are important.

In UVLM, the airfoil and the aileron are discretized into panels (respectively red and blue in fig. 1.13) and the transport of vortices (black) is accounted for by a shedding wake in the case of the free wake approach. For each panel, there is a vortex and a collocation point (fig. 1.13). The vortex points induce a velocity on the rest of the panels and in the collocation point the resulting velocity is calculated.

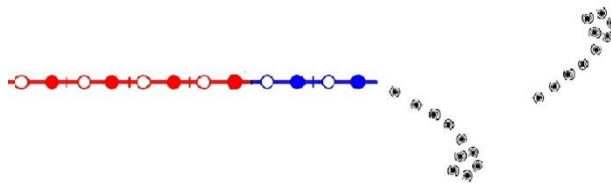


Figure 1.13 : UVLM airfoil discretization with free wake

○:airfoil vortex point, ●:airfoil collocation point, ○:aileron vortex point, ●: aileron collocation point, ⊙:wake vortex

By imposing the same vorticity on the shed wake and on the trailing edge panel, the Kutta circulation condition is satisfied. The Neumann boundary conditions for the velocity potential is applied on the airfoil and close the system of equations [54]. UVLM is solved in the time domain, although recently a frequency-domain formulation has been developed [55]. The computational implementation of the UVLM code is fully described in [54]. By solving a linear system of equations (equation 1.9), the vorticity (γ) at each point is obtained.

$$\text{AIC} * \gamma = \text{RHS} \quad (1.9)$$

where AIC is the Aerodynamic Influence Coefficients matrix which contains the induced velocities ($v_{j,i}$), which are calculated as shown in equation 1.10, and RHS is the right-hand side vector containing the inflow velocity, the airfoil velocity and the position of the airfoil.

$$v_{j,i} = \frac{\gamma_j}{2\pi r_{ij}^2} \{y_i - y_j\} \quad (1.10)$$

Once the vorticities (γ) are obtained, the pressure coefficient is calculated using the unsteady Bernoulli equation:

$$C_{p,i} = \frac{\gamma_{i,k}}{\Delta l} * (u_\infty - v_{m,i} + \sum_{l=1}^k v_{l,i}) * n_i + \frac{1}{\Delta t} \sum_{m=1}^i \gamma_{i,k} - \gamma_{i,k-1} \quad (1.11)$$

which enables the calculation of the rest of the aerodynamic coefficients.

1.3.4 Volumetric methods

Higher-fidelity methods are capable of modeling the physics more accurately by making significantly fewer hypotheses concerning the nature of the structure and the flow around it. This nevertheless results in much higher computational time and cost. Contrary to the previously presented methods where only the airfoil and the wake are modeled, volumetric methods require a large portion of the fluid volume to be meshed so that the aerodynamic forces can be assessed by solving a set of conservation laws (mass, momentum, energy) at discrete space/time intervals. This is an advantage when modeling complex structures and in the case of bidimensional wing aeroelasticity it enables to consider airfoil thickness with or without structural nonlinearities. The compressibility of the flow can also be considered. The Navier-Stokes equations of continuity, momentum and energy are as follows [56].

Continuity:

$$\frac{\partial \rho}{\partial t} + \nabla \cdot \rho V = 0 \quad (1.9)$$

Momentum:

$$\rho \frac{Du}{Dt} = -\frac{\partial p}{\partial x} + \frac{\partial \tau_{xx}}{\partial x} + \frac{\partial \tau_{yx}}{\partial y} + \frac{\partial \tau_{zx}}{\partial z} \quad (1.10a)$$

$$\rho \frac{Dv}{Dt} = -\frac{\partial p}{\partial y} + \frac{\partial \tau_{xy}}{\partial x} + \frac{\partial \tau_{yy}}{\partial y} + \frac{\partial \tau_{zy}}{\partial z} \quad (1.10b)$$

$$\rho \frac{Dw}{Dt} = -\frac{\partial p}{\partial z} + \frac{\partial \tau_{xz}}{\partial x} + \frac{\partial \tau_{yx}}{\partial y} + \frac{\partial \tau_{zz}}{\partial z} \quad (1.10c)$$

Energy:

$$\begin{aligned} \rho \frac{D(e + \frac{V^2}{2})}{Dt} = & \rho \dot{q} + \frac{\partial}{\partial x} \left(k \frac{\partial T}{\partial x} \right) + \frac{\partial}{\partial y} \left(k \frac{\partial T}{\partial y} \right) + \frac{\partial}{\partial z} \left(k \frac{\partial T}{\partial z} \right) - \nabla \cdot pV + \frac{\partial u\tau_{xx}}{\partial x} + \frac{\partial u\tau_{yx}}{\partial y} \\ & + \frac{\partial u\tau_{zx}}{\partial z} + \frac{\partial v\tau_{xy}}{\partial x} + \frac{\partial v\tau_{yy}}{\partial y} + \frac{\partial v\tau_{zy}}{\partial z} + \frac{\partial w\tau_{xz}}{\partial x} + \frac{\partial w\tau_{yz}}{\partial y} + \frac{\partial w\tau_{zz}}{\partial z} \end{aligned} \quad (1.11)$$

where u, v, w are the three components of the velocity vector V , ρ, T and p are the density of the fluid, its temperature and the pressure respectively and τ is the shear force on the fluid element. k is the thermal conductivity of the fluid, \dot{q} is the heat generation per unit volume and e is the internal energy.

Euler [57] and Reynolds-Averaged Navier Stokes (RANS) [58] are two commonly used methods in this category. The main difference between the two models is that RANS is the only of the two models which takes into account the effects of the flow viscosity by modeling turbulence, typically modeled via the eddy viscosity assumption [59]. The unsteady version of RANS, URANS, is appropriate for unsteady flows and can be solved both in the time domain by using for example the dual time stepping approach (DTS) [60] or in the frequency domain, for example in the nonlinear frequency domain (NLFD) [61]. URANS is usually considered the highest-fidelity method used in the aerospace industry since other models are too expensive and slow. Since Euler and URANS will be two of the methods used in this work, further detail concerning the URANS development can be found in section 4.3.2.

Higher-fidelity volumetric computational fluid mechanics (CFD) methods include large eddy simulation (LES) [62, 63] and direct numerical simulations (DNS) [64] which solves all the

turbulent scales. DNS is, for the moment, the most physically accurate model available. These high-fidelity methods are too expensive in terms of computational time and cost for this project where additionally, that level of accuracy in the flow computation is far from necessary.

Table 1.1 : Assumptions in the CFD models

		Airfoil		Fluid						
		Nonlinearities	Thickness	Compressibility	Vorticity	Viscosity	Unsteady fluctuations	All turbulent scales		
Analytical	Theodorsen model	✓								
Panel (potential)	HSPM									
	DLM									
	UVLM	✓			✓					
Volumetric	Euler	✓	✓	✓	✓					
	URANS	✓	✓	✓	✓	✓				
	LES	✓	✓	✓	✓	✓			✓	
	DNS	✓	✓	✓	✓	✓			✓	✓

1.4 Research objectives

The purpose of this work is to achieve passive aeroelastic control by integrating a NES, which has a cubic stiffness, as a flap on the tip outboard of an aircraft wing (fig. 1.14). This innovative solution is called flap-NES. The hypothesis is that it will act as a secondary oscillator and control the aeroelastic behavior of the wing. This aeroelastic behavior may have the form of instabilities or of steady vibration. During flight, the wing mass varies due to fuel consumption and structural frequencies may be wind speed dependent. The nonlinear features of the NES make it efficient over a broader frequency range so it will be adapted for mitigating vibration throughout the different flight regimes. Another hypothesis is therefore that the NES will have higher control capacities than a linear damper in this context.

As previously mentioned, NES and other secondary dampers have been used in flutter control; it was, however, inserted as an added mass in the wing. The advantages of its integration as a flap are that the structure is barely modified and also that there is negligible added mass in the system. Furthermore, the placement of the NES in the flow means that it will profit from aerodynamic damping. A high level of damping is required to control unstable responses. In this sense, this work presents a novel approach to aeroelastic wing control.

The main objective of this research work is therefore to give a proof of concept of this innovative design by evaluating its capacity to control aeroelastic instabilities and to mitigate the wing vibration. Another objective is to develop the necessary methods for optimization and analysis of the solution.

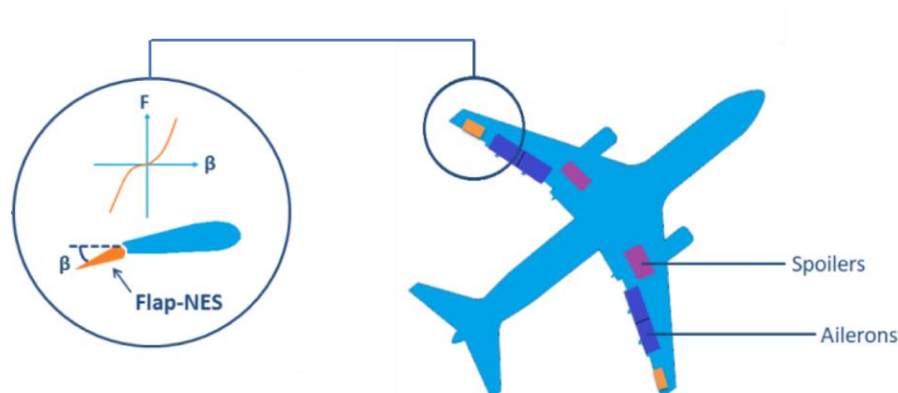


Figure 1.14 : Aircraft wing with NES schema

1.5 Methodology

In order to attain the work's global objective of carrying out passive flutter control using a NES, an experimental approach is chosen to ensure that no aeroelastic mechanism is neglected. This approach is used as a proof of concept of flap-NES control on a wing. The need of further flap-NES optimization is highlighted and, therefore the need for complementary analysis. Numerical methods are therefore developed and used to analyze similar aeroelastic phenomena. This section presents a brief overview the approaches used which is summarized in fig. 1.15.

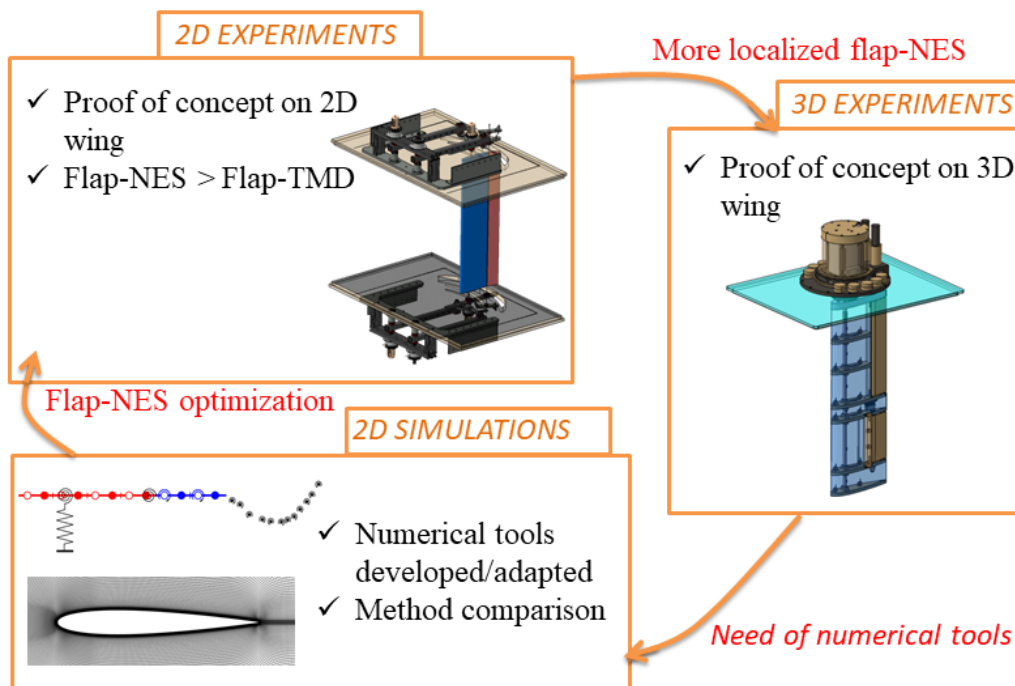


Figure 1.15 : Schematic overview of advances carried out throughout the PhD research work

Regarding the experimental analysis, the research is carried out in two steps, first on a bidimensional wing setup, and second on a tridimensional wing setup both illustrated in fig 1.16. Both setups contain a flap which can be blocked or equipped as a flap-NES so that its control effect on the wing can be compared to the original dynamic response. The bidimensional wing (fig. 1.16a) is rigid with a flap that spans the entire wingspan. The movement of the wing is enabled by a mechanical system placed above and below the wind tunnel so that it has no influence on the airflow. The tridimensional (fig. 1.16b) wing is flexible and is clamped at one end and free at the other.

Starting with a bidimensional wing enables the simplification of the system to a 2 (blocked flap) or 3 (free flap) degrees of freedom profile and therefore is a starting point. However, once the proof of concept is attained on the bidimensional wing, the choice of developing a tridimensional set-up is justified by the objective of working with a more realistic wing and a flap-NES closer to the real solution. Since the flap-NES spans the entire wingspan in the bidimensional wing, it is not possible to compare directly its control effect to that in a real wing where the flap-NES would occupy only a small portion of the wing. Therefore the proof of concept is extended in the tridimensional wing where the flap-NES is placed only at the wing tip.

The first step of the experimental approach is to design and build the experimental set-ups. Second, the set-ups are characterized and tested in a wind tunnel. The aeroelastic phenomena of the original systems are identified and the control capacity of the flap-NES is evaluated.

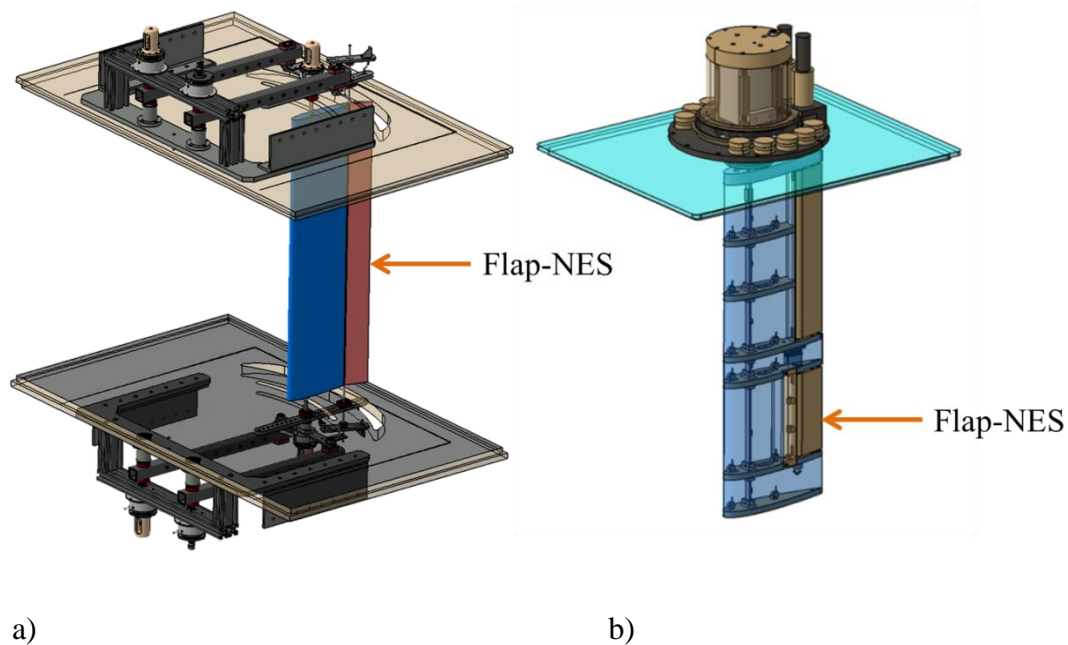


Figure 1.16 : CADs of experimental setups a) bidimensional wing b) tridimensional wing

The experimental approach serves as a necessary proof of concept of the solution but also highlights the need for complementary analysis for its development and optimization. In order to attain this objective, four aerodynamic methods are selected to be developed or adapted to a bidimensional wing. The four numerical methods are: Theodorsen model, UVLM (unsteady vortex lattice methods), Euler and URANS (unsteady Reynolds Averaged Navier-Stokes).

Developing bidimensional a numerical approach enables a simplification of the complex nonlinear aeroelastic system. The ability and accuracy of the methods in capturing the phenomena of interest are used. To do so, cases from the literature are selected. This enables to select the best methods in terms of compromise between time cost and accuracy by identifying the limitations of each method. These numerical studies constitute a first step in applying numerical models towards the flap-NES design.

1.6 Outline

The present work has been structured as a thesis by articles containing three journal articles (one published, the other submitted) with an introduction in which the connection between each of the articles is made and a final section with a global discussion and conclusion. This first chapter presents an introduction of the work with some definitions regarding aeroelasticity and its main phenomena and the importance of aeroelasticity in the history of aircraft design and in our days. A summary of the progress in both vibration mitigation and instability control, as well as state-of-the-art experimental and numerical approaches for tackling aeroelasticity are presented.

Chapters 2 and 3 contain the experimental approach of this study. Chapter 2 contains the first journal article, concerning an experimental study of the bidimensional aeroelastic wing. Its aeroelastic behavior is identified as classic flutter and the effects of the passive solution on the vibration response are identified on the flutter speed and on the LCO amplitude in the supercritical regime. Chapter 3 contains the second journal article which concerns the experimental study of a tridimensional flexible wing which undergoes vortex induced vibration. Its response is modified and analyzed by integrating the flap-NES.

Chapter 4 presents the numerical part of this study. It consists of the third and final journal article which is a comparison of different numerical methods for aeroelastic control. These methods are developed to respond to the need of a numerical approach for the further optimization of the control solution which arises from chapter 3. The methods range from the simplest analytical Theodorsen model, to a middle fidelity potential model (UVLM) and higher fidelity methods such as Euler and URANS. This article enables, through literature cases, to compare the performance, both in time and in accuracy, of these methods and to identify their limits. Some nonlinear features are introduced in order to anticipate the nonlinear behavior of the

flap-NES since these test constitutes a first step in applying numerical models towards the flap-NES design.

Finally, chapter 5 presents a global discussion concerning the three articles presented with a review of the scientific progress achieved. The conclusions which can be extracted from the work are given and the possible future of the study is outlined.

CHAPTER 2 ARTICLE 1: NONLINEAR FLAP FOR PASSIVE FLUTTER CONTROL OF BIDIMENSIONAL WING

FERNANDEZ-ESCUADERO, C., PROTHIN, S., LAURENDEAU, E., ROSS, A., MICHON, G. Submitted to *Journal of Aerospace Science and Technology*, 2021

This section contains an experimental journal article on the aeroelastic analysis of a bidimensional wing equipped with a flap-TMD and a flap-NES. The first step of this PhD work is to carry out an initial proof of concept of the innovative control solution presented. This initial analysis enables, to validate the hypothesis that installing a NES as a flap on an aeroelastic wing can mitigate energy from the wing structure and also to identify the strengths and weaknesses of the solution. Furthermore, the flap can alternatively be equipped as a linear mass damper, a TMD. The objective of this is to validate the hypothesis that the NES has higher control capacities than the TMD in this context.

In order to carry out the first proof of concept the simplest possible system was chosen, which is why this first analysis is carried out on a bidimensional wing. This bidimensional wing is a classic aeroelastic system which has been largely studied in the literature.

During wind tunnel tests, the original wing undergoes classic flutter. The flap-TMD and the flap-NES are observed to significantly increase the flutter. Furthermore, when the supercritical regime is analyzed, it is found that the flap-TMD reduces the wing energy during the supercritical limit cycle oscillations and that the flap-NES does so further. This paper therefore validates both the hypotheses of the adequacy of the control solution and the advantageous performance of the NES over the TMD. Both these hypotheses being valid on a bidimensional wing, the next step is to consider a system closer to an aircraft wing. This system is the tridimensional wing presented in chapter 3.

FERNANDEZ-ESCUADERO, C., PROTHIN, S., LAURENDEAU, E., ROSS, A., MICHON, G., “Nonlinear flap for passive flutter control of bidimensional wing” Submitted to *Journal of Aerospace Science and Technology*, 2021

Abstract. A solution for passive aeroelastic control is presented and tested experimentally on a bidimensional wing setup. The solution consists of a flap integrated in the wing which acts as a secondary mass damper and absorbs energy when aeroelastic instability is encountered. This device is passive, which makes it safe in emergency cases and adds little mass to the system in the fundamental case presented in this paper. If installed on actual aircraft wings, the flap-NES would use existing flaps as a control system, not substituting but coexisting with existing active control methods, thereby adding virtually zero mass to the existing system. Using a flap placed in the airflow enables the control system to benefit from aerodynamic damping with a behavior dependent on wind speed. The device can either have a linear or nonlinear stiffness. It is shown that both options absorb energy from the main system, that is the wing. The flap acts as a TMD (Tuned Mass Damper) in the linear case and as a NES (Nonlinear Energy Sink) in the nonlinear case. The nonlinear solution not only absorbs more energy at given wind speed, but it also is a more suited solution as the damper follows the wind speed dependent frequencies due to its nonlinear feature. In this work the flap-TMD and the flap-NES are tested experimentally on a bidimensional wing which presents classic flutter.

2.1 Introduction

Aeroelastic instabilities, such as flutter, are phenomena that limit flight speed of aircraft and can cause structural damage. Therefore, they have been widely researched both experimentally and numerically ([1];[65];[66];[67]). Furthermore, many attempts have been made regarding different control techniques as presented in this section.

In order to increase aircraft flutter speed, and therefore enlarge the flight envelope, active methods (energy inputted) are most common. A simple way of applying control forces is to use the aircraft's control surfaces, which require less modifications of the structure [68]. [69] and [70] achieved an increase in flutter speed of 50% and 13.4%, respectively, numerically and

experimentally using this kind of method. Another approach that has been explored to apply the necessary control forces is the use of piezoelectric actuators, which can be used both in an active and in a passive way [71]. [13] were able to increase flutter speed by 6 to 11%. Moses [72] performed wind tunnel tests on a 1/6 scale model of a F-18 with tail buffeting and was able to decrease by about 60% the root mean square (RMS) amplitude of the vibrations using piezoelectric and control surfaces actuators. Although active methods are very effective, they have the important drawback of not being of any use in emergency cases (i.e. power shortage).

Regarding passive control, there are several solutions that do not rely on external energy. For instance, vibration control can be achieved via the choice of materials of the structure. Viscoelastic materials have shown to be very effective in vibration mitigation and an important advantage is that they could be reasonably easy to install in existing structures [73]. However, the disadvantage is that their performance is highly affected by many factors, mainly temperature and vibration frequencies. [74] carried out experiments on a two degrees of freedom (2DOF) aeroelastic apparatus using springs made of shape memory alloys in order to introduce hysteretic mitigation which showed to increase flutter speed and decrease limit cycle oscillation (LCO) amplitude. The energy mitigation rate was very high compared to other solutions; however, the effectiveness of this solution remains dependent on vibration frequency.

Another possibility for passive control is dynamic absorbers. This solution has been used both for vibration mitigation and for instability control. Depending on the characteristics of the stiffness and damping force added by the absorber, the properties and therefore their applications vary. The simplest absorbers are Tuned Mass Dampers (TMDs) which are a good option for vibration control in certain cases [75] and are widely used in civil engineering. [76] achieved structural vibration mitigation by using hysteretic TMDs. The classic linear TMD is simple and effective but it has the limitation of only being useful within a narrow frequency band due to being linear. In the case of an aeroelastic wing, the system's natural frequencies change with the wind speed, therefore TMDs are not an ideal solution. Also, for TMDs to be effective, significant mass must be added (10% the modal mass of the mode to be controlled) [77].

A solution which is more appropriate for systems with changing frequencies is the Nonlinear Tuned Vibration Absorber (NLTVA) [78]. Due to its nonlinear behavior, the NLTVA is effective for broad frequency band. However it also has the disadvantage of adding mass which

is always a drawback in aeronautics. The Nonlinear Energy Sink (NES) [79] is a particular type of NLTVA with a purely nonlinear stiffness and linear damping that presents high vibration absorption for a broadband frequency range and a very low added mass. For example, [80] have developed a vibro-impact NES which adds only 1% of the system's mass. The main characteristic of the NES is its cubic stiffness. It is able to absorb energy from the main system and mitigate it via targeted energy transfers, also known as energy pumping [81]. The natural frequency of the NES is not unique but function of the vibration amplitude, so it is effective for broad frequency band.

NES's are already used in civil engineering and their main drawback is that their effectiveness is greatly dependent on proper parameter design. Current NES applications include both vibration mitigation and instability control, for example: shock isolation [82], seismic vibration control [83], energy harvesting [84], suppression of the stick-slip phenomenon in machining [85] and other fluid structure interactions, such as vortex induced vibration (VIV), where a body is periodically excited by the vortex induced in the flow [86] and [87]. Very recently, a vibro-impact NES has been used in galloping mitigation by [88].

The proposed control system consists of a flap which can be configured as a flap-TMD or as a flap-NES depending on the linear or nonlinear nature of its stiffness, respectively [41]. This device adds little mass to the system and is passive which makes it appropriate for emergency cases. Contrary to the previously described passive control systems, which rely on the addition of mass dampers inside the wing, the novelty of the solution lies in its inflow location. Since the flap is placed in the wind flow, it benefits from aerodynamic damping and wind speed dependent properties. This means that the control solution itself is submitted to fluid structure interactions in a way which can enhance its control efficiency.

The effectiveness of flutter control using the proposed solution in a 2DOF bidimensional wing is presented in this work where the flap becomes a 3rd degree of freedom. Figure 2.1 presents the flap-NES integrated in wing and shows the cubic relationship of the control force (F) relative to the flap angle (β). The other 2 DOFs are heave (h) and pitch (α). This work is considered as a first step toward the integration of the control device on a tridimensional aircraft

flexible wing. The structure is simplified in this way in order to carry out a first proof of concept of the control solution.

First, the experimental setup consisting of the bidimensional wing is described, as well as the instrumentation including the wind tunnel used. Next, the experimental protocol and the tests carried out are detailed, as well as the results and observations. The wing is tested without wind for structural characterization and with increasing wind speed in order to identify the flutter instability. The flap is blocked as the reference test case of the wing without control systems. The bidimensional wing is observed to present classic flutter by modal coalescence. Finally, the system is tested with the flap-TMD and with the flap-NES consecutively and proof of the instability control is achieved compared to the reference test case. The flap-TMD and the flap-NES control capacities are also compared.

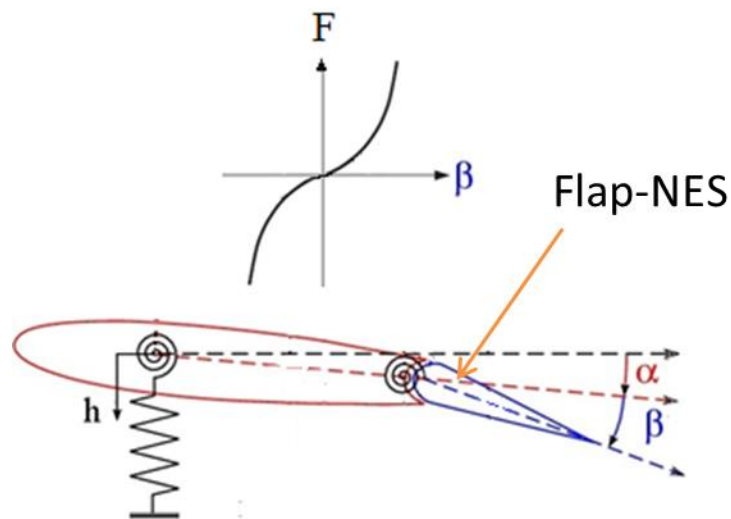


Figure 2.1: Flap-NES concept in a bidimensional wing, showing the cubic relationship of the control force (F) relative to the flap angle (β)

2.2 Experimental setup

In this section, the experimental setup is presented including the wind tunnel where the tests were carried out and its characteristics, the bidimensional wing itself and the mechanism which lies outside the wind tunnel and enables the movement of the wing. The flap-NES is presented and the way in which the cubic stiffness is generated is introduced.

2.2.1 Wind tunnel

The wind tunnel (fig. 2.2) used to carry out the tests is a low Reynolds, closed loop Prandtl Tunnel at atmospheric pressure. The tunnel has a total length of 2.4 m, a rectangular section of 1.2 x 0.8 m and its contraction ratio is 9. The speed range of the airflow is up to 25 m/s and the turbulence rate is below 0.1%.

Two pitot tubes are used to measure wind speed in the tunnel, one on each side upstream of the wing, and they are connected to a static Kimo CP300 pressure probe. The measuring range of these probes is 0-50 m/s which is more than enough for the velocity range of the wind tunnel. The actual sensitivity of the pitot tubes is 0.015 m/s.

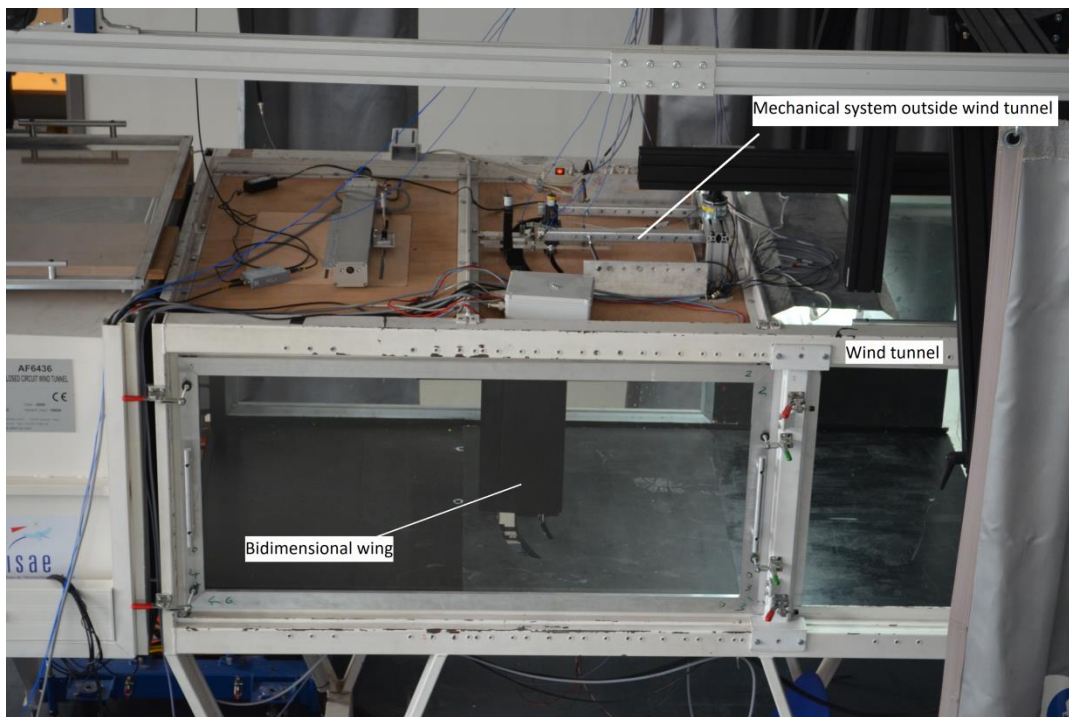


Figure 2.2 : The experimental wind tunnel setup

2.2.2 2D wind setup

The setup consists of a rigid wing with a flap that spans the entire wingspan. The wing is placed vertically, and is able to move on rails attached to the wind tunnel floor and ceiling to reproduce 2D wing aerodynamics. The wing has a chord of 0.25 m, a wingspan of 0.78 m and a total weight of 2.675 kg. The profile chosen is a NACA 0012. The wing has a steel cylindrical

spar, placed at 25% of the chord, which has a length of 1.1 m and a diameter of 0.012 m. Another steel spar with a length of 1.1 m, diameter of 0.006 m and weight of 0.510 kg is placed at 75% of the chord and enables the rotation of the control surface. There is a mechanical clearance of 0.003 m between the flap and the wing to prevent dry friction between the two. Metal ribs, carbon stiffeners, a filler foam and double-row ball bearings ensure the rigidity of the wing. A CAD view of the setup is shown in fig. 2.3.

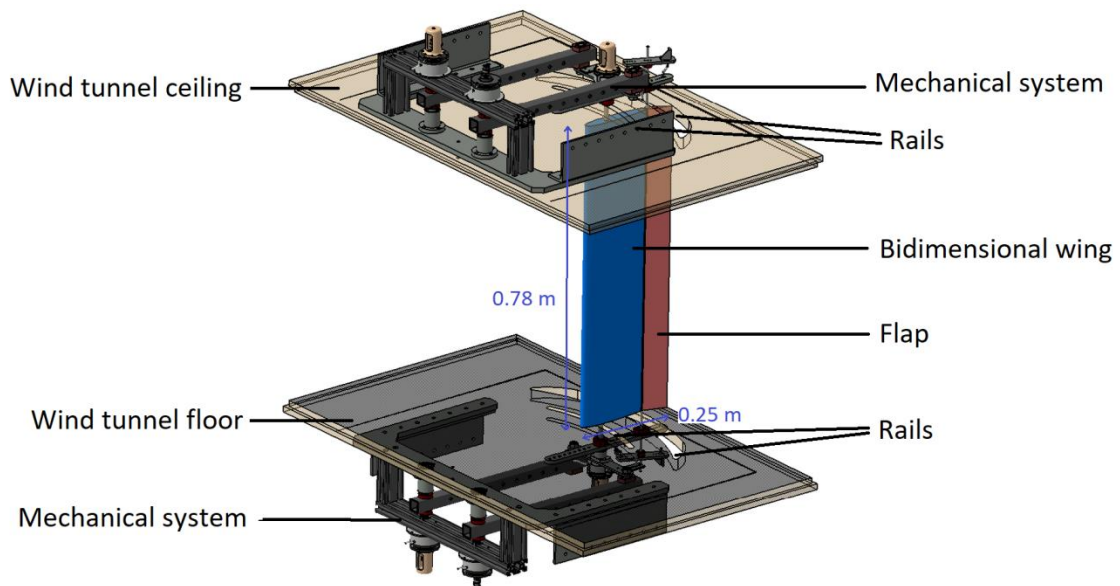


Figure 2.3 : CAD view of the 2D wing setup

In order to enable the movement of the wing, there is a mechanical system placed above and below the wind tunnel so that it has no influence on the airflow. The mechanical system can be divided into three subsystems, each one being responsible for one of the DOFs (see fig. 2.4). Note that these subsystems come in mirror image pairs located at each end of the wing creating a vertically symmetrical setup. First, the heave (h) system is made up of three bars (green in fig 2.4b) with the wing spar attached to the central bar. The torsional stiffness can be varied by putting different springs between the bars and the fixed rigid frame, and by varying their location using 7 different hole pairs on the frame (visible on fig. 2.4a. Since the bars used for h are long (0.53 m), the movement can be associated to a classical heave translation, although the actual movement is a rotation expressed as $h(^{\circ})$. For the pitch (α) subsystem, one bar (blue) is connected to the spar and follows the rotation of the wing around the spar axis. Pitch stiffness can be varied

by changing the traction springs between the pitch bar and the heave system. Finally, to allow the flap rotation (β), one bar (red) is connected to the flap's spar and follows the rotation of the flap.

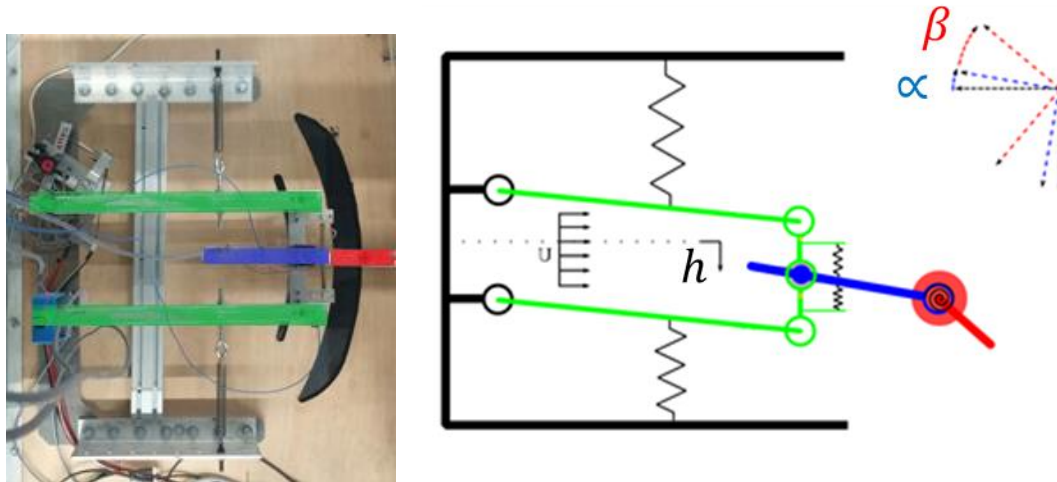


Figure 2.4 : Mechanical system. a) View from under the wind tunnel b) Diagram

2.2.3 Flap

The stiffness of the flap can also be changed by modifying the spring configuration: using torsional springs for a linear flap behavior (TMD) as in fig. 2.5, or using traction springs placed in parallel in order to have nonlinear stiffness when the flap is used as a NES. The way in which the cubic stiffness is obtained geometrically is presented in fig. 2.6 in a basic spring-mass system.

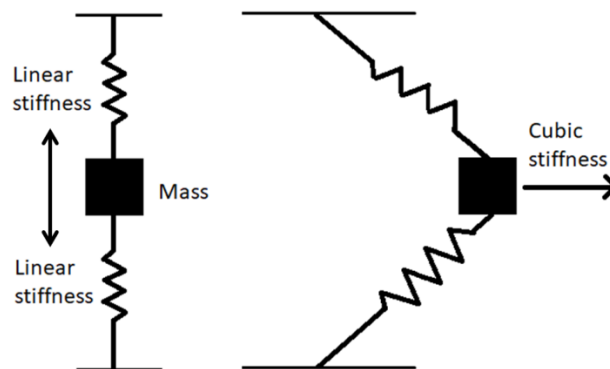


Figure 2.5 : General mass spring system with resulting cubic stiffness schema

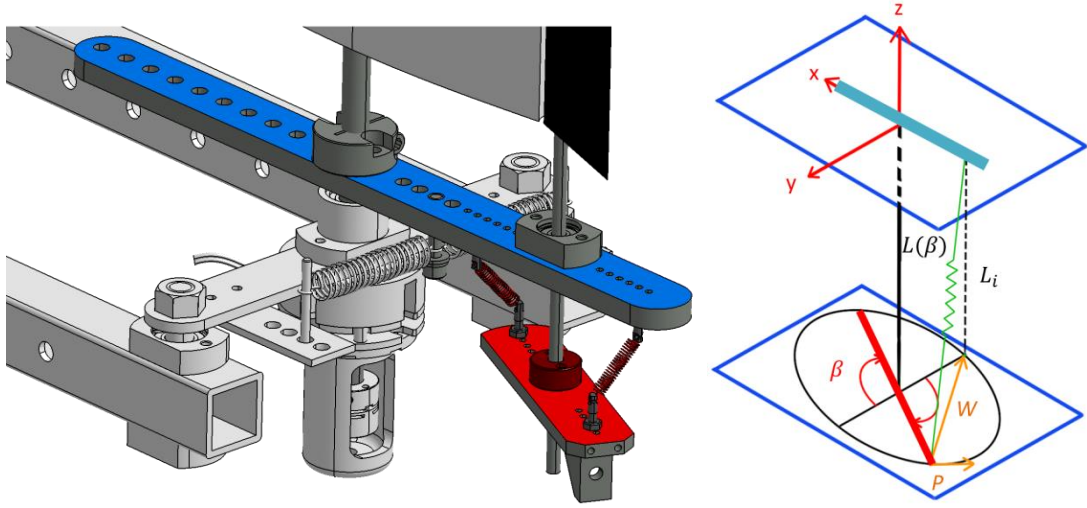


Figure 2.6 : Flap-NES design. a) CAD view b) Schema

Figure 2.6 a presents a close-up CAD view of the flap mechanical subsystem, initially presented in fig. 2.4b, this time, equipped with a nonlinear stiffness obtained by parallel traction springs. Similarly to fig. 2.4b the pitch subsystem is identified in blue and the flap subsystem is identified in red. In fig. 2.6b, when the angle of rotation (β) of the flap-NES is zero, the traction spring is parallel to the rotation axis and at a distance L_{nes} from the axis. The initial length of the spring is L_i . The spring constant is K_u and its unstretched length is L_o . The length of the spring at any given position β is $L(\beta)$. The force F generated by the spring creates a moment, M , around the rotation axis. This moment M is found by projecting the force F onto the plane containing the flap subsystem (xy plane), giving force W , whose tangential component (P) multiplied by L_{nes} gives the moment.

$$M = L_{nes}(K_u(L(\beta) - L_o) \frac{L_{nes}}{L(\beta)} \sin(\beta)) \quad (2.1)$$

where $L(\beta)$ is given by:

$$L(\beta) = \sqrt{L_i^2 + 2L_{nes}^2 + 2L_{nes}^2 \cos(\beta)} \quad (2.2)$$

The cubic term then arises from the Taylor development of fourth order of this moment M , resulting in:

$$M = -k_1\beta - k_3\beta^3 + o(\beta^4) \quad (2.3)$$

In the case where the initial spring length is equal to the unstretched spring length, the linear terms of the Taylor development disappear and only the cubic term remains. The general equation of the flap-NES is then:

$$I_\beta \ddot{B} + B_s \dot{B} + k_1 B + k_3 B^3 = 0 \quad (2.4)$$

where k_1 is the linear stiffness constant, k_3 is the cubic stiffness constant and B_s is the linear damping of the flap. The flap-NES developed is not purely cubic and therefore technically a NLTMD. The decision to call the device flap-NES in this paper arises from the fact that although not purely cubic, the stiffness is strongly nonlinear.

The flap-TMD has the same general equation as the flap-NES, only this time $k_3 = 0$, since its stiffness is purely linear.

2.2.4 Instrumentation

In order to start a test, an initial condition must be imposed to one or more DOF. This is done by a system of electromagnetic brakes which enable to fix the position of the wing and to release it at the start of a test. These brakes also have a security function and serve to stop the tests when required. The different DOF can also be fixed permanently with metal spars during the test in order to vary the number of DOF.

Two types of sensors are used on the structure: position sensors and acceleration sensors. Figure 2.7 shows their location. The position sensors used are inductive rotation sensors with reference R120LC from the brand “te connectivity”. They have a measuring range of $\pm 60^\circ$ and a maximum linearity error of 0.2%. A pair of sensors (one above and another below) is placed on each subsystem corresponding to each DOF. Measuring the angular displacement on both sides of the wing enables to ensure that there are negligible differences in torsion or flexion along the length of the wing. Three acceleration sensors (one for each DOF) are placed at the top

of the wing. The sensors, PCB 070A02, have a measuring range of ± 5 g for a [0.5, 3000] Hz frequency range. The actual sensitivity of all the sensors used is given in table 2.1.

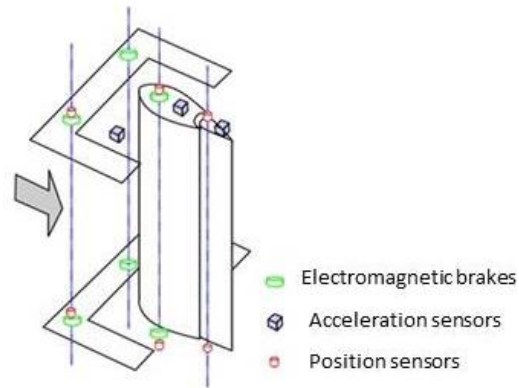


Figure 2.7 : Diagram of the sensor distribution in 2D wing

Table 2.1 : Actual sensitivity of sensors in 2D wing

Sensor type	Position	Sensitivity	Unit
Acceleration	h	984	mV/g
Acceleration	α	1017	mV/g
Acceleration	β	1000	mV/g
Displacement	h above	33.9	mV/°
Displacement	α above	33.1	mV/°
Displacement	β above	34.3	mV/°
Displacement	h below	33.6	mV/°
Displacement	α below	32.4	mV/°
Displacement	β below	33.0	mV/°

2.3 Results

This section contains the results of the experimental campaign which are divided into “zero wind speed tests” and “variable wind speed tests”. The first enable the wing structure to be characterized by identifying its natural frequencies, as well as to ensure the 2D behavior of the wing. The variable wind speed tests provide observations about the sub flutter regime and identification of the flutter speed, and allow observations about the post flutter speed regime. As

mentioned earlier, all tests are carried out for the three configurations: 2DOF (blocked flap), flap-TMD and flap-NES.

2.3.1 Zero wind speed

First, each of the three wing's degrees of freedom was characterized by obtaining their natural frequencies and stiffness in zero wind speed conditions. This was done by blocking two DOFs and imposing an initial condition to the third DOF in order to obtain a 1 DOF damped free oscillating response. Three different initial conditions were imposed with the system's breaks. The tests were repeated twice for each initial condition for H and for A. The natural frequencies and the damping are obtained by curve fit using the damped harmonic oscillator equation:

$$z(t) = Ce^{-\zeta\omega t} \sin(\sqrt{1 - \zeta^2}\omega t + \varphi) \quad (2.5)$$

Where ω the natural frequency, ζ is the damping ratio, C is a constant and φ the phase angle. Figure 2.8 gives an example of the fitted α damped curve.

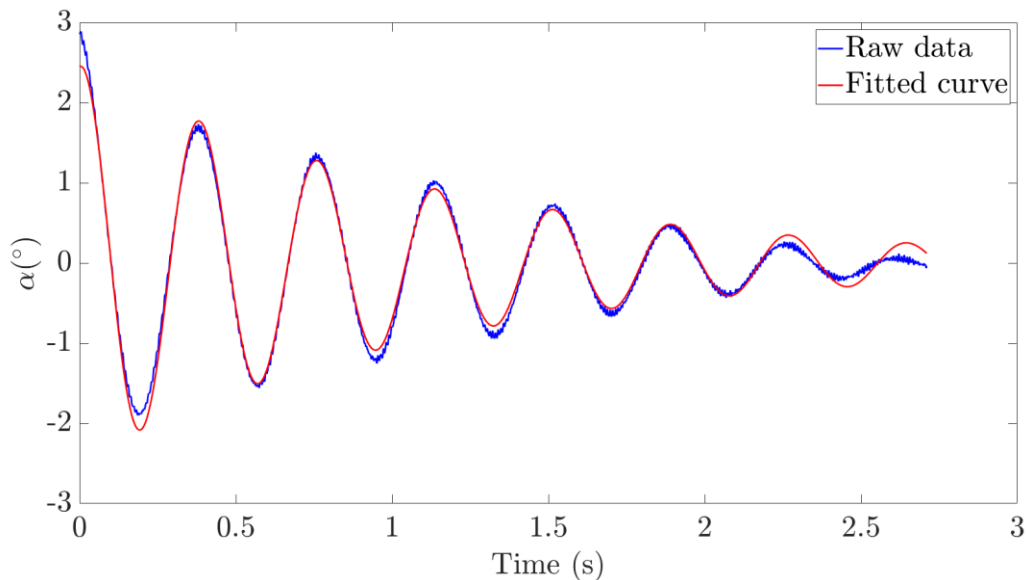


Figure 2.8 : A sensor signal and fitted damped sinusoidal function comparison.

The fit function gives a value of frequency and of damping with their 95% confidence bounds. The average value for each DOF is given for the frequency in table 2.2, as well as the maximum/minimum values.

Table 2.2 : Natural frequencies and damping coefficient of each individual DOF

	ω (min, max)	ζ (min, max)
h	1.42 (1.34, 1.47)	0,080 (0.074, 0.094)
α	2.62 (2.59,2.65)	0,041 (0.031, 0.053)

Table 2.2 does not present values for β (linear or nonlinear), as the vibration is highly damped and therefore difficult to characterize. Additionally the equation used for fitting, the damped harmonic oscillator equation, is not valid for the nonlinear β configuration. Also since β has no electromagnetic brake, the initial condition is difficult to impose. Figure 2.9 shows the response of the linear and nonlinear β to an initial displacement manually imposed.

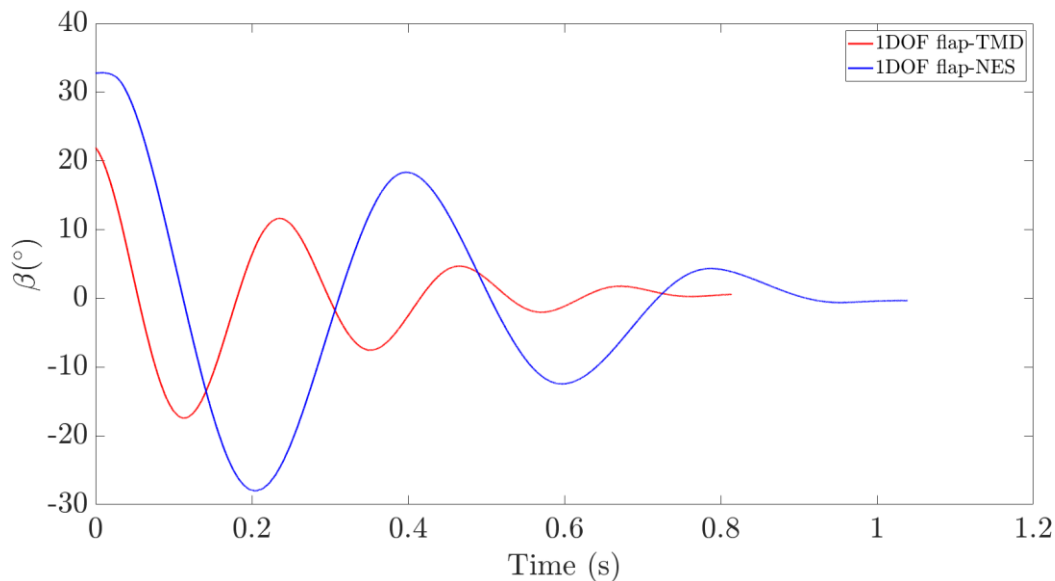


Figure 2.9 : Response of the flap-TMD and flap-NES to a manually imposed initial displacement in zero wind speed

These 1DOF tests are also used to compare the rotation measurements on top and beneath the wing which show the wing always to be in the same vertical plane with negligible (less than 5%) out of phase behavior from the upper and the lower wing, as shown in fig. 2.10. This is

important as all 3D effects are to be avoided. With this verification done, from this point onwards, only the upper sensors measurements are analyzed.

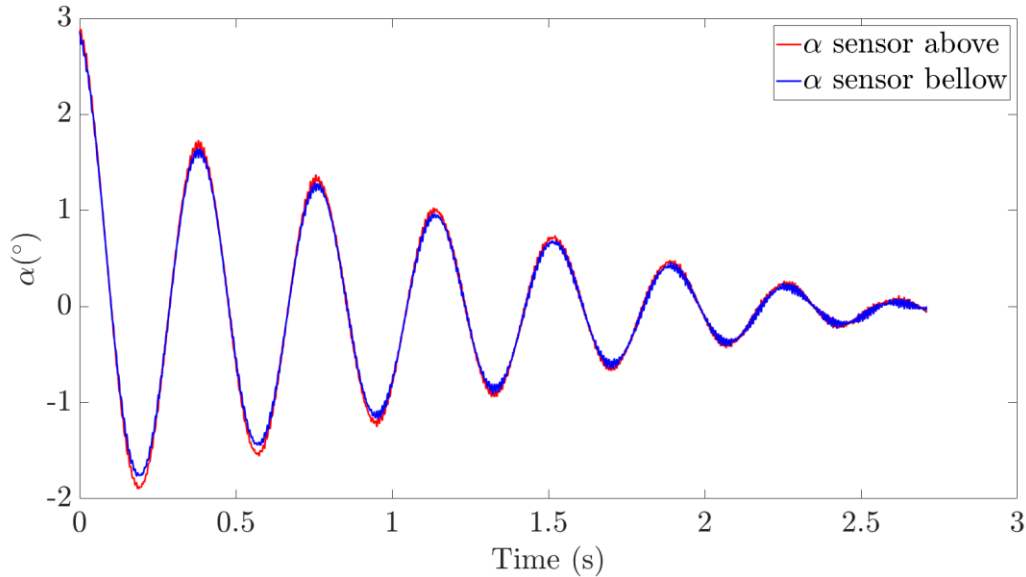


Figure 2.10 : Comparison of alpha rotation sensor signal above and below wind tunnel

2.3.2 Varying wind speed

Next, tests are carried out with varying wind speed, in the 2DOF configuration (β , the flap, is blocked) and in the 3DOF configurations which are the linear flap-TMD case and the nonlinear flap-NES. The first objective of these tests is, once the individual 1DOF frequencies have been obtained, to determine if these frequencies vary with wind speed and if so, what is the interaction between each DOF for the different cases.

2.3.2.1 Flutter speed

Figures 2.11, 2.12 and 2.13 present the evolution of the frequency of each DOF for 2DOF, flap-TMD and flap-NES configurations respectively. In these figures, it is observed that as the wind speed increases, the oscillation frequencies get closer to one another until modes h and α coalesce. This means that the system is presenting classic flutter. Similarly to the 1DOF characterization, the frequencies are obtained via curve fitting of the given function. The curve fitting function gives the values within error bars of 95% confidence which are of the order of $\pm 0.05\%$ and therefore not visible on the plots. As observed in these three figures, the wind speed at

which coalescence occurs varies in the three cases. The wind speed at which h and α frequencies coalesce (identified with a vertical red line in figs. 2.11, 2.12 and 2.13 helps identify the range of wind speeds in which the flutter speed U_F appears. This range of wind speeds is presented in table 2.3. It is observed that both the flap-TMD and the flap-NES increase flutter speed by 3% to 16%.

Table 2.3 : Range of wind speeds in which flutter speed (U_F) appears for different wing configurations

	2DOF	Flap-TMD	Flap-NES
U_F (m/s)	13.13-13.73	14.09-15.24	14.16-15.25

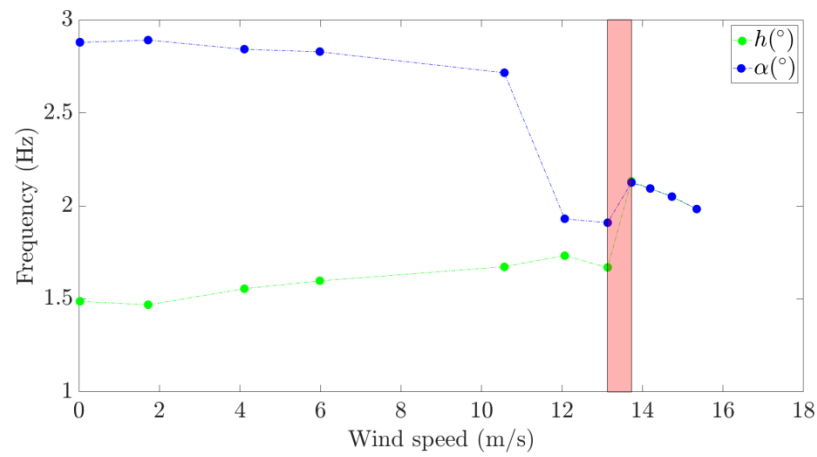


Figure 2.11 : Frequency evolution of h and α with wind speed (2DOF)

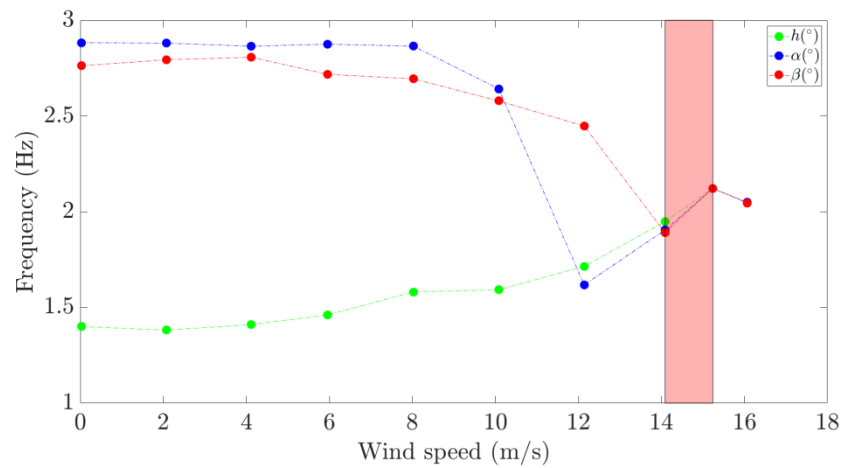


Figure 2.12 : Frequency evolution of h , α and β with wind speed in flap-TMD configuration

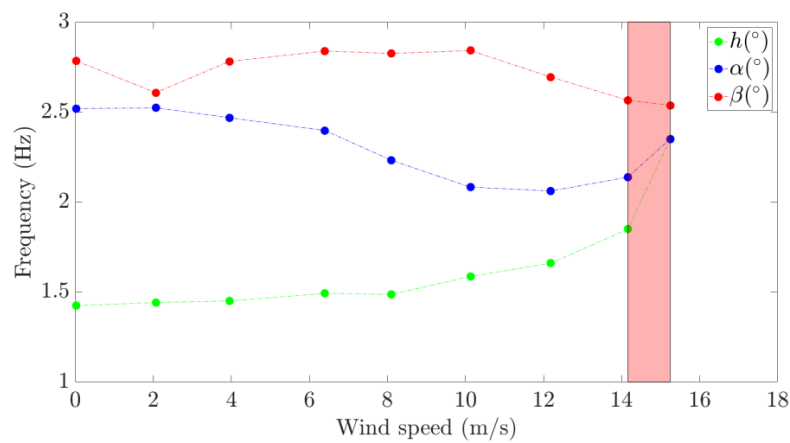


Figure 2.13 : Frequency evolution of h , α and β with wind speed in NES-flap configuration

2.3.2.2 Post flutter

Looking at the supercritical regime, although modal coalescence is observed in all configurations (2DOF, 3DOF with flap-TMD and 3DOF with flap-NES), the type of response is altered by the nonlinear character of the flap-NES. Figures 2.14, 2.15 and 2.16 show the response, at a given supercritical wind speed, of each DOF at 2DOF, flap-TMD and flap-NES configurations respectively. Figure 2.15 shows the constant amplitude LCO obtained with the flap-TMD, which is similar to LCO of the 2DOF (fig. 2.14), whereas fig. 2.16 shows a highly modulated LCO response, an inherent characteristic of NES control.

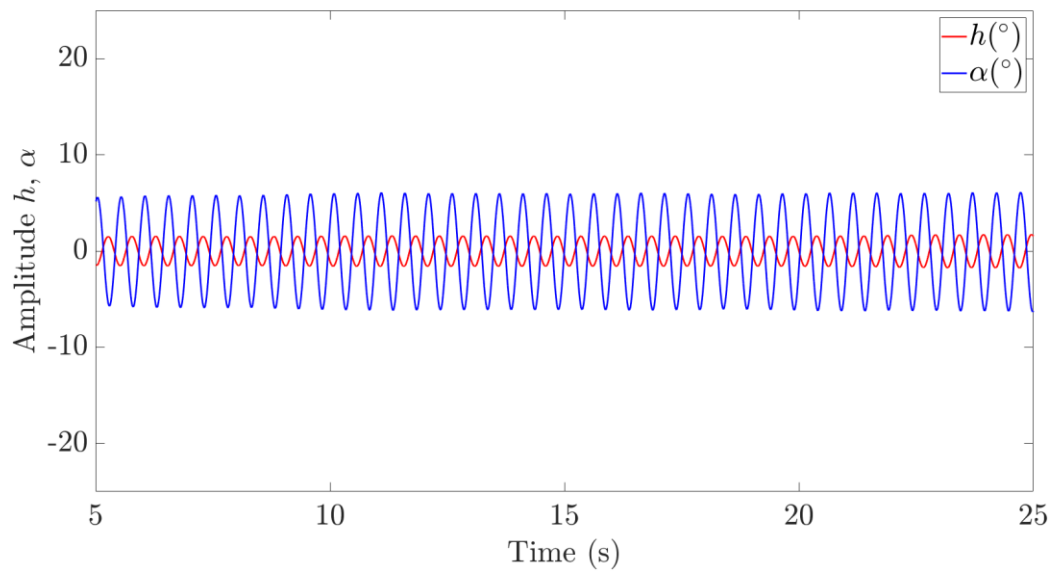


Figure 2.14 : Response of 2DOF system at wind speed of 15.35 m/s

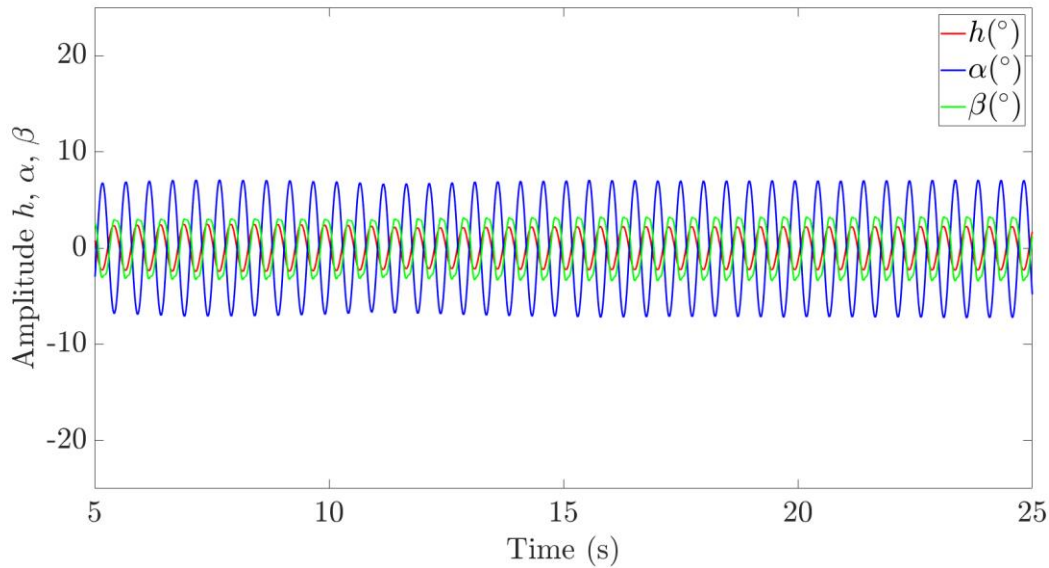


Figure 2.15 : Response of 3DOF flap-TMD system at wind speed 16.09 m/s

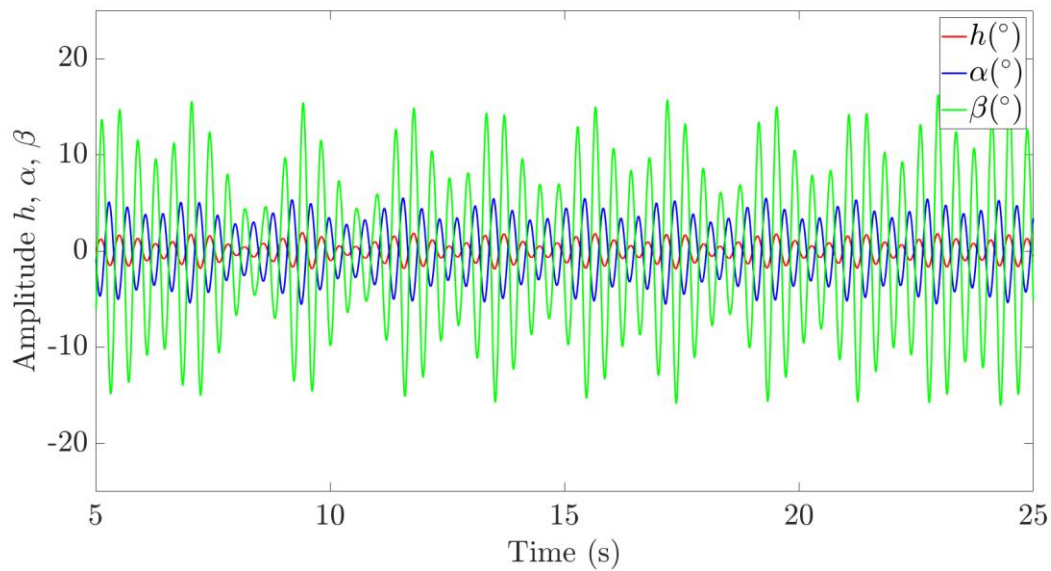


Figure 2.16 : Response of 3DOF flap-NES system at wind speed 16.20 m/s

By obtaining the average peak amplitude of these LCO (by using the last 10 amplitude positive peaks when the permanent regime is established) for each DOF and each configuration, figs. 2.17, 2.18 and 2.19 are obtained. The 3DOF flap-NES case which presents a modulated response is given as a range of LCO peak amplitudes (see green area in the figures). It is observed that the flap-TMD reduces the vibration amplitude of the wing (by reducing both h and

α) at any given post flutter wind speed. However, greater LCO reduction is obtained with the flap-NES, showing it to be a better solution for post flutter speed control. The flap-NES, as mentioned, changed, at high speed, the response from constant amplitude LCO to a modulated one which, most importantly, has lower average amplitude. Moreover, it is observed in figs. 2.17 and 2.18 that the 2DOF configuration test had to be stopped at a lower wind speed than the other two configurations. This is due to safety reasons as the high amplitude LCO could cause structural damage to the wing. However, following the tendency displayed, the amplitude decrease caused by the control system continues to grow with increasing wind speed. Figure 2.19 shows an increase in the average flap-NES amplitude for all wind speeds, with respect to the average flap-TMD amplitude, meaning that greater energy was lost from H and A and transferred to the flap which, in turn, is mitigated it to the surrounding airflow.

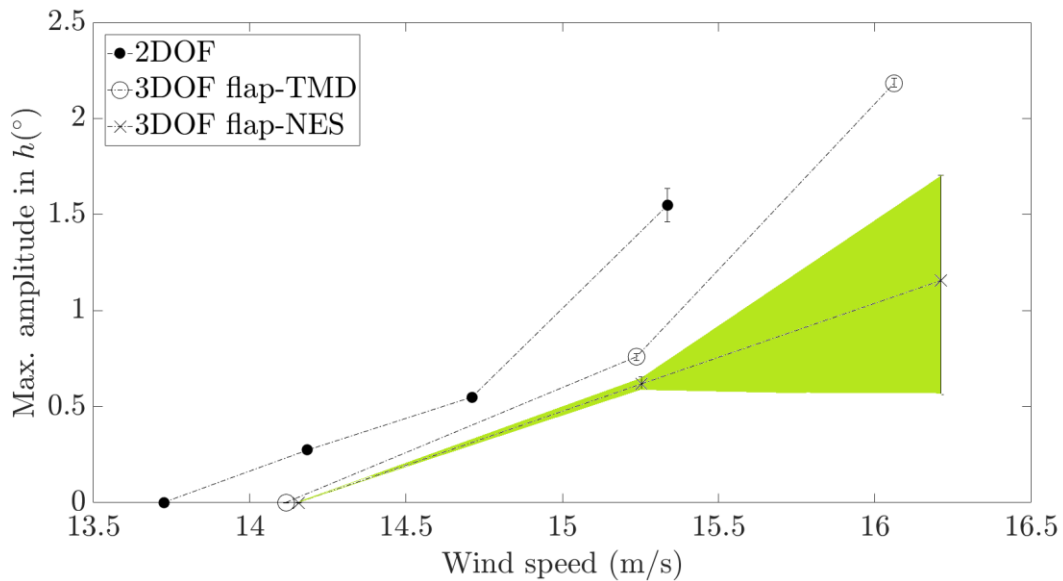


Figure 2.17 : Average LCO peak h amplitude

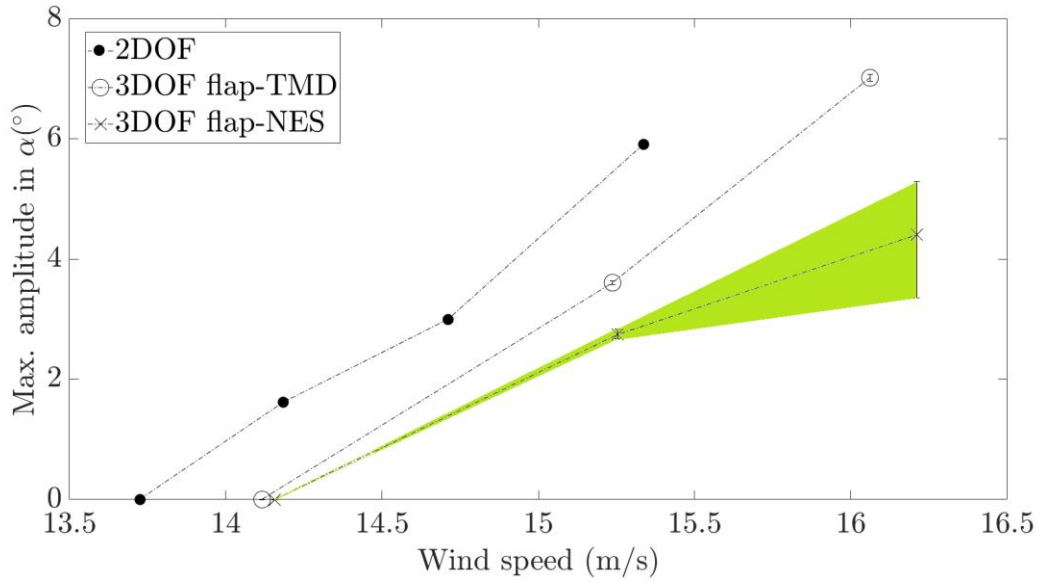


Figure 2.18 : Average LCO peak α amplitude

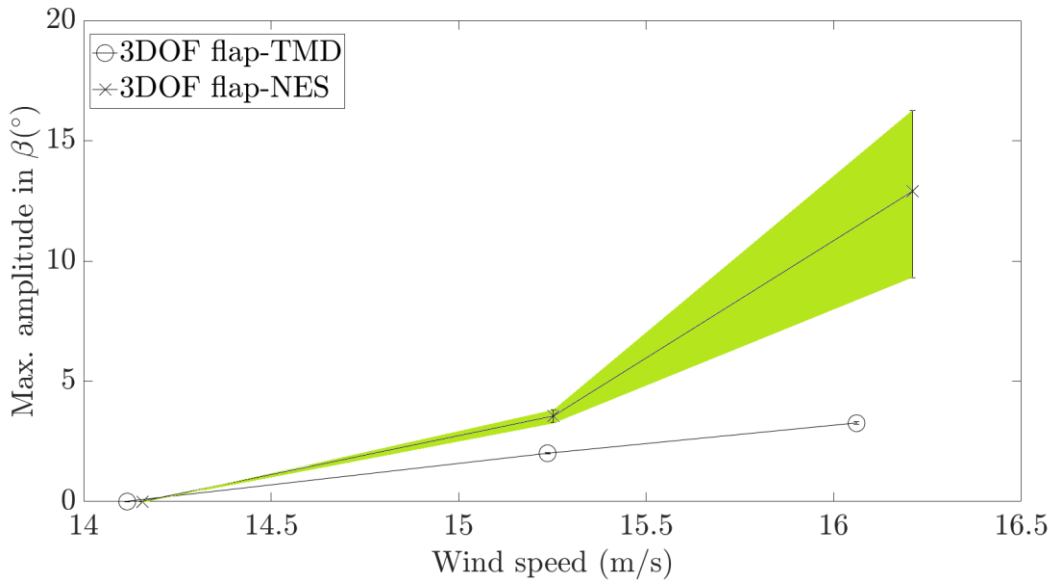


Figure 2.19 : Average LCO peak β amplitude

The energy transfer effect may be estimated by considering the total signal energy, obtained by adding the signal energies of h and α , and comparing the given values for each of the three configurations (2DOF, flap-TMD and flap-NES) at given wind speeds. This enables a comparison between the constant amplitude LCO (2DOF and flap-TMD) and the modulated LCO

(flap-NES). The signal energies are obtained by time integration of the square of each sensor signal and, once added, are used to approximate the total energy of the system:

$$E = \int [h(t)]^2 dt + \int [\alpha(t)]^2 dt \quad (6)$$

Where $h(t)$ and $\alpha(t)$ are the sensor signals and E is the total signal energy.

The comparison of the different configurations shows up to 61% energy reduction using the flap-TMD, as compared to the 2DOF case, and up to 79% energy reduction using the flap-NES, as compared to the 2DOF case.

2.4 Conclusion

In this work, a solution for passive flutter control is presented. It consists of integrating a passive control device which acts as a secondary mass damper and mitigates energy from the main system, when properly tuned. A flap-NES is created by introducing a flap with nonlinear stiffness. The device is efficient for broadband frequencies which is ideal in the aeroelastic case where wing frequencies can be wind speed dependent. The flap-NES, which is also tested in its linear variant as a flap-TMD, is integrated in the bidimensional wing, therefore becoming its third degree of freedom. The paper describes an experimental proof of concept of the device on a bidimensional wing in a wind tunnel.

The setup is first characterized in zero wind speed conditions. Second, its dynamic response to varying wind speeds is obtained. The evolving response is identified as classic flutter caused by modal coalescence of the heave and pitch modes.

The effectiveness of the flap-TMD and the flap-NES in passively controlling the flutter instability on the bidimensional wing in the wind tunnel is observed. The flutter speed is increased by 3 % to 16% respect to the baseline system by using both the flap-TMD and the flap-NES. Once in the post-flutter regime, the LCO signal energy is reduced by up to 61% by the flap-TMD. The flap-NES showed greater control effectiveness in the post-flutter regime with a LCO signal energy reduction of up to 79%.

Overall this work presents and characterizes the effectiveness of a new solution for passive aeroelastic control which can be easily integrated in wings with little added mass and placed in the wind flow to benefit from wind speed dependent properties and additional aerodynamic damping. The capacity of the flap-NES of acting as a secondary oscillator and absorbing energy from the main structure in this context has been highlighted. In the case presented, high amplitude LCOs which could lead to eventual structural failure by fatigue are avoided with the flap-NES configuration.

Regarding the perspectives of this work, now that the proof of concept has been made on a bidimensional wing, the flap-NES will be tested experimentally on a tridimensional wing. In parallel, analytical and numerical methods are developed to enable the design and optimization of this passive control solution.

Acknowledgements

The authors would like to acknowledge the Natural Sciences and Engineering Research Council of Canada, the Canada Research Chair program, the French Initiative d'Excellence (IDEX) and the Université de Toulouse for the funding. The work greatly benefited from the expertise of the technical team and, in particular, Rémy Chanton, Leonardo Sanches, Jean-Benoit Alibert and Henri Dedieu.

**CHAPTER 3 ARTICLE 2: PASSIVE CONTROL OF VORTEX
INDUCED VIBRATION IN FLEXIBLE WING USING NONLINEAR
FLAP**

**FERNANDEZ-ESCUADERO, C., PROTHIN, S., LAURENDEAU, E.,
ROSS, A., MICHON, G., Submitted to Journal of Aircraft**

In the previous chapter, a proof of concept was obtained of flap-NES in passively controlling the aeroelastic behavior of a bidimensional wing. The bidimensional wing is the simplest approximation of an aircraft wing so it was logical to use this system as a first step. However, it is limited as tridimensional effects are not taken into consideration. The tridimensional effects may affect the aeroelastic behavior of the wing but, most importantly, affect the design of the flap-NES. The idea in a real aircraft wing is that the flap only occupies a small portion of the wingspan, having a much localized action. This gives rise to the second experimental journal article where the innovative control solution is tested on a tridimensional wing, closer to a real aircraft wing. The flap-NES now has a localized nonlinear action, as it only occupies a portion of the wing span. It is placed in the wing tip as to maximize its effect on the wing structure. The first objective is to validate the hypothesis that this flap-NES design will also achieve aeroelastic control.

The tridimensional wing presents limit cycle oscillations in the wind tunnel. Again, proof of concept is achieved: the wing presents lower energy when the flap-NES is present.

A second objective is to evaluate the importance of the correct design flap-NES in its control capacity. The hypothesis is that since the flap-NES is nonlinear its optimization is challenging. The influence of dynamic parameters in the wing and in the flap-NES is tested. The results highlight the sensitivity of the control ability to the parameters and therefore the need of a complementary approach to further develop and optimize the flap-NES. The response to this need is shown in chapter 4 with the development of numerical methods.

FERNANDEZ-ESCUDERO, C., PROTHIN, S., LAURENDEAU, E., ROSS, A., MICHON, G., “*Passive control of vortex induced vibration in flexible wing using nonlinear flap*” Submitted to Journal of Aircraft, 2021

Abstract. A solution for aircraft wing aeroelastic control is presented and tested experimentally on a 3D wing test bench. The wing presents vortex induced vibrations and the objective is to reduce the limit cycle oscillations. The control solution consists of a flap integrated in the wing which acts as a secondary mass damper. The flap acts as a NES (nonlinear energy sink) which has a nonlinear stiffness. Its stiffness and damping are therefore dependent of wind speed. This feature makes the flap-NES well adapted for aeroelastic control. The control system is passive, which makes it safe in emergency cases, and adds little mass to the system. The flap-NES is tested in ground vibration test and in a wind tunnel on a 3D flexible wing. The vibration dissipation qualities of the flap-NES are highlighted and its ability to control vortex induced vibrations is demonstrated.

3.1 Introduction

Aeroelasticity is a main limiting factor in aircraft design as it can cause unstable responses, high amplitude vibration and other undesired effects. Many attempts have been and still are being developed in order to control aeroelastic phenomena. The purpose is to enlarge flight envelopes, to avoid fatigue problems and, more recently, to enable the development of more flexible wings, innovative aircraft and drone designs.

Aeroelasticity control can be active or passive. Active control can include the use of piezoelectric materials [89] and morphing control [90]. Vibration mitigation can be achieved passively through the materials of the structure. For example, viscoelastic materials are efficient in vibration mitigation and reasonably easy to install in existing structures [15]. In [16], experiments were carried out on a 2 DOF aeroelastic test bench using shape memory alloy springs. Flutter speed was increased, limit cycle oscillation (LCO) amplitude decreased and the rate of energy mitigated was very high compared to other solutions; however, the solution is dependent on vibration frequency.

Passive control via dynamic absorbers is also efficient in this context and is the focus of the present work. A way to classify secondary absorbers is by their stiffness which can be linear or nonlinear. This will determine their behavior and therefore their scope of applications. Linear stiffness secondary absorbers are Tuned Mass Dampers (TMDs). They are simple to design but add significant mass in order to be efficient (10% of the modal mass of the targeted mode [91]) and are only efficient for dissipating energy around a single targeted frequency. They are widely used in civil applications, for example in bridges [92]. However, the structural properties of a system under wind flow vary due to aerodynamic added mass, damping and stiffness. This means that having a device which targets a single frequency is not ideal. Additionally, mass is always to be minimized in the aerospace industry for power efficiency reasons.

A solution which is more adequate in an aeroelastic wing context is the Nonlinear Tuned Vibration Absorber (NLTVA) [20]. Due to its nonlinear stiffness, unlike the TMD, the NLTVA is efficient for broadband frequencies. The Nonlinear Energy Sink (NES) [79], which is the damper used in this work, is a specific kind of NLTVA which has purely nonlinear stiffness and linear damping. This absorber presents high vibration absorption capacity for a broadband frequency range and low added mass. A NES absorbs energy from the main system and mitigates it via targeted energy transfer known as energy pumping [23]. This means that it is efficient for a larger frequency band than other dynamic absorbers. This makes a NES appropriate for passive aeroelastic control. The main drawback of the device is that its efficiency is greatly dependent on its proper dimensioning due to its strongly nonlinear behavior [93]. Some of the current applications of the NES are: shock isolation [25], seismic vibration control [26], energy harvesting [94], suppression of the stick-slip phenomenon in machining [28] and control of fluid structure interactions such as transonic instabilities [34] and vortex induced vibration (VIV) [29].

VIV are oscillations of the structure in response to the Von Karman vortex street shed due to the detached flow either from a bluff body or from a streamlined body at high angle of attack. When the frequency of the VK vortices and the structure's natural frequency are very close, lock-in is observed which can lead to high amplitude oscillations [9]. These oscillations may lead to fatigue failure so their mitigation is important.

An innovative solution for controlling bidimensional wing flutter consists of a flap-NES, where the NES is integrated in the wing as a flap [41]. When placed in the wind flow, the system

benefits from aerodynamic damping and adds little mass. The flap-NES is placed at the wing-tip to maximize its effect on the structure. It is not to be confused with the active control surfaces already present in aircraft wing such as ailerons or spoilers (see fig. 3.1).

In this work, a test bench is developed with the objective of proving the physical feasibility of the flap-NES on a tridimensional wing for controlling vortex induced vibration. Ground vibration testing is carried out in order to identify the modal shapes and frequencies of the setup. The effect of the flap-NES in zero wind speed conditions is assessed. The set-up is tested in a wind tunnel and its aeroelastic behavior is identified. The capacity of the flap-NES of controlling undesired aeroelastic effects is presented. The influence of dynamic parameters in the wing and in the flap-NES is tested. The goal of this work is to carry out a proof of concept of the control solution for vortex induced vibration and to evaluate the dependence of its control capacity on structural parameters.

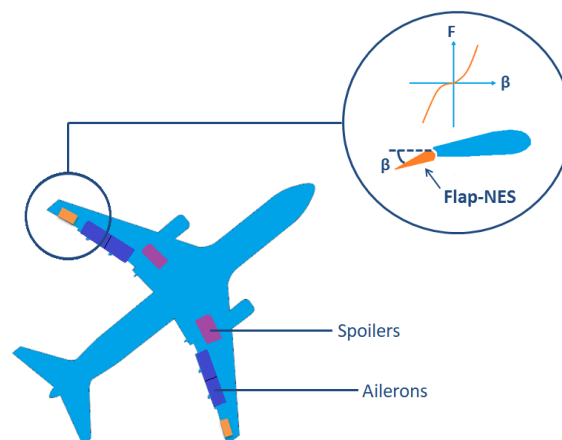


Figure 3.1 : Schema of the flap-NES concept in aircraft wing

3.2 Flap-NES

A NES is a secondary damper consisting of cubic stiffness and linear damping. Its strongly nonlinear features make the flap-NES control capacity very sensitive to its design parameters. The control solution developed in this work proposes integrating a NES as a flap in a wing in order to control its aeroelastic behavior. The way in which cubic stiffness is obtained and how the flap-NES is integrated in the experimental wing setup is described in this section.

The nonlinear stiffness of the flap is generated by placing tension springs in a parallel configuration. The geometrical nonlinear stiffness is presented fig. 3.2 in a generic mass spring system. In fig. 3.3, the CAD view of the flap-NES in the 3D flexible wing and a supporting schema are shown. The equations giving rise to the cubic stiffness are shown in equations 3.1 to 3.4.

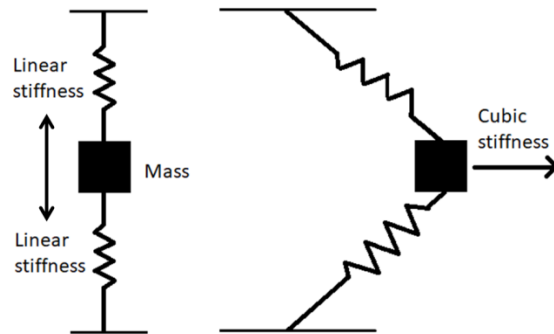


Figure 3.2 : General mass spring system (left) with resulting nonlinear stiffness (right)

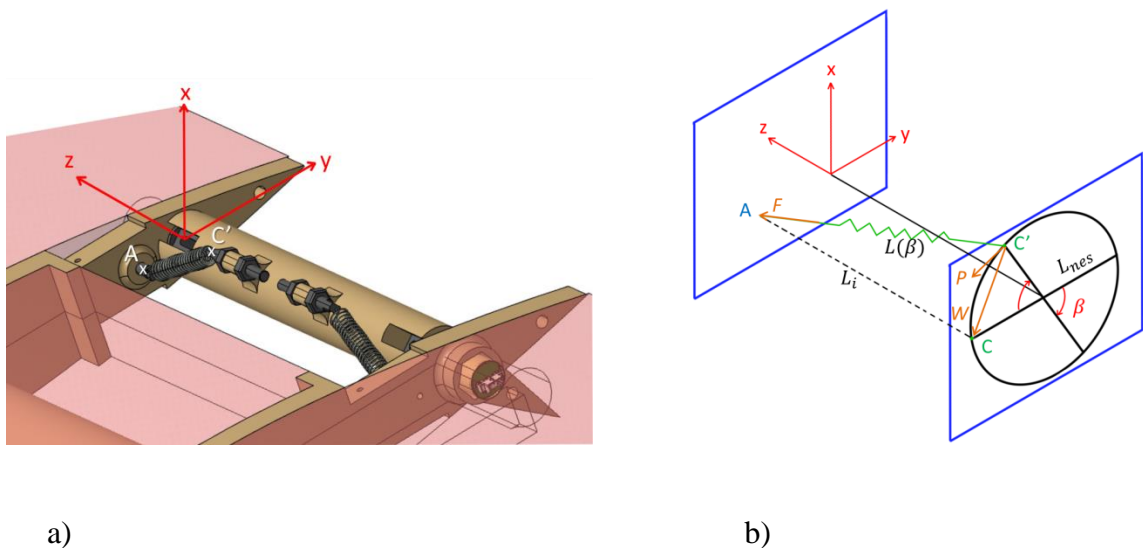


Figure 3.3 : Flap-NES design a) CAD view b) schema

In fig. 3.3b, when the angle of deflection (β) of the flap-NES is zero, the tension spring is parallel to the rotation axis of the flap and at a distance L_{nes} from it. Points A and C are contained within the zy plane and, therefore, the flap is aligned with the wing. As the flap-NES rotates, the tension spring stays fixed at one end (point A) while the other end (point C)

follows a flat circular trajectory around the rotation axis of radius L_{nes} . The initial length of the spring is L_i . The spring constant is K_u and its unstretched length is L_o . The length of the spring $L(\beta)$ at any given position is given as a function of β . The force F generated by the spring creates a moment, M , around the rotation axis. This moment M is found by projecting the force F onto the plane containing the flap subsystem (xy plane), giving force W , whose tangential component (P) multiplied by L_{nes} gives the moment:

$$M = L_{nes}(K_u(L(\beta) - L_o) \frac{L_{nes}}{L(\beta)} \sin(\beta)) \quad (3.7)$$

where $L(\beta)$ is given by :

$$L(\beta) = \sqrt{L_i^2 + 2L_{nes}^2 + 2L_{nes}^2 \cos(\beta)} \quad (3.8)$$

The cubic term then arises from the Taylor development of fourth order of this moment M , resulting in:

$$M = -k_1\beta - k_3\beta^3 + o(\beta^4) \quad (3.9)$$

In the case where the initial spring length is equal to the natural spring length, the linear terms of the Taylor development disappear and only the cubic term remains. In the case of this study, the springs are stretched at all positions so both linear and cubic stiffness remain. The general equation of the flap-NES:

$$I_\beta \ddot{B} + B_s \dot{B} + k_1 B + k_3 B^3 = 0 \quad (10)$$

where k_1 is the linear stiffness constant, k_3 is the cubic stiffness constant and B_s is the linear damping of the flap. The flap-NES developed is not purely nonlinear and therefore, technically, it is a nonlinear tuned mass damper (NLTMD). The decision to call the device flap-NES in this paper arises from the fact that although not purely cubic, the stiffness is strongly nonlinear.

3.3 Experiments

In order to carry out a proof of concept of the flap-NES and assess its control capacity, an experimental setup is developed. At this stage of the project, an experimental approach is chosen to ensure that no aeroelastic mechanism is neglected. This section presents the different parts, materials and properties of the tridimensional flexible wing for three different configurations. It provides the various tests set-ups and details the instrumentation. The characteristics of the three different wing mass configurations tested are stated. Two different flap-NES are tested by varying their properties. First, ground vibration testing enables the identification of the modal shapes and frequencies of the wing. The flap-NES is also tested in zero wind conditions during these tests. Second, the setup is tested in a wind tunnel. This set enables an aeroelastic analysis of the system's response. The flap-NES is evaluated in its capacity to control the undesired aeroelastic phenomena encountered.

3.3.1 3D Flexible Wing Set-up

The setup consists of a flexible wing which is clamped at one end and free at the other, therefore presenting full 3D structural and aerodynamic effects. The wingspan is 600 mm and the profile is a NACA0020 with a 200 mm chord. The ribs are printed in ABS (Acrylonitrile Butadiene Styrene) and the spar, placed at the $\frac{1}{4}$ chord, is made of aluminum and has a rectangular cross-section. The wing skin is made of one ply of woven bidirectional glass-epoxy composite material and a second layer of thermoplastic material which ensures the absence of porosity of the skin. The skin is attached to the wing by the ribs.

The wing has two flaps (fig. 3.4a): the one nearest to the wing tip is designed to behave as a NES. The other one is actuated and has the double function of exciting the structure and also of serving as a security system. Indeed, it can be placed very rapidly at 90° in order to exit the instability, by drastically removing the lift force if the flap-NES fails to work. The flap-NES has a span of 15 mm and therefore occupies only 7.5% of the wingspan. This enables having a localized inflow effect. The flap-NES is placed at the wing tip to maximize its effect on the wing's structural response.

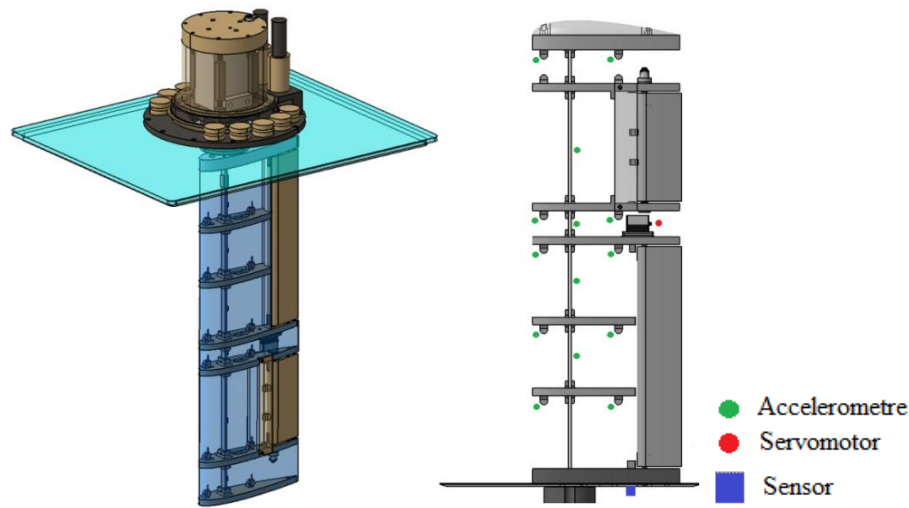


Figure 3.4 : Design of the 3D wing: a) CAD model b) Instrumentation

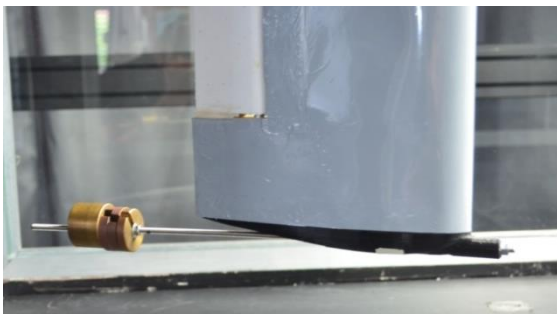
3.3.2 Instrumentation

The wing is equipped with 14 unidirectional miniature accelerometers from PCB Piezotronics, model 352A74 which measure the movement of the wing. There are 9 in the lift direction, placed on the ribs, and 4 in the drag direction, placed on the spar. The locations of the accelerometers are given in fig. 3.4b. The sensitivity of these accelerometers is 100mV/g and the measuring range is +/- 50 g pk. The angular displacement of the flap-NES and of the actuated flap is measured with miniature analogic rotary encoders MA3-A10-125-B from US digital, with 10-bit resolution. These rotary encoders are powered with 5V input. The flap closest to the wing root is actuated by a servomotor which can be controlled manually. A piezoelectric patch transducer is the P-876 DuraAct™ from PI is also placed on the wing spar (blue square in fig. 3.2) and measures the deformation of the wing. A safety limit is defined in the servomotor so that the actuated flap is automatically placed at 90° if the wing root deformation limit is surpassed.

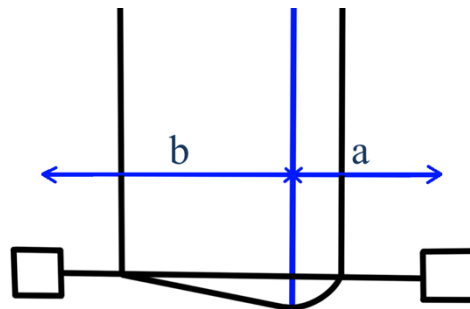
3.3.3 Wing Mass Distributions

The wings main dynamic parameters are related to its mass and stiffness. In this work, three different mass distributions for the wing structure are tested. In this way, the total mass and the position of the center of gravity are modified. By changing the mass distribution, the bending and torsion modes of the wing are modified which leads to a different vibration response. By

changing the vibration response of the wing it can be analyzed whether the flap-NES remains adapted for control or whether its control efficiency is highly dependent on the dynamic characteristics of the wing. One configuration is without added mass; for the two others, local masses are added to the wing tip either at the trailing edge or both at the trailing and leading edge (fig. 3.5a). Adding mass at the wing tip maximizes its effect on the bending and torsion modes. The modification of the wing frequencies will change its aeroelastic response in the wind tunnel. The parameters of the mass configurations are given in table 3.1, including the added masses and the distance from their center of mass to the wing spar, as shown in fig. 3.5b. The masses are screwed on to a threaded shaft which is inserted through a wing tip designed for this purpose and screwed again to the wing to lock their position. Mounting masses in this way is not ideal from an aerodynamics point of view, but it enables to modify the bending and torsion modes by not only adding local masses but also controlling their locations. However, their effect on the aerodynamics can be considered negligible as the tests are carried out at high angle of attack and the flow will be detached.



a)



b)

Figure 3.5 : System used to add masses to the leading edge and/or the trailing edge a) image b) schema of parameters

Table 3.1 : Different mass configurations

Config. num.	a (mm)	Mass(g)	b(mm)	Mass(g)
1	n/a	n/a	n/a	n/a
2	n/a	n/a	208	638
3	81	349	158	299

3.3.4 Flap-NES Configurations

The tension springs in the flap-NES can easily be changed through a small trap placed on the side of the wing, in order to test different NES stiffnesses. The stiffness of the NES is an important parameter which affects its control effectiveness. Additionally, the flap can be completely blocked by using a small metal rod, enabling the comparison of the response with and without flap-NES.

Two different flap-NES configurations are tested. The springs used are from Misumi and their references, spring constant (K_u) and length (L_o) as given by the provider can be found in table 3.2. Note that the spring constant K_u appears in equation 1 and is not to be confused k_1 and k_3 which are the linear and nonlinear stiffnesses respectively of the NES once its geometry is considered. Previous work within the research program enabled to select an adequate range of spring parameters for the design of the NES considering the wing's characteristics. In the two flap-NES configurations the springs are always stretched giving rise to a linear component, as explained in section 3.2. NES A is stiffer than NES B. Using springs with different properties enables to see the effect of different NES on the response of the system. This will show if the control capacity of the flap-NES is greatly dependent or not on its stiffness.

Table 3.2 : Springs used in flap-NES

Flap-NES config.	Spring reference	K_u (N/mm)	L_o (mm)
Flap-NES A	UFSP8-0.8-14	0.16	14
Flap-NES B	UFSP6-0.6-17	0.09	17

3.3.5 Ground vibration tests

Before the wind tunnel testing, modal analysis of the wing in the different configurations is carried out by placing the wing on a 10kN electrodynamic shaker from Brüel & Kjaer (LDS V830-335), as shown in fig. 3.6. The shaker is controlled with LMS Test Lab using the Sinus Control module. Frequency is swept from 5Hz (the minimum frequency allowed by this shaker) to 60Hz with controlled input amplitude of both 0.05g and 0.1g. The frequency resolution is 0.01 Hz. Additional instrumentation is required for the ground vibration test (GVT) as reference. This consists of a control accelerometer placed on the shaker below the wing and a triaxial accelerometer placed on the disk attached to the wing. The PCB Piezotronics 333B50 control accelerometer has a sensitivity of 1029 mV/g, and the 356B21 triaxial accelerometer's sensitivities are 10.26, 10.12, 10.15 mV/for each of its axis. The data from the 14 accelerometers inside the wing, the control and the triaxial accelerometers and the analogic rotary placed in the flap is collected through LMS test lab. The results from this test are presented in section 3.4.1.



Figure 3.6 : 3D Wing setup mounted on shaker a) without skin b) with skin

3.3.6 Wind tunnel testing

The wind tunnel (fig. 3.7) used to perform the tests is a low Reynolds, closed loop Prandtl tunnel operating at atmospheric pressure. The tunnel has a total length of 240 mm, a rectangular section of 120 x 80 cm and its contraction ratio is 9. The speed range of the airflow is up to 25 m/s and the turbulence rate is below 0.1%.

Two pitot tubes are used to measure wind speed in the tunnel, one to the right and another to the left side, upstream of the wing, and they are connected to a static Kimo CP300 pressure probe. The measuring range of these probes is 0-50 m/s which is more than enough for the velocity range of the wind tunnel. The sensitivity of the pitot tubes is 0.015 m/s. The data from the 14 accelerometers inside the wing, the analogic rotary placed in the flap and the pressure probe data is collected through LMS test lab.



Figure 3.7 : a) Wind tunnel used for tests b) wing in wind tunnel

3.4 Results

The results of the tests carried out on the tridimensional wing with its three mass configurations and its different flap-NES are presented, as well as the blocked flap-NES cases for comparison purposes. The wing is first tested in ground vibration test by considering only the wing and its interaction with the flap-NES. The structure is then set up in the wind tunnel in order to introduce aerodynamic forces and resulting fluid structure interaction. As the wind speed changes, the wing's and the flap-NES's structural properties vary due to added aerodynamic mass, damping and stiffness. Therefore, the system with and without wind is considered separately and no analogous effect of the flap-NES is expected.

3.4.1 Ground vibration tests

The different configurations are tested on the electrodynamic shaker in order to identify the system's natural frequencies and modes for the different mass distributions and the effect of the different flap-NES in the responses.

3.4.1.1 Effect of the added mass in blocked flap-NES configuration

The three different mass configurations presented in table 3.1 are tested in the blocked flap-NES configuration, in order to quantify the effects of the added masses on the natural frequencies. The frequencies of the lift and drag bending modes and the torsion mode are presented in table 3.3. The corresponding mode shapes, extracted from the accelerometers'

frequency response functions, are shown in fig. 3.8. In figs. 3.8a and 3.8c, the colors represent the deformation outside the wing's plane at rest. Note that only the four accelerometers placed in the drag direction on the wing spar are represented in fig. 3.8b. In this case, the deformation of the wing spar within the wing's plane is observed from above. The frequency sweeps are carried out at 0.1g input acceleration for a frequency range of 5 to 60 Hz. It is observed that both in mass configurations 2 and 3, all of the natural frequencies are lowered, and the order at which the natural frequencies of the drag bending and the torsion modes occur are inverted with respect to configuration 1.

Table 3.3 : GVT wing modes for three mass configurations with blocked NES

Mass config.	Lift bending mode (Hz)	Drag bending mode (Hz)	Torsion mode (Hz)
1	11.7	33.4	49.7
2	<5	19.7	16.5
3	6.1	28.1	15.0

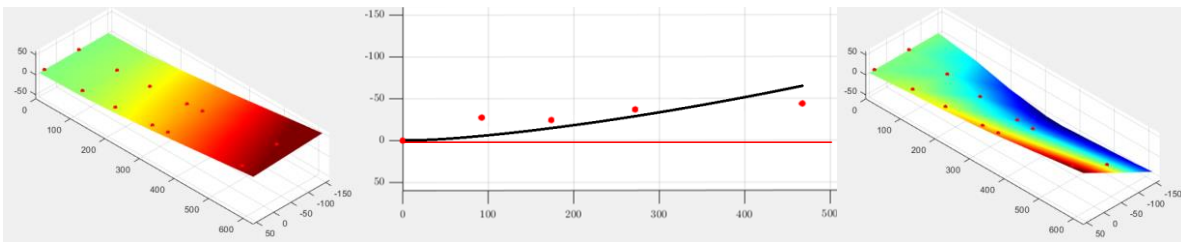


Figure 3.8 : Modal shapes of wing in mass configuration 1 with blocked flap-NES. a) lift bending, b) drag bending c) torsion

3.4.1.2 Effect of the flap-NES

Fig. 3.9 shows the FRF (frequency response function) of the wing tip accelerometer RMS measurements for the three different mass configurations. For each configuration, the blocked flap-NES is used as the baseline for comparing flap-NES A (see table 3.2) and flap-NES B. These tests enable to observe the effect of the flap-NES in the absence of aerodynamic effects.

For mass configuration 1, the bending frequency peak in the system with blocked NES is divided into two smaller amplitude peaks by flap-NES A. This means flap-NES A is correctly tuned for this mass configuration (fig. 3.9a). The first and second resulting new peaks have an amplitude of 29% and 68% respectively of the baseline peak amplitude. Flap-NES B is not as efficient for this system and increases the bending peak frequency by 7%, reducing its amplitude by 12%. Figure 3.9b shows mass configuration 2 (see table 3.1 for mass configurations). In this case, the first frequency peak is lower than 5 Hz, which is the lower limit frequency of the shaker, and is therefore not captured; observations cannot be made regarding this peak. However, it can be seen that there is no significant effect of either flap-NES on the drag resonance (at 16.5 Hz). Finally, in mass configuration 3, in fig. 3.9c, no resonance frequency peak is split but their amplitude is reduced by 16% using flap A and 22% using flap B. Overall, the better dimensioned flap-NES is the flap-NES A for the mass configuration 1 considering only structural effects without wind. In this context, none of the flap-NES amplify the original structure's response on the shaker, at the bending frequency.

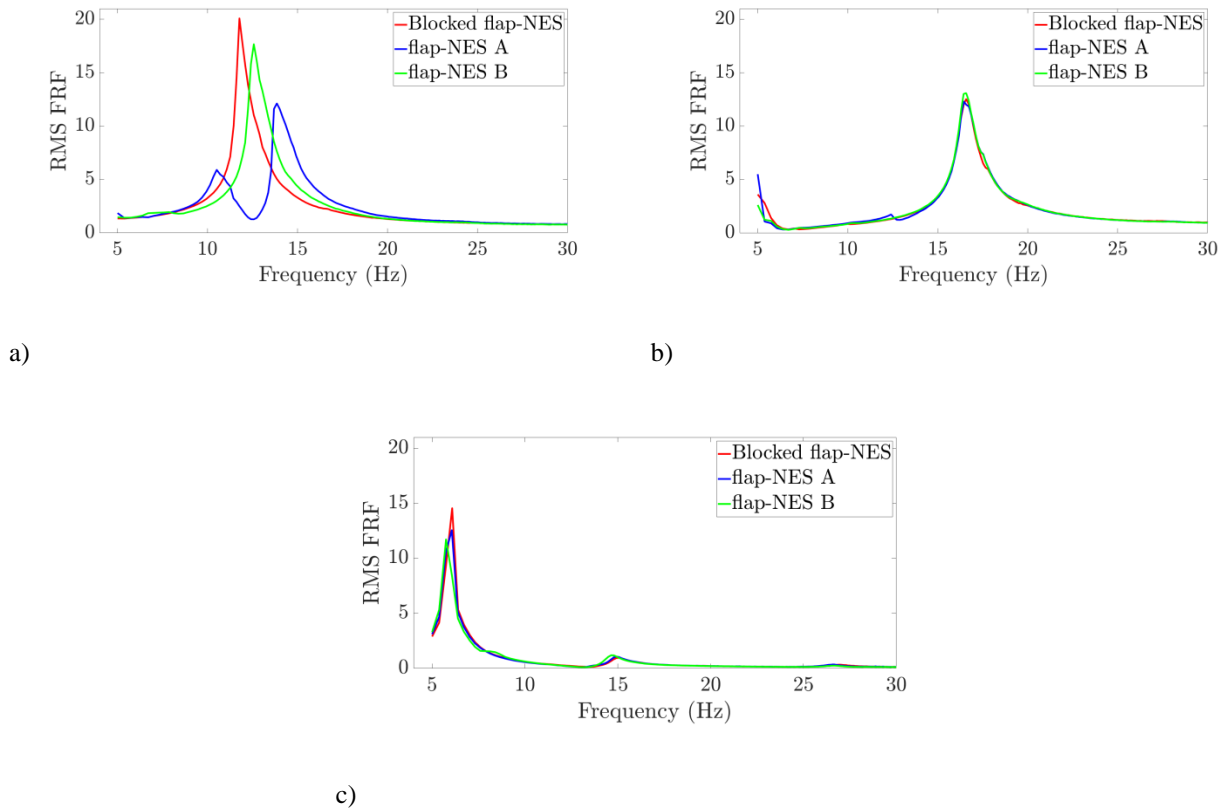


Figure 3.9 : Wing tip FRF in lift direction a) mass config. 1, b) mass config. 2, c) mass config. 3

3.4.2 Wind tunnel tests

The flap-NES effect in the GVT and in the wind tunnel do not necessarily have a corresponding trend. As a matter of fact, adding aerodynamics leads to a different dynamic behavior due to added aerodynamic mass, stiffness and damping.

For the wind speed range of interest, ramps are carried out from 15.2 to 24.8 m/s with 0.2 m/s steps of 20 s each. The speed ramps are performed for each of the different mass and flap-NES configurations, giving a total of 9 ramps which were repeated twice. Throughout the tests, the angle of attack is fixed at 15° in order to have detached flow which gives rise to Vortex Induced Vibration (VIV).

For each mode during a ramp, the vibration amplitude of the wing varies with increasing wind speed, but the frequencies remain mostly constant. The vibration response is caused by

Vortex Induced Vibration (VIV). The purpose of the flap-NES is to control the response by decreasing the wing's total energy and achieving vibration mitigation.

Figure 3.10 and 3.11 shows the response of the system during the wind speed ramps, with different flap-NES for mass configurations 1 and 2 respectively quantified by a scalar that we refer to as the “energy of the wing”. In this way, the global energy of the wing is estimated and compared throughout the configurations. This energy is estimated by adding up the signal energy of all 14 accelerometers on the wing. Both lift and drag accelerations are considered as the wing displays a coupled mode movement. The signal energy is obtained by time integration of the sensor signal squared. In this way, the movement of the wing throughout the wind speed ramp is quantified by considering both the frequency and amplitude of the movement enabling the comparison of the different configurations. This is shown in equation 5 where A_i are each of the 14 accelerometer sensor signals and E is the total signal energy.

$$E = \sum_{i=1}^{14} \int [A_i(t)]^2 dt \quad (5)$$

In mass configuration 1, flap-NES A reduces the total signal energy, for wind speeds below 22 m/s as seen fig. 3.10a where the blue curve is below the red curve up to 22 m/s. This is further represented in fig. 3.10b where the ratio of the energies of flap-NES A over blocked flap-NES is plotted with respect to wind speed. In this figure, the green area represents the zone in which the energy of the system is reduced by the flap-NES A and the red area is where it is increased. This highlights the fact that flap-NES optimization depends on the desired range of wind speeds. In the present configuration, flap-NES A is useful below 22 m/s, where it reduces the energy of the system up to 60%. Over that speed, the energy of the system with the flap-NES A becomes higher than the energy with the blocked flap-NES (up to 130%). On the other hand, in fig. 3.10a, it is seen that flap-NES B is incorrectly tuned for this mass distribution (green curve above red curve) and, therefore, the effect is contrary to the desired outcome. The test had to be stopped before the maximum wind speed as the vibration of the wing became violent.

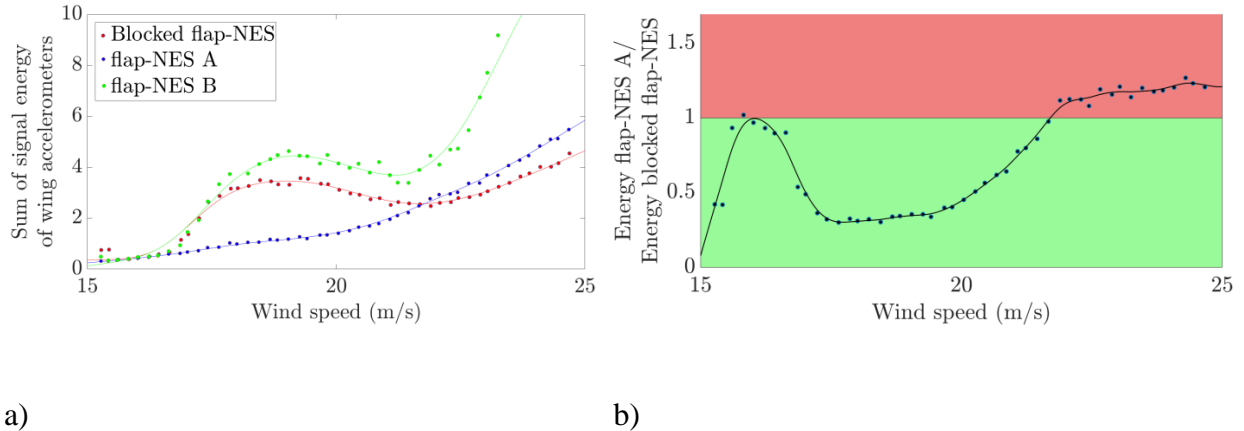


Figure 3.10 : Mass config. 1: a) Evolution of the energy the wing, b) Ratio of flap-NES A to blocked flap-NES of the energy of the wing

Regarding mass configuration 2, shown in fig. 3.11a, the softer springs in flap-NES B turn out to be more appropriate as the system's energy is greatly reduced with respect to the baseline system over the entire range of wind speeds. Although flap-NES B is effective for the whole wind speed range, its efficiency increases from 80% at 15 m/s to more than 90% at 18 m/s, and is relatively constant for higher wind speeds (see fig. 3.11b). This shows, similarly to fig. 3.10b, that the efficiency of the flap-NES varies with wind speed. Flap-NES A is not correctly tuned for this configuration and the energy is increased over the whole range of wind speeds.

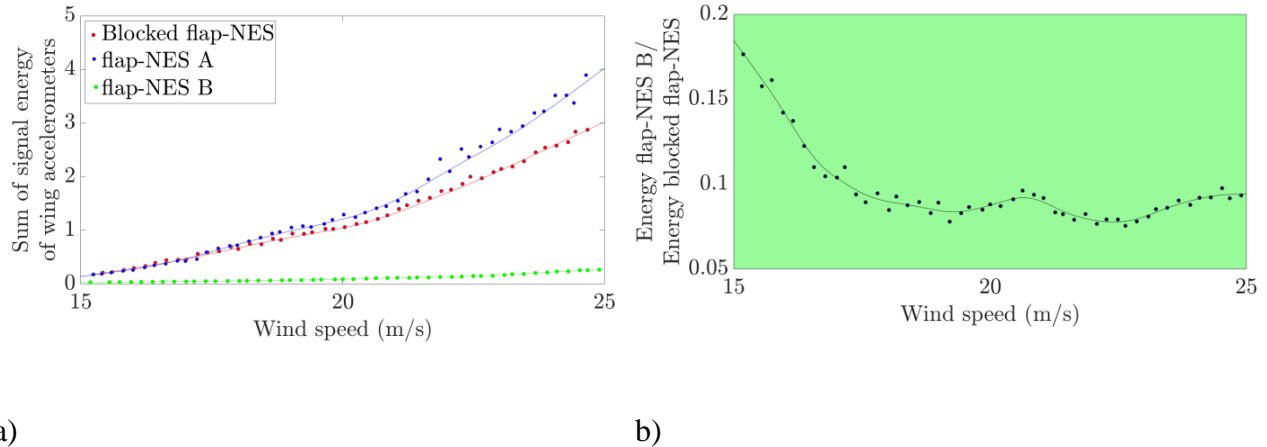


Figure 3.11 : Mass config. 2a) Evolution of the energy of the wing, b) Ratio of flap-NES B to blocked flap-NES of the energy of the wing

Finally, none of the two flap-NES tested is correctly tuned for the mass configuration 3 (not illustrated). However, the system's energy in both cases is just slightly increased and not highly amplified.

3.4.3 Conclusion

In this work, a passive solution for controlling vortex induced vibration of aircraft wings. The solution consists of a nonlinear tuned mass damper called "flap-NES". The flap-NES adds little mass and is placed near the wing tip, to obtain a localized nonlinearity and to maximize its effect on the structure. This device is integrated in a rectangular tridimensional flexible aircraft wing presenting vortex induced vibration. The objective is to show, experimentally, the effectiveness of this solution, as well as to highlight the importance of proper dimensioning for a given wing system.

The importance of correct NES dimensioning is highlighted by testing different masses and flap-NES configurations. The tests yield different outcomes: either the vibrations due to VIV of the system are highly decreased when the adequate flap-NES is activated, or they are increased or remain unchanged if the flap-NES is not correctly tuned. Flap-NES effectiveness is evaluated with respect to a corresponding baseline system in which flap-NES is blocked. Out of the nine mass and flap-NES combinations tested, two combinations show high vibration mitigation when

the flap-NES is present. In one combination, the system's energy is reduced by up to 60% over 88% of the range of the wind speeds tested. In the second configuration, the system's energy is reduced between 80% and 90% throughout the entire range of wind speeds tested.

Overall, this work presents and demonstrates the efficiency of a solution for passive aeroelastic control which can be easily integrated in aircraft wings with negligible added mass. The capacity of the flap-NES of acting as a secondary oscillator and absorbing energy from the main structure in this context is highlighted. The great importance of its correct dimensioning and optimization is also observed and this will be the focus of further analytical and computational development of the flap-NES concept.

Funding Sources

The authors would like to acknowledge the Natural Sciences and Engineering Research Council of Canada and Université de Toulouse for the funding.

Acknowledgments

The work greatly benefited from the expertise of the technical team and in particular of Rémy Chanton, Leonardo Sanches, Jean-Benoit Alibert and Henri Dedieu.

CHAPTER 4 ARTICLE 3: COMPARISON OF LOW, MEDIUM AND HIGH FIDELITY NUMERICAL METHODS FOR UNSTEADY AERODYNAMICS AND NONLINEAR AEROELASTICITY

FERNANDEZ-ESCUDERO, C., GAGNON, M., LAURENDEAU, E., PROTHIN, S., MICHON, G., ROSS, A. *Journal of Fluid and Structures*.

In the previous sections, the efficiency of the flap-NES is showed experimentally. The necessity of a correct flap-NES is also highlighted in chapter 3. Numerical simulations are adequate for this kind of optimization since they enable to change parameters within large ranges easily. Also, since the flap-NES is an innovative concept within the complex field of nonlinear aeroelasticity, having a double numerical and experimental approach is an important asset to understand the physics behind the observed phenomena. In this sense, this chapter is a first step to the future numerical optimization of the flap-NES.

The section presents the third and final journal article written and published in the framework of this PhD thesis. It consists of a comparison of different numerical methods applied to aerodynamics and, more precisely to aeroelasticity through different literature cases. These methods have been developed with the objective of being used in the future flap-NES development and optimization. The test cases used could be the base of future flap-NES optimization.

Following the logic of chapter 2, the aeroelastic system chosen is a profile, equivalent to a bidimensional wing. The test cases chosen in order to compare the different numerical methods are chosen from the existing aeroelastic literature. Some of the test cases contain structural nonlinearities in order to assess the capacity of the numerical methods to simulate the response of these systems. Like in the first experimental bidimensional campaign (chapter 2), the systems studied presents classic flutter and limit cycle oscillations. This section concludes that for the cases presented, the low-fidelity methods are capable of capturing the same complex phenomena than for medium or high fidelity methods, at much reduced computational times. The importance of this section is the development and validation of the numerical methods. This approach is

developed for future flap-NES analysis and optimisation and pertinent considerations, such as using lower fidelity methods for faster preliminary optimisation, are made.

FERNANDEZ-ESCUDERO, C., GAGNON, M., LAURENDEAU, E., PROTHIN, S., MICHON, G., ROSS, A., “Comparison of low, medium and high fidelity numerical methods for unsteady aerodynamics and nonlinear aeroelasticity,” *Journal of Fluid and Structures*, vol 91, 2019, 102744, ISSN 0889-9746, doi:10.1016/j.jfluidstructs.2019.102744.

Abstract The unsteady aerodynamic and aeroelastic behaviour of a 2D wing section with and without flap is analysed with Theodorsen theory and Unsteady Vortex Lattice Method (low fidelity), Euler (medium fidelity) and Reynolds-Averaged Navier Stokes (high fidelity) methods. The aeroelastic studies are carried out for linear cases and non-linear structural configurations presenting cubic stiffness and freeplay. The critical flutter speeds as well as the limit cycle oscillations present in the non-linear cases are compared. The methods show good agreement for the cases studied.

4.1 Introduction

Aeroelasticity remains today a subject of great interest in aircraft design and analysis. It includes the study of static aeroelastic effects and the analysis of more complex problems which appear when dynamic systems are considered. Moreover, aeroelasticity is often affected by non-linearities which alter the system's response; it is the subject of active research, as can be found in the review paper by [95]. These non-linearities have two different sources: structural elements such as freeplay or cubic stiffness [96] can appear alone or simultaneously in any of the degrees of freedom (DOF) of the airfoil [16] and aerodynamic effects which are mainly due to either transonic effects [97] or to dynamic flow separation due to large deflections in wings, known as stall flutter [16]. The present paper focuses on the two structural non-linearities mentioned, i.e. freeplay and cubic stiffness.

An important phenomenon encountered in dynamic aeroelasticity is flutter. If there are no sources of non-linearities the system can only experience classic flutter which is defined as self-excited vibration of the structure due to energy extraction of the incident airflow resulting in negative damping and, therefore, a divergent evolution of the amplitude of vibration. One of the causes of this phenomenon is the coalescence of two structural modes: pitch and plunge, which

reach the same vibration frequency. Other causes of flutter include transonic effects which cause “dip-flutter”, flow separation leading to stall flutter or instabilities in the flow above or below the structure which may result, for example, in buffet or galloping. If the speed becomes higher than the flutter speed, the amplitude of the movement grows exponentially causing structural failure [66]. A thorough analysis of these aeroelastic problems is presented in [98] and in [99] which also developed many of the flutter prediction computational methods currently used in the current aeronautics industry.

The presence of non-linearities can change drastically the observed behaviour as other phenomena, such as limit cycle oscillations (LCOs), can appear in the system’s response. During a LCO, the vibration reaches a stable amplitude which remains constant unless the wind speed changes. LCOs can be observed in subcritical or in supercritical regime once flutter speed is passed (Thomas, 2002). It has been found that when non-linearities govern the system behaviour, initial conditions may cause the system response to change between two or more possible stable outcomes [8]. These non-linearities can mainly have two different sources: structural or aerodynamic. Structural non-linearity can be caused by many different elements. Moving parts can have friction or gaps [100] between them or a nonlinear stiffness, such as a cubic stiffness, [45] [96] [101], as will be shown further to be our case. Irregular surfaces with, for example, rivets, are also a common source of nonlinearity. These elements are often classified as concentrated (the freeplay) or distributed (the rivets) nonlinearities. The focus of this work will be in concentrated structural non-linearities. As for aerodynamic non-linearities, they are mainly due to either transonic effects [98] or to flow separation due to viscous effects, for instance, large deflections in wings, or perturbing elements on the aircraft [7].

The aim of this work is to compare the ability of different numerical methods to capture unstable aerodynamics and aeroelastic behaviour. The aerodynamic forces acting on the airfoil are computed and, together with the equations of motion, enable the calculation of the fluid-structure effects. For the aeroelastic analysis, both the linear and the non-linear cases are studied. In the non-linear 2DOF case, cubic stiffness and freeplay gap are applied in the pitch restoring force whereas only freeplay in the control surface deflection is applied in the 3DOF case. This work follows the work of [41] and includes the use of NLFD (Non-Linear Frequency Domain)

for the high fidelity solvers as well as with more accurate time-integration and post-processing techniques.

4.2 Structural Model

Two configurations are studied regarding the 2D typical wing section: a 2DOF and a 3DOF airfoil. The 2DOF are heave h and pitch α and the 3DOF case refers to an airfoil with an added control surface that can rotate around its elastic axis β . The airfoil is a NACA0012. Figure 4.1 presents the degrees of freedom for each case and the main geometrical parameters: b is the semi chord length, ab and cb are the midchord to elastic axis of the profile and of the control surface distance, respectively. Similarly, $x_\alpha b$ and $x_\beta b$ are the centre of gravity to elastic axis distance of the airfoil and of the control surface, respectively.

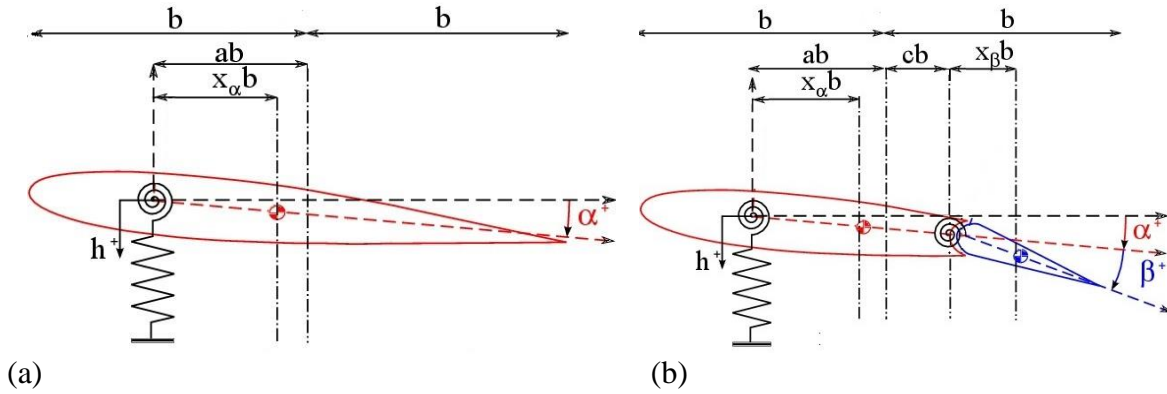


Figure 4.1 : a) 2DOF and b) 3DOF typical aeroelastic sections. [41]

The dimensionless aeroelastic equation of motion of an airfoil is:

$$M_s \ddot{q} + B_s \dot{q} + (1 - \nu) K_s q + \nu f_s(q) = f_a(t) \quad (4.1a)$$

$$M_s = \begin{bmatrix} 1 + \mu_h & x_\alpha & x_\beta \\ x_\alpha & r_\alpha^2 & r_\beta^2 + (c - a)x_\beta \\ x_\beta & r_\beta^2 + (c - a)x_\beta & r_\beta^2 \end{bmatrix} \quad (4.1b)$$

$$K_s = \begin{bmatrix} \omega_h^2 & 0 & 0 \\ 0 & r_\alpha^2 & 0 \\ 0 & 0 & r_\beta^2 \end{bmatrix} \quad (4.1c)$$

$$q = [h/b \quad \alpha \quad \beta] \quad (4.1d)$$

$$f_a = [-L \quad M_\alpha \quad M_\beta] \quad (4.1e)$$

where M_s , B_s and K_s represent respectively the inertial, damping and stiffness matrices, q is a vector containing the degrees of freedom and f_s and f_a are vectors containing respectively the restoring and aerodynamic forces. ν is a switch parameter which has a value of either 1 when the system is non-linear and 0 when the system is linear.

As for the structural damping, matrix B_s is calculated by the method described in [102] where firstly the eigenvalues of the homogeneous linear system are obtained which enable the calculation of the natural frequencies and the modal mass matrix. Next, the modal mass matrix is obtained and the modal damping matrix is calculated making use of the damping ratios (ζ) obtained experimentally.

In order to solve the fluid structure interaction, a loosely coupled iterative scheme is selected (see fig. 4.2), whereby the fluid state (W) and structure state (X) are successively updated from iteration n to $n + 1$. First, the fluid forces F_a are computed at a given time step and interpolated back onto the structure. The structure state is then computed and the new position, velocity and acceleration (q , \dot{q} and \ddot{q} respectively) are thereafter calculated. The process is then repeated for the next iterative time-step.

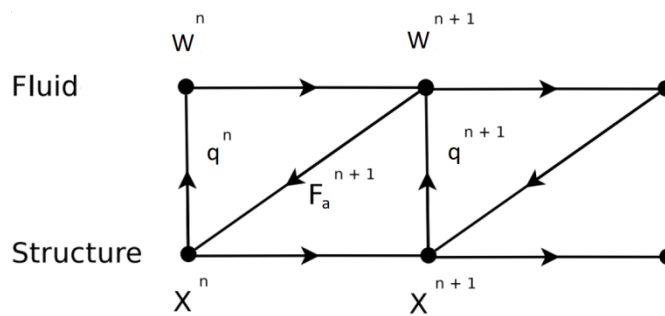


Figure 4.2 : Schema for loosely coupled Fluid-Structure interaction [40]

Non-linearities are introduced in the pitch restoring force in the form of a cubic stiffness and a freeplay gap in the 2DOF [100] (see fig. 4.3). In the 3DOF case, freeplay is introduced in control surface deflection [45]. The equations are as follows:

$$f_{s,\alpha} = \begin{cases} r_\alpha^2 \sum_{k=1}^n \eta_{\alpha,k} (\alpha - \alpha_s)^k, & \text{if } \alpha > \alpha_s \\ r_\alpha^2 \sum_{k=1}^n \eta_{\alpha,k} (\alpha + \alpha_s)^k, & \text{if } \alpha < -\alpha_s \\ 0, & \text{else} \end{cases} \quad (4.2)$$

$$f_{s,\beta} = \begin{cases} r_\beta^2 \sum_{k=1}^n \eta_{\beta,k} (\beta - \beta_s)^k, & \text{if } \beta > \beta_s \\ r_\beta^2 \sum_{k=1}^n \eta_{\beta,k} (\beta + \beta_s)^k, & \text{if } \beta < -\beta_s \\ 0, & \text{else} \end{cases} \quad (4.3)$$

where α_s and β_s are half of the freeplay angle in pitch and in control surface deflection, r_α and r_β are the reduced radius of gyration defined as $r_{\alpha/\beta} = \sqrt{\frac{I_{\alpha/\beta}}{mb^2}}$ where m is the mass of the airfoil, $I_{\alpha/\beta}$ are the structural inertias, $\eta_{\alpha,k}$ is the ratio between the k^{th} non-linear quadratic stiffness and the linear stiffness and $\Omega_{\beta,k}$ is the reduced uncoupled natural frequency at the k^{th} order.

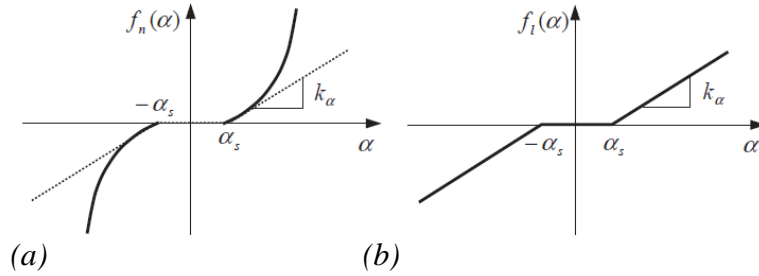


Figure 4.3 : Non-linear pitch stiffness: (a) cubic stiffness with freeplay; (b) freeplay. [100]

4.3 Aerodynamic Models

Different numerical approaches are used to model the aerodynamic forces vector, f_a . These are described at very high level to highlight their respective modelling and computational time differences.

4.3.1 Theodorsen approach

The Theodorsen approach assumes harmonic motion and is valid for thin profiles with small deflections immersed in linear incompressible and irrotational flows. Its ability to capture LCOs

in non-linear cases was demonstrated in [45]. Contrary to the quasi-stationary force approach, Theodorsen takes into account the effects of the wake on the profile by imposing the impermeability and the Kutta conditions. The vortices shed are assumed to be aligned with the profile resulting in a flat wake. The original formulation is in frequency domain [42] and remains convenient as long as the system is linear. However, for non-linear cases the equations are more easily solved in time domain and the Jones approximation is used [46].

In the case of the frequency domain approach the Theodorsen complex transfer function $C(k)$ is used whereas in time domain, the inverse Fourier transform of this function is used which is called Wagner function [47]. The later function enables the calculation of an augmented variable which is used to obtain the aerodynamic coefficients as shown in [103].

4.3.2 UVLM

In the Unsteady Vortex Lattice Method (UVLM), the airfoil and the aileron are discretized into panels and the transport of vortices is accounted for by a shedding wake [54] in the case of the free wake approach. Other options are available for the wake model: a rigid wake which captures the oscillating motion of the wake but, unlike the free wake approach, does not account for the wake roll-up or a linear wake which assumes a flat wake similar to the Theodorsen method (fig. 4.4). Since the results obtained by all three methods, namely free wake, rigid wake and flat wake, were similar for the cases examined in our study, only results with the free wake approach are presented.

Each panel contains a vortex at $\frac{1}{4}$ of its length and a collocation point at $\frac{3}{4}$ of the length (fig. 4.3). The vortex points induce a velocity on the rest of the panels and their influence is calculated in the collocation points. The Kutta condition is satisfied by imposing the same vorticity on the shed wake and on the trailing edge panel. The Neumann boundary condition on the airfoil, for the velocity potential, closes the system [54]. Some limitations remain, as the thin airfoil and potential flow hypothesis still apply.

The computational implementation of the UVLM code is fully described in [54]. The algorithm obtains the vorticity at each point (γ) by solving a linear system of equations:

$$AIC * \gamma = RHS \quad (4.4)$$

where AIC is the Aerodynamic Influence Coefficients matrix which contains the induced velocities ($v_{j,i}$) calculated as:

$$v_{j,i} = \frac{\gamma_j}{2\pi r_{ij}^2} \{y_i - y_j\} \quad (4.5)$$

and RHS is a vector containing the reduced inflow velocity, the reduced airfoil velocity and the position of the airfoil.

Once the vorticities are obtained, the pressure coefficient is calculated using the unsteady Bernoulli equation:

$$C_{p,i} = \frac{\gamma_{i,k}}{\Delta l} * (u_\infty - v_{m,i} + \sum_{l=1}^k v_{l,i}) * n_i + \frac{1}{\Delta t} \sum_{m=1}^i \gamma_{i,k} - \gamma_{i,k-1} \quad (4.6)$$

which enables the calculation of the rest of the aerodynamic coefficients.

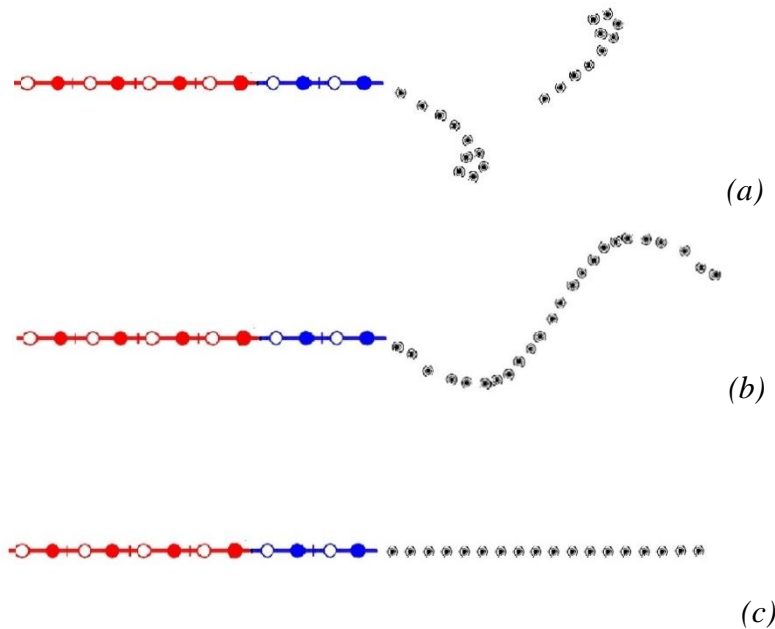


Figure 4.4 : UVLM airfoil discretization. (a) free wake (b) rigid wake (c) flat wake

○:airfoil vortex point, ●:airfoil collocation point, ○:aileron vortex point, ●: aileron collocation point, ⊙:wake vortex

Euler and Unsteady Reynolds-Averaged Navier Stokes (URANS) solvers compute the aerodynamic forces by solving a set of conservation laws (mass, momentum, energy) at discrete space/time intervals. While the Euler equations are non-linear, they ignore viscous effects. URANS solvers are as Euler solvers, with the addition of the viscous stresses. Turbulence is typically modelled via the eddy viscosity assumption. The aerodynamic solver used is NSCODE [104], which uses a cell-centered multiblock structured approach. In this work, we use an implicit LUSGS (Lower-Upper Symmetric Gauss-Seidel) time integration scheme with classical acceleration methods such as multigrid and implicit residual smoothing. For turbulent calculations, the Spalart-Allmaras turbulence model [105] is selected. Different meshes and different time steps were tested to ensure mesh and time converged solutions. Three levels of O-meshes with 129×129 , 257×257 and 513×513 cells were used. The results of the intermediate mesh (257×257) are considered sufficiently converged and are used in the paper. The presented computations use an ALE (Arbitrary Lagrangian Eulerian) formulation. The unsteady Euler model was solved with both DTS (Dual-Time Stepping) [106, 107] and NLFD (Non-Linear Frequency Domain) methods [61]. For DTS, simulations lasted for 7 complete periods with 500 time steps per period. A convergence analysis was performed with 1000 time steps per period, showing time-step convergence. Regarding NLFD, spectral convergence analysis was carried out with 3, 5 and 6 modes and the results shown correspond to the 3 modes analysis.

4.3.3 Computation time

Table 4.1 presents approximate computation time for each of the methods for approximately 10 oscillation cycles (3 initial transient cycles) on a single-core of the Intel 3930K CPU. Note that regarding our cases, the aerodynamic force calculation determines the total computation time since the time taken for the structural equation is comparatively negligible.

Table 4.1 : Approximate computation time for each method

Method	Computation Time on Intel 3930K CPU
Theodorsen	~30 seconds
UVLM	~45 minutes
Euler DTS	~8 hours
Euler NLFD (3 modes)	~6 hours
URANS NLFD (3 modes)	~1 day

4.4 Unsteady Aerodynamics

As a preliminary step, the potential aerodynamic models are verified for imposed plunge and pitch motions of the 2DOF linear airfoil (figs. 4.4 and 4.5). The cases chosen are those presented in Murua [108] using UVLM and (Yang, 2006) using Euler respectively. We emphasise that only the aerodynamic forces are considered in this section and not the structure response to these forces.

For each case, the Mach (M) and Reynolds (Re) numbers are given. We observe that the tests are in low subsonic regime where the incompressibility hypothesis is reasonable. The imposed vibration frequency is characterised by the dimensionless reduced frequency $K = \frac{\omega c}{2U_\infty}$ where ω is the oscillating frequency (in rad/s), c is the airfoil chord and U_∞ is the incident flow speed. The dimensionless amplitude of the movement is given by h/b in the plunge case. In the pitch case, the airfoil moves around a position referred to as “mean alpha” with amplitude alpha. The low-fidelity methods agree in capturing the aerodynamic coefficient Cl at moderate reduced frequency and small oscillations (figs. 4.5 and 4.6). Table 4.2 shows the aerodynamic coefficients obtained at 4.93° angle of attack by the different methods for the steady flow condition ($K=0$).

One must be careful interpreting the differences. Indeed, airfoil thickness increases lift-curve slopes whereas viscous forces reduce it which explains the differences between Theodorsen and RANS solutions. The Euler solution has more lift than the RANS, and the UVLM lift matches Theodorsen's, as expected.

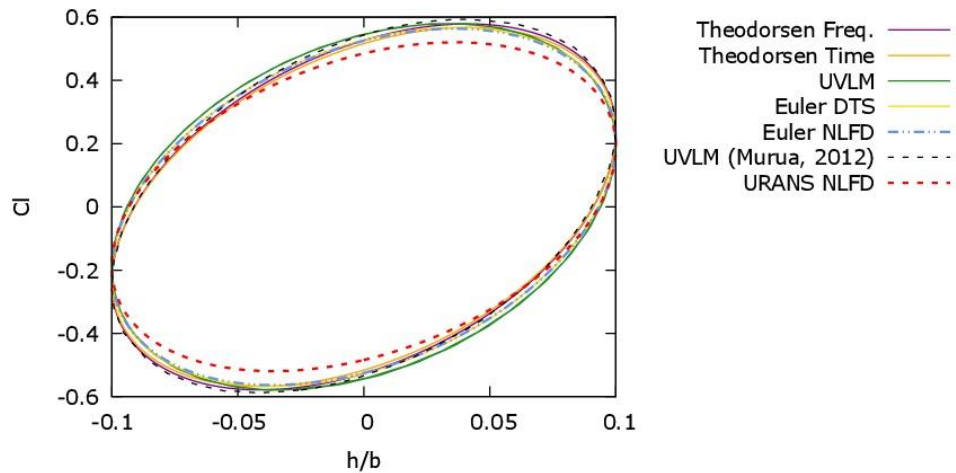


Figure 4.5 : Plunge motion. $M=0.1$, $Re= 1.18M$, $K=0.75$, $h/b=0.1$

Table 4.2 : Steady aerodynamic coefficient. $M =0.301$, $Re=3.91M$, $K=0$, Mean $\alpha=4.93^\circ$

	Theodorsen	UVLM	Euler	URANS
Cl	0.54	0.54	0.63	0.57

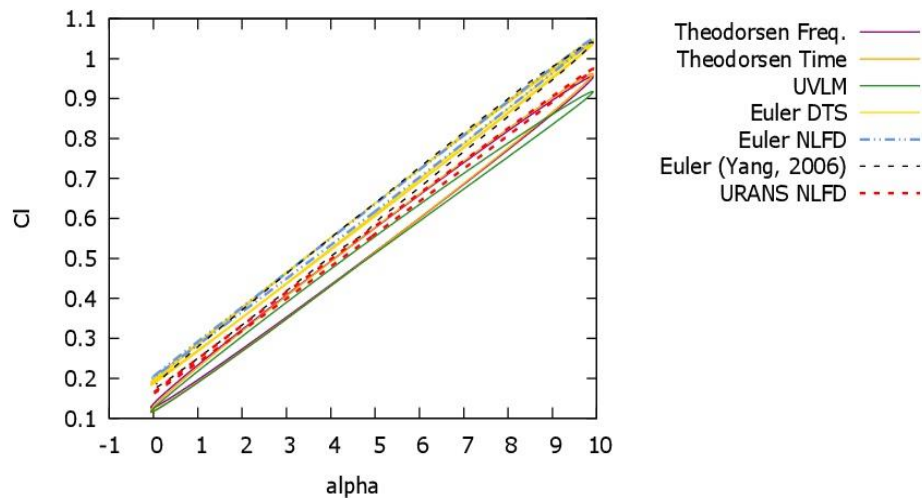


Figure 4.6 : Pitch motion. $M=0.301$, $Re=3.91M$, $K=0.198$, $\alpha=4.99^\circ$, Mean $\alpha=4.93$

4.5 Linear Aeroelasticity

The flutter analysis is performed on the dimensionless aeroelastic equation of motion of the airfoil (*equation 1*) using the aerodynamic force calculated with the numerical methods already presented. The cases tested are those presented in [100] using a reduced order flat wake UVLM model and in Conner [45] experimentally and numerically for the 2DOF and 3DOF cases respectively. The parameters used are presented in table 4.3. The structural parameters already shown are present, as well as $k = \frac{\rho\pi b^2}{m}$ which is the mass ratio, ζ_h , ζ_α and ζ_β , are the structural damping ratios for each DOF and μ_h is the normalized mass of the support. The natural frequencies of each DOF are represented by ω_h , ω_α and ω_β . $\eta_{\alpha,k}$ is the cubic stiffness and freeplay parameters will be used further on for the nonlinear cases.

Due to the fact that UVLM is in time domain, an extra step is required in order to obtain the results presented. A Fast-Fourier Transform is used to obtain frequency content of the time domain solutions. FFT does not allow the damping to be calculated so a combination of curve fitting and logarithmic decrement techniques are used to capture the damping shown in figs. 4.8 and 4.10. In these graphs, although there could be as many damping branches as DOFs, only the branch which becomes negative at the flutter point is included for clarity.

Table 4.3 : Values of parameters for test cases

	2DOF	3DOF
k	1/100	0.03984
a	-0.5	-0.5
c	n/a	0.5
x_α	0.25	0.434
x_β	n/a	0.01996
r_α	0.5	0.7321
r_β	n/a	0.11397
ω_h/ω_α	0.2	0.8078
$\omega_\beta/\omega_\alpha$	n/a	2.0746
ζ_α	0	0.01626
ζ_h	0	0.0115
ζ_β	n/a	0.0113
<i>freeplay</i>	0.5° (α)	2.12° (β)
$\eta_{\alpha,k}$	3	0
μ_h	0	1.163627

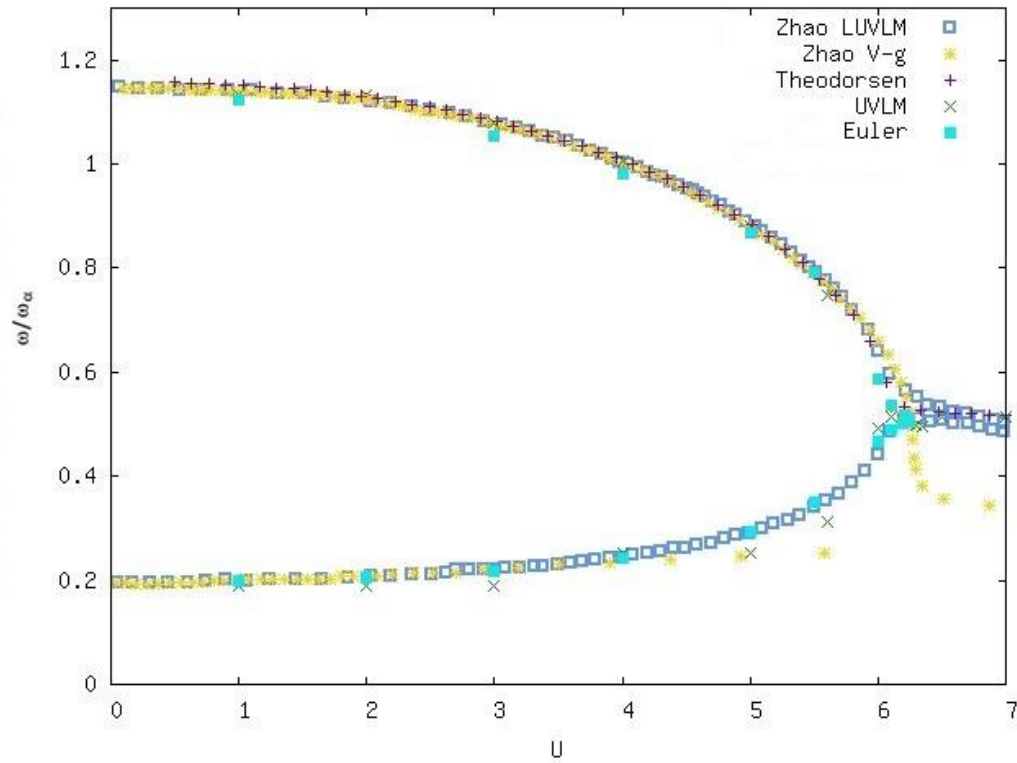


Figure 4.7 : Dimensionless oscillation frequency against dimensionless wind speed for 2DOF linear case

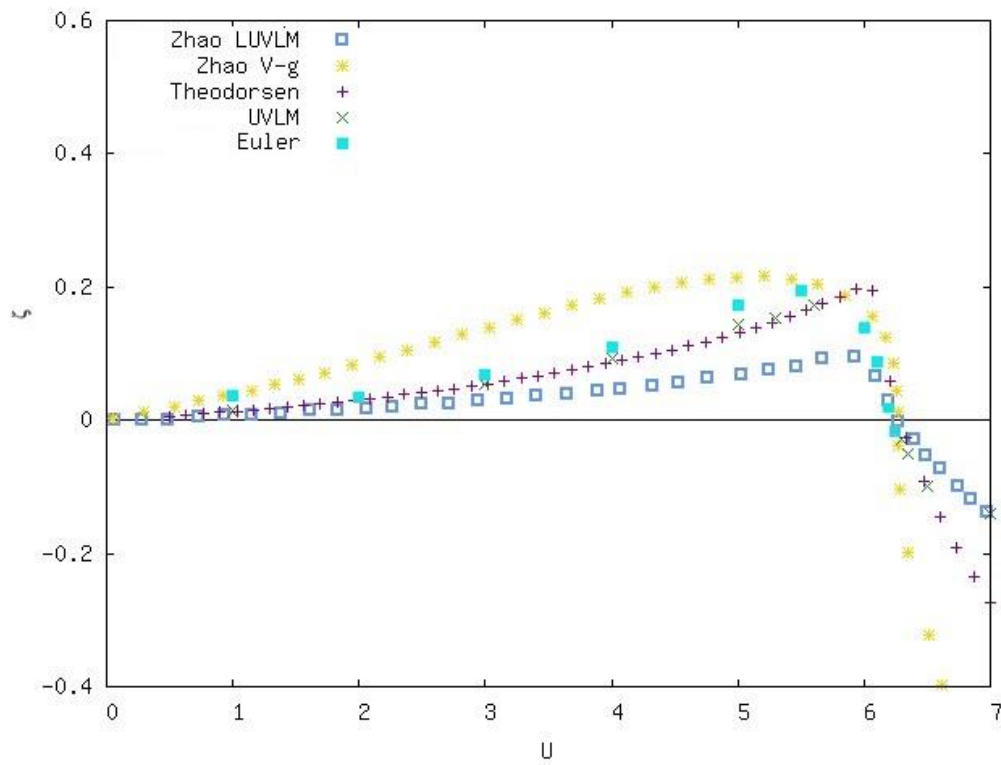


Figure 4.8 : Damping against dimensionless wind speed for the 2DOF linear case

Table 4.4 : Comparison of dimensionless flutter velocities for the 2DOF linear case

	Theodorsen	UVLM	Euler	Zhao V-g	Zhao LUVLM
U_f	6.29	6.27	6.29	6.29	6.29

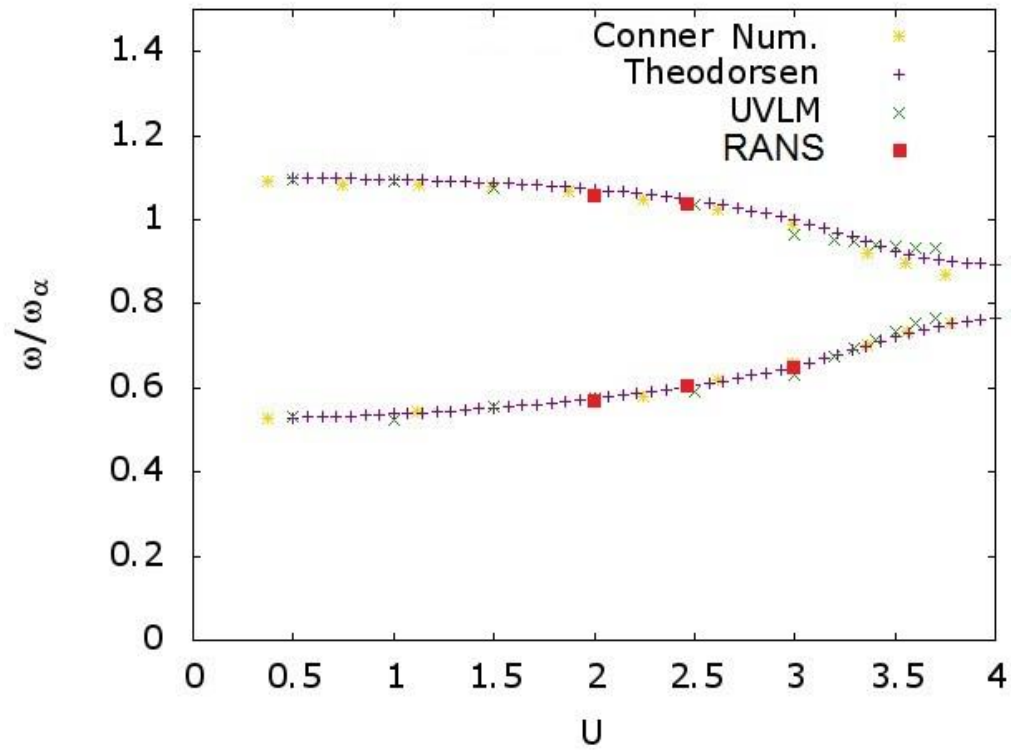


Figure 4.9 : Dimensionless oscillation frequency against dimensionless wind speed for 3DOF linear case

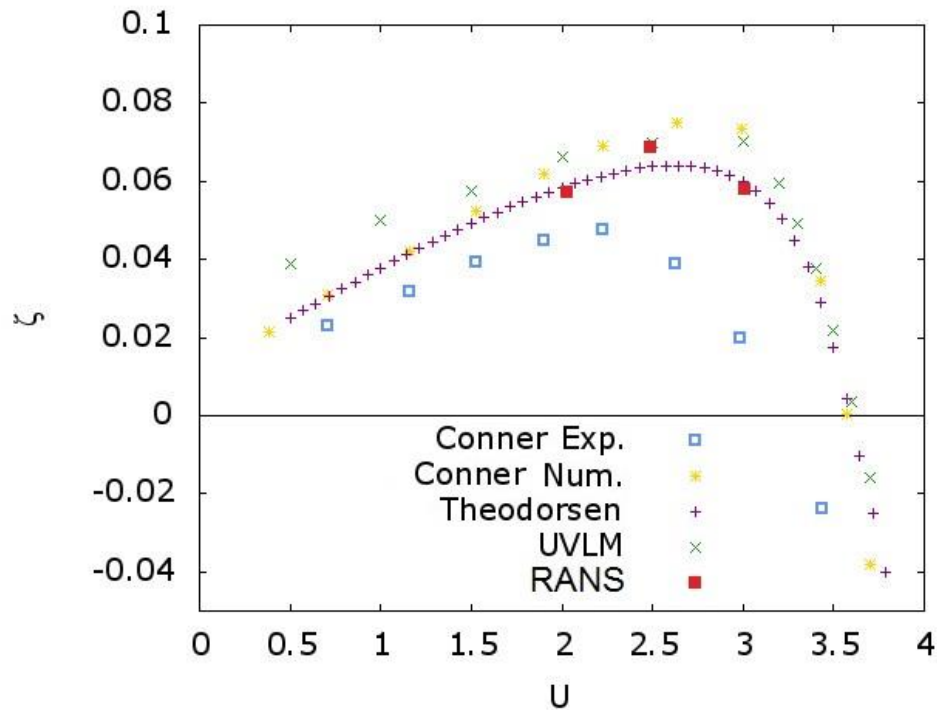


Figure 4.10 : Damping against dimensionless wind speed for the 3DOF linear case

Table 4.5 : Comparison of linear flutter velocities for the 3DOF linear case

	Theodorsen	UVLM	Conner Theo.	Conner Exp.
Uf	3.57	3.61	3.57	3.08

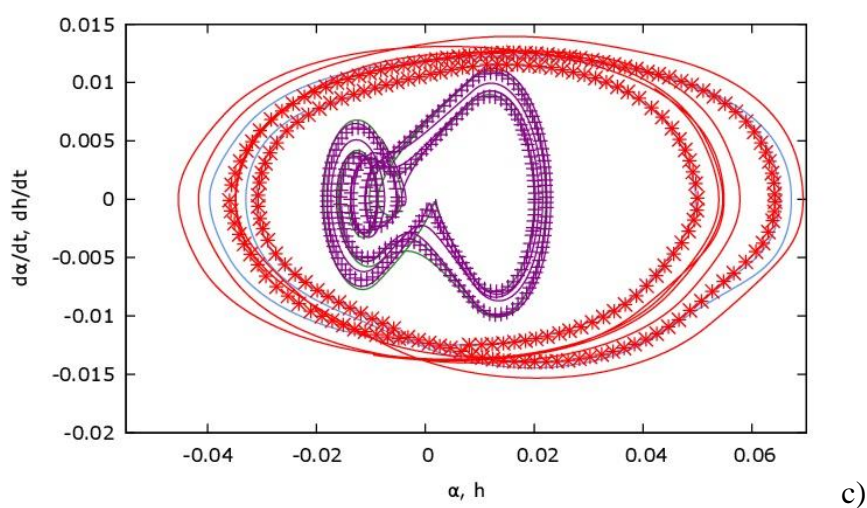
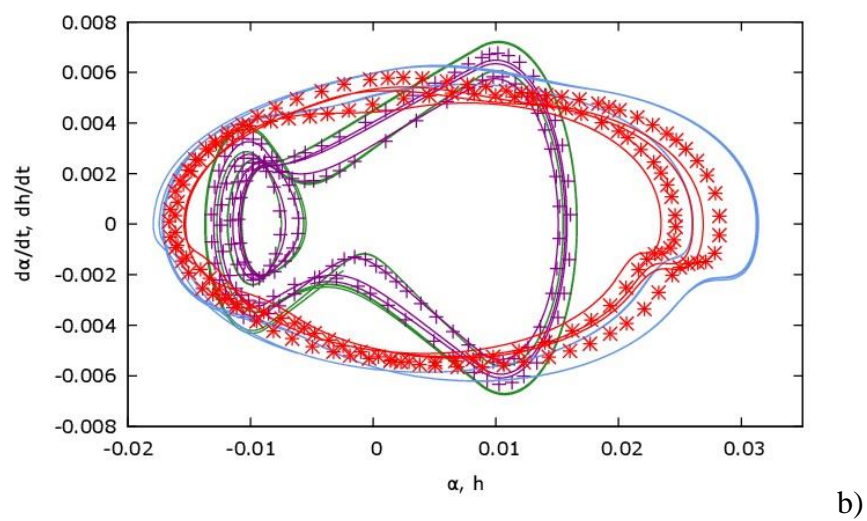
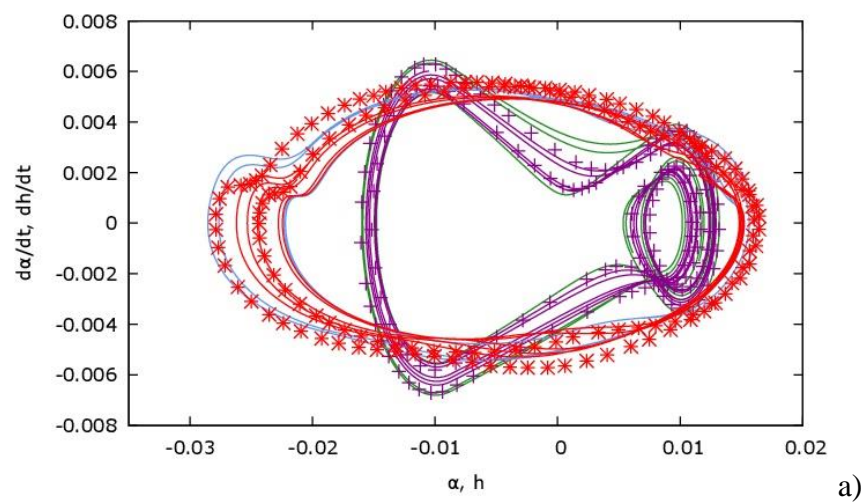
Figures 4.7 to 4.10 show good agreement between Theodorsen, UVLM and Euler or RANS in capturing linear aeroelastic behaviour. These results are compared with [100] for 2DOF and [45] for 3DOF. The values of the flutter speed are obtained, observed as the wind speed at which the damping ratio changes sign in the damping diagrams, and provided in table 4.4 for 2DOF and in table 4.5 for 3DOF cases. In these cases, a modal coalescence in the frequency diagrams can be observed at a close wind speed. Figures 4.8 and 4.10 show reasonably good agreement for the methods presented for all wind speeds but it is seen that the approaches become closer to each other as the system is in the close vicinity to flutter as the system goes from being damped to undamped. This important change of behaviour is thought to be more simply captured than the exact values of positive damping which are not obtained as directly as the modal frequencies for

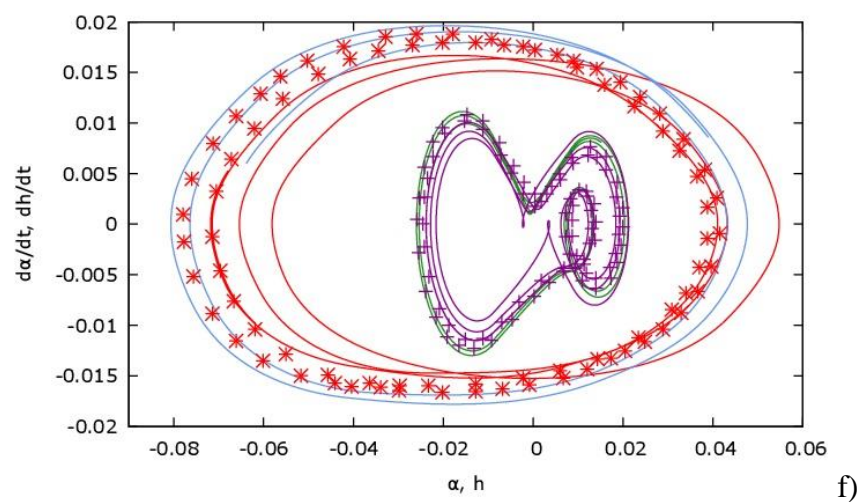
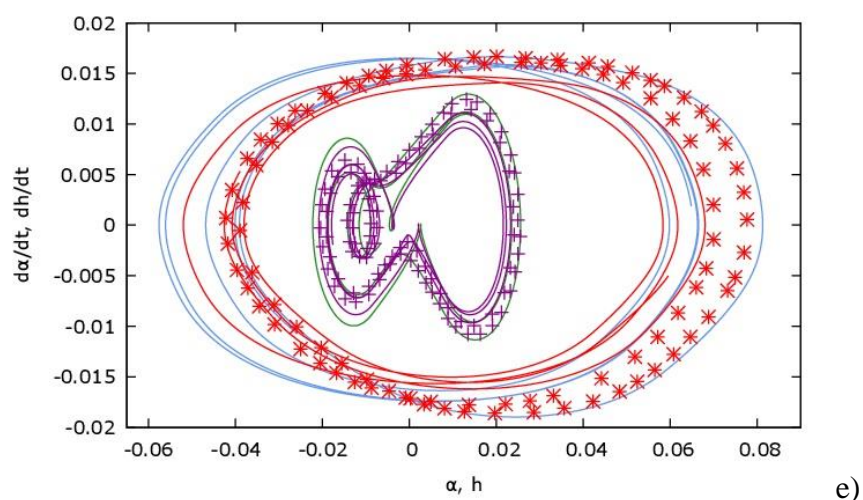
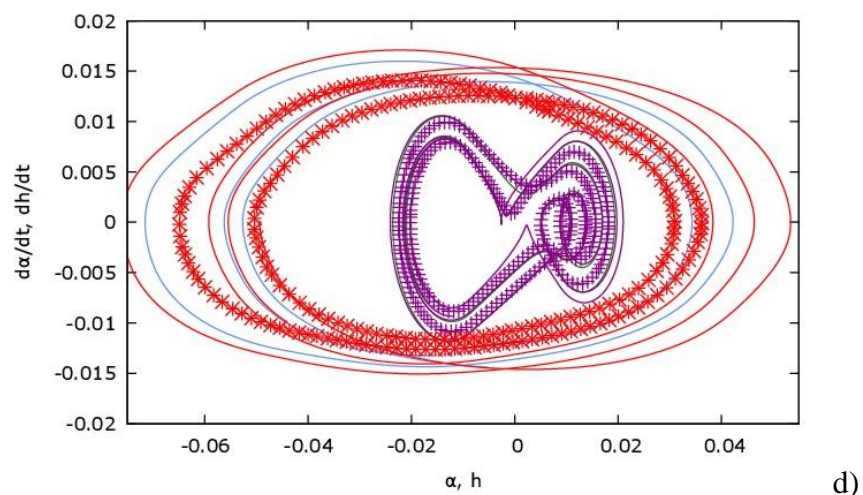
time domain methods and have to be extracted by different means which may give rise to a certain level of uncertainty.

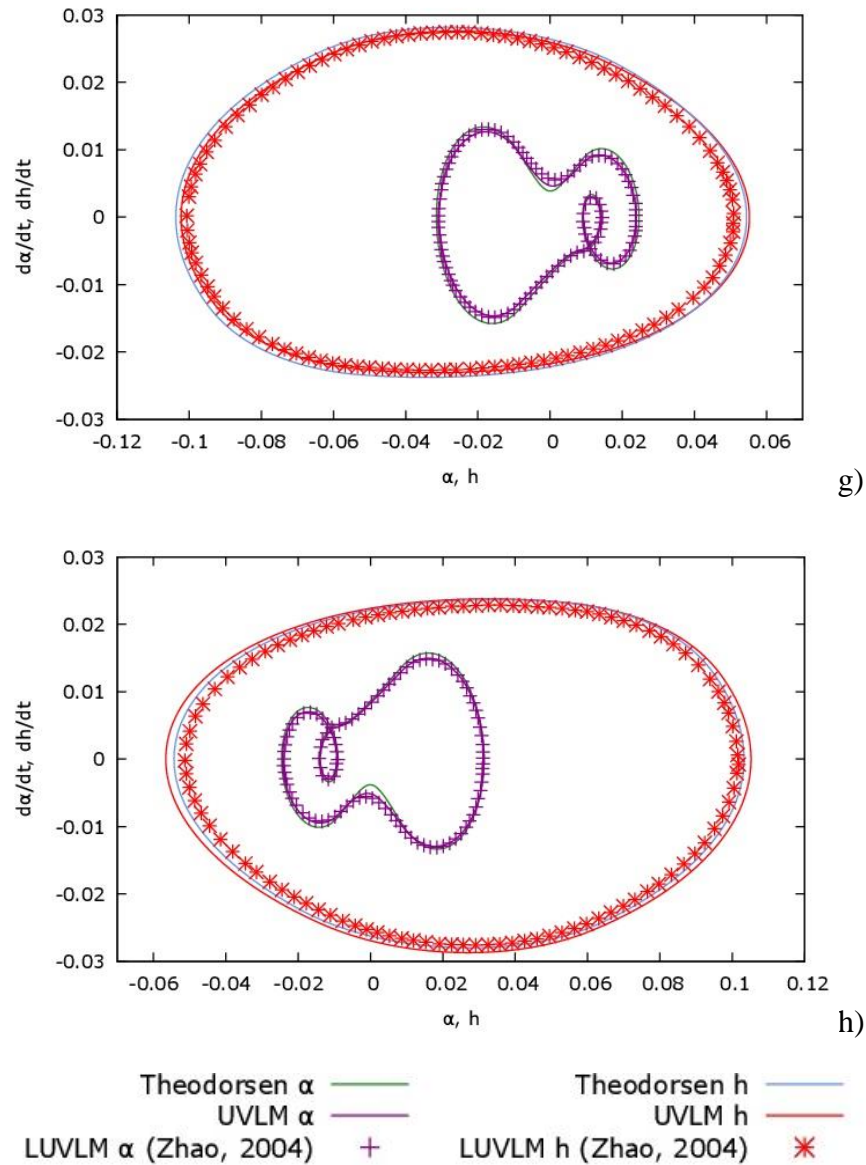
4.6 Non-Linear Aeroelasticity

For non-linear analysis, the same parameters shown in table 4.3 are used but now include the following parameters: *freeplay*, $\eta_{\alpha,k}$ (*the non-linear stiffness power*) and μ_h . Regarding the nonlinear restoring forces, cubic and freeplay non-linearities are introduced in the pitch DOF for the 2DOF case (fig. 4.11), and freeplay is introduced in the aileron deflection for the 3DOF case (fig. 4.12). The rest of restoring forces in the structural models are kept linear. As for the initial conditions, the 2DOF case (fig. 4.11) is started with an initial α of 3° and the 3DOF case (fig. 4.12) is started with an initial β of $2,12^\circ$ similar to the literature cases chosen as due to the nonlinear characteristics of the system, LCO amplitude is dependent on initial conditions.

Below the linear flutter speed, U_f , both Theodorsen and UVLM succeeded in capturing the subcritical LCO and were compared with [100], who used a reduced order linear wake UVLM model named LUVLM, in the 2DOF case. Figure 4.11 presents $d\alpha/dt$ and dh/dt against α and h respectively for different dimensionless speeds.







- a) U : Theo. : 1.850, UVLM : 1.800, Zhao LUVLM : 1.900
b) U : Theo. : 2.007, UVLM : 1.860, Zhao LUVLM : 1.912
c) U : Theo. : 2.925, UVLM : 2.990, Zhao LUVLM : 2.931
d) U : Theo. : 3.140, UVLM : 3.120, Zhao LUVLM : 2.944
e) U : Theo. : 3.420, UVLM : 3.140, Zhao LUVLM : 3.453
f) U : Theo. : 3.520, UVLM : 3.150, Zhao LUVLM : 3.466
g) U : Theo. : 4.160, UVLM : 4.000, Zhao LUVLM : 4.076
h) U : Theo. : 4.150, UVLM : 4.010, Zhao LUVLM : 4.089

Figure 4.11 : Change of phase trajectory of subcritical LCO for 2DOF airfoil.

Both the Theodorsen and the UVLM codes have captured a subcritical LCO with four different double symmetric changes of trajectory (fig. 4.11), in agreement with Zhao's work. The authors believe that some of the observed deviations between the presented intermediate figures may be linked to the difficulty experienced in identifying the matching wind speed corresponding to an exact given LCO amplitude due to the fact that the LCO trajectories have a high level of variation as the wind speed increases. It is observed that the α trajectory is closer in all methods than the h trajectory.

For the 3DOF analysis, the literature cases chosen are those presented by [45], who also presented experimental data, and [101], who used a Doublet Lattice Method (DLM) as well as Theodorsen approach, respectively.

For the 3 DOF non-linear case, the root mean square (RMS) of each DOF's amplitude is calculated and divided by the freeplay gap to compare the results to those obtained by Kholodar [101]. Figure 4.12 shows the results as a function of speed divided by the linear flutter speed

where: $(h, \alpha, \beta) = \frac{RMS(h, \alpha, \beta)}{2\beta_s}$.

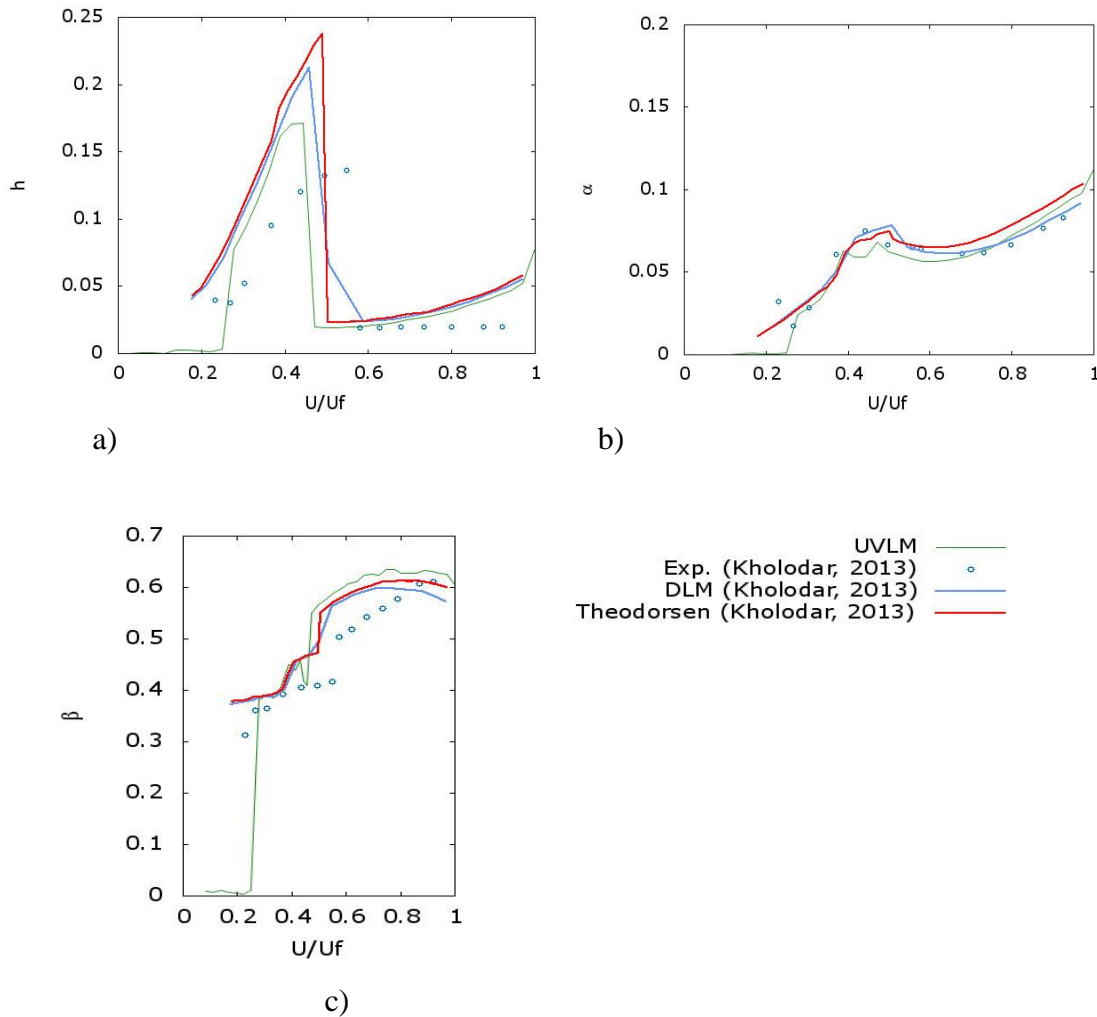


Figure 4.12 : RMS amplitudes as a function of speed over linear flutter speed a) plunge DOF, b) pitch DOF and c) control surface deflection.

The subcritical LCOs present in the 3DOF system including freeplay are captured as observed in fig. 4.12. For each DOF, motion amplitude varies as linear flutter speed fraction increases. Pitch angle and aileron deflection angle both increase with flow velocity with different rates, as shown by all models. The heaving amplitude increases and then drops to lower amplitude LCO before increasing again as the velocity approaches linear flutter speed.

4.7 Conclusion

In this work, four methods are used to analyse unsteady aerodynamics and aeroelasticity of a 2D typical wing section: Theodorsen, UVLM, Euler and URANS. The structural models are presented, followed by a brief description of the aerodynamic methods that highlights their differences. Once a mesh/time step validation is carried out to ensure numerical convergence, a pure aerodynamic comparison is performed, showing the agreement between the unsteady aerodynamics low fidelity results and those obtained via Euler (medium fidelity) and URANS (high fidelity) approaches.

Regarding the aeroelastic analysis, the linear flutter speed is identified for a 2DOF and a 3DOF typical section. Non-linearities through freeplay and cubic stiffness in the pitching DOF for the 2DOF case and aileron freeplay for the 3DOF are added to the system to evaluate its response. Both Theodorsen and UVLM are able to capture subcritical LCOs similar to those identified in the literature.

The computational times of Theodorsen and UVLM are lower by several orders of magnitude than those of URANS or even Euler method. It is concluded that for the cases presented, the low-fidelity methods are capable of capturing the same complex phenomena than for medium or high fidelity methods, at much reduced computational times.

Acknowledgements

The authors would like to acknowledge the Natural Sciences and Engineering Research Council of Canada and ISAE-Supaero for the funding. The work benefited from the advices of Simon Bourgault-Côté and Matthieu Parenteau regarding the software NSCODE and UVLM, respectively.

CHAPTER 5 GENERAL DISCUSSION

The greatest challenge of this work regarding the experimental approach was the lack of reference parameters to begin developing the control solution. Since the flap-NES is a novel concept and analytical models in order to estimate its effect on the wing are not available, finding a starting point is complex. Furthermore, since the focus is on aeroelastic control, the experiments take place in dangerous regimes, often avoided in wind tunnel tests. This implies a double challenge: ensuring the wings perform aeroelastic instabilities within the range of speeds provided by the wind tunnel and ensuring their physical integrity. This means that before each of the campaigns reflected in this work, another “pre-campaign” was carried out in order to modify the wing and/or the safety system appropriately.

The design of the tridimensional wing was specially challenging in this sense. Initially, the intention was to build a wing which would present classic flutter similarly to the bidimensional wing. However, having a wing flexible enough to undergo flutter by coalescence and not be damaged was highly complex. The safety system is much more difficult to realize than the brake system of the 2D wing. This is why finally the tridimensional wing presents other physical phenomena which is VIV.

Once the set-ups are built and their aeroelastic phenomena observed, parametric characterization is a challenge as many parameters, some nonlinear, are involved in the complex physical phenomena which arises. This may be one of the difficulties encountered in the future development of the work once numerical simulations are run in parallel to experiments with the objective of optimizing the flap-NES.

Another challenge to consider is the design of the flap-NES on a real wing. Although the tridimensional wing presented is closer to a real wing than the initial bidimensional wing, it still has strong simplifications since, for example, it is rectangular and not swept, does not have regular control surfaces, etc. An interesting option would be to translate the flap-NES onto, for example, a prototype drone to carry out flight tests.

The scientific value of this work is the introduction of a novel passive control system. The initial hypothesis presented has been validated: the flap-NES is shown to control both aeroelastic instabilities and to mitigate vibrations. Furthermore, numerical methods are used

to analyze aeroelastic behavior and developed for the future optimization of the control solution.

As mentioned in the introduction, aeroelastic control is important both in traditional aircraft design and in keeping up with the latest advances of aeronautics. These advances include the use of more flexible materials and highly swept wings which are lighter and more efficient from an aerodynamic point of view respectively saving fuel consumption. However, these features enhance fluid structure interactions and favor aeroelastic behavior. Additionally, new disruptive aircraft and drone designs are constantly developed for new applications or more ecological air transport. The flap-NES is therefore a pertinent aeroelastic control solution to respond to aeroelastic challenges in the progress of aeronautics.

CHAPTER 6 CONCLUSION AND PERSPECTIVE

The work presented concerns the aeroelastic control of aircraft wing. An innovative solution consisting on a nonlinear secondary oscillator integrated into the wing as a flap is introduced. This new passive control concept for aircraft wings is presented, tested and its control efficiency in a range of aeroelastic phenomena is shown. This solution is called a flap-NES. The control effectiveness of the device is shown on a bidimensional wing presenting classic flutter. The presence of the control solution shows an increase of the flutter speed of 3% to 16%, with respect to the baseline system. During the post critical regime, the energy of the limit cycle oscillations experienced a decrease of up to 61% and 79% with the flap-TMD and the flap-NES respectively. The flap-NES is then tested experimentally on a three-dimensional wing presenting vortex induced vibration. Again the control capacity is shown by energy reduction of up to 90% when the flap-NES was best tuned for the system. However, the need of flap-NES optimization is highlighted by the effect of dynamic parameters in its control capacity. In order to optimize the flap-NES design, many parameters must be tested which is difficult to do experimentally. This motivates the development of a numerical approach to analyze aeroelastic behavior and as a first step to their use in future flap-NES optimization. Theodorsen model, UVLM, Euler and URANS coupled to a bidimensional airfoil are developed and tested with different aeroelastic literature cases. All methods show good agreements and it is suggested that lower fidelity methods may be used for faster initial optimization.

Future work could consist in carrying out a detailed numerical optimization of the flap-NES so that the key design parameters are identified and the control and vibration mitigation properties are maximized for a given wing and flight speed range. Apart from carrying out a numerical optimization, an analytical approach in future work could give rise to a detailed understanding of the functioning of the flap-NES and how the energy is transferred from the wing to the flap and to the fluid. This deeper understanding could benefit the design of the device.

APPENDIX A – DEVELOPMENT OF EQUATIONS OF MOTION

The equations of the bidimensional wing are hereby developed for a 3DOF general profile. This development is taken from [2].

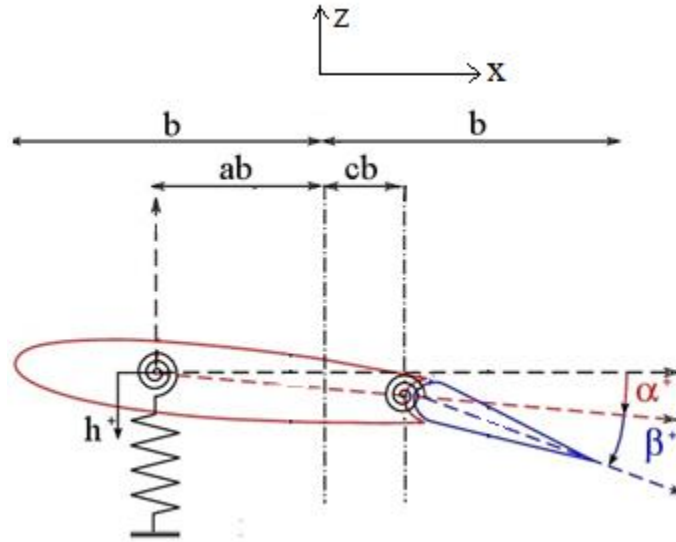


Figure A.1

The parameter shown in Figure A.1 are b , the semichord, a , the distance between the elastic axis of the profile and the midchord and c the distance from the midchord of the profile to the leading edge of the flap. In this case the leading edge of the flap is assumed to coincide with the flap's elastic axis.

The Lagrange equations for a mechanical system can be expressed:

$$\frac{d}{dt} \left(\frac{\partial T}{\partial \dot{q}_i} \right) - \frac{\partial T}{\partial q_i} = Q_i \quad (\text{A.1a})$$

$$q_i = \begin{Bmatrix} h \\ \alpha \\ \beta \end{Bmatrix} \quad (\text{A.1b})$$

Where T is the kinetic energy of the system, q_i and \dot{q}_i are the generalized displacements and velocities respectively and Q_i are the generalized forces which can be expressed as follows:

$$Q_i = \sum_{k=1}^N \frac{\partial \vec{r}_k}{\partial q_i} \vec{F}_k \quad (\text{A.2})$$

Where \vec{F}_k are the external forces acting on point $k = 1, 2, \dots, N$ of the system. Considering an aircraft wing, the system is affected by elastic Q_i^E , damping Q_i^D and aerodynamic Q_i^A . Both the elastic and damping forces are potential forces which can be expressed as:

$$Q_i^E = -\frac{\partial U}{\partial q_i} \quad (\text{A.3})$$

$$Q_i^D = -\frac{\partial D}{\partial \dot{q}_i} \quad (\text{A.3})$$

Where U and D are the potential deformation energy and the damping function. Equation A.1 therefore becomes:

$$\frac{d}{dt} \left(\frac{\partial T}{\partial \dot{q}_i} \right) - \frac{\partial T}{\partial q_i} = Q_i^E + Q_i^D + Q_i^A \quad (\text{A.3})$$

And considering that the kinetic energy only depends on the velocities and not the displacements:

$$\frac{d}{dt} \left(\frac{\partial T}{\partial \dot{q}_i} \right) + \frac{\partial U}{\partial q_i} + \frac{\partial D}{\partial \dot{q}_i} = Q_i^A \quad (\text{A.4})$$

which will give rise to a system of equations:

$$M_s \ddot{q}_i + B_s \dot{q}_i + K_s q = Q_i^A \quad (\text{A.5})$$

where M_s , B_s and K_s are the mass damping and stiffness matrices which are calculated as follows

Regarding the kinetic energy it can be expressed as:

$$dT = \frac{1}{2} (dm * 1) [\dot{h} + (x - ab)\dot{\alpha} + (x - cb)H(x - cb)\dot{\beta}]^2 \quad (\text{A.6})$$

Where x is the position along the chord and H is the so called Heaviside which is 0 for negative values and 1 for positive values. This is used to delimitate the flap. Developing the equation and integrating from the leading and the trailing edge the following expression is obtained:

$$T = \left[\frac{1}{2} M \dot{h}^2 + \frac{1}{2} I_\alpha \dot{\alpha}^2 + \frac{1}{2} I_\beta \dot{\beta}^2 + S_\alpha \dot{h} \dot{\alpha} + S_\beta \dot{h} \dot{\beta} + (I_\beta + (c - a) b S_\beta) \dot{\alpha} \dot{\beta} \right] \quad (\text{A.7})$$

M is the total of the profile:

$$M = \int_{-c/2}^{+c/2} dm \quad (\text{A.8})$$

I_α is the inertial moment of the profile with respect of the elastic axis:

$$I_\alpha = \int_{-c/2}^{+c/2} (x - ab)^2 dm \quad (\text{A.9})$$

I_β is the inertial moment of the flap with respect to its rotation axis:

$$I_\beta = \int_{-c/2}^{+c/2} (x - cb)^2 H(x - cb) dm \quad (\text{A.10})$$

S_α is the static moment of the profile with respect to its elastic axis:

$$S_\alpha = \int_{-c/2}^{+c/2} (x - ab) dm \quad (\text{A.11})$$

And S_β is the static moment of the flap with respect to its elastic axis:

$$S_\beta = \int_{-c/2}^{+c/2} (x - cb) H(x - cb) dm \quad (\text{A.12})$$

By applying LaGrange, the mass matrix M_s is calculated as:

$$M_s = \begin{pmatrix} M & S_\alpha & S_\beta \\ S_\alpha & I_\alpha & I_\beta + (c-a)bS_\beta \\ S_\beta & I_\beta + (c-a)bS_\beta & I_\beta \end{pmatrix} \quad (\text{A.12})$$

Regarding the stiffness forces k_h , k_α and k_β are the heave, pitch and flap equivalent stiffness'.

The potential energy due to elastic deformation is:

$$U = \left[\frac{1}{2}k_h h^2 + \frac{1}{2}k_\alpha \alpha^2 + \frac{1}{2}k_\beta \beta^2 \right] \quad (\text{A.13})$$

The existence of the elastic axis ensures that there is no coupling in the potential energy function. The equivalent stiffness coefficients are usually expressed as a function of the natural frequencies therefore:

$$U = \left[\frac{1}{2}M\omega_h^2 h^2 + \frac{1}{2}I_\alpha\omega_\alpha^2 \alpha^2 + \frac{1}{2}I_\beta\omega_\beta^2 \beta^2 \right] \quad (\text{A.14})$$

By applying LaGrange, the mass matrix K_s is calculated as:

$$K_s = \begin{pmatrix} M\omega_h^2 & 0 & 0 \\ 0 & I_\alpha\omega_\alpha^2 & 0 \\ 0 & 0 & I_\beta\omega_\beta^2 \end{pmatrix} \quad (\text{A.15})$$

The damping energy is obtained as:

$$D_s = M\omega_h^2\zeta_h h^2 + M\omega_\alpha^2\zeta_\alpha \alpha^2 + M\omega_\beta^2\zeta_\beta \beta^2 \quad (\text{A.16})$$

By substituting the expressions, equation A.5 becomes:

$$\begin{aligned} & \begin{bmatrix} M & S_\alpha & S_\beta \\ S_\alpha & I_\alpha & I_\beta + (c-a)bS_\beta \\ S_\beta & I_\beta + (c-a)bS_\beta & I_\beta \end{bmatrix} \begin{Bmatrix} \ddot{h} \\ \ddot{\alpha} \\ \ddot{\beta} \end{Bmatrix} + \begin{bmatrix} M\omega_h^2 & 0 & 0 \\ 0 & I_\alpha\omega_\alpha^2 & 0 \\ 0 & 0 & I_\beta\omega_\beta^2 \end{bmatrix} \begin{Bmatrix} \dot{h} \\ \dot{\alpha} \\ \dot{\beta} \end{Bmatrix} \\ & + \begin{bmatrix} 2M\omega_h^2\zeta_h & 0 & 0 \\ 0 & 2I_\alpha\omega_\alpha^2\zeta_\alpha & 0 \\ 0 & 0 & 2I_\beta\omega_\beta^2\zeta_\beta \end{bmatrix} \begin{Bmatrix} h \\ \alpha \\ \beta \end{Bmatrix} = \begin{Bmatrix} Q_h \\ Q_\alpha \\ Q_\beta \end{Bmatrix} \end{aligned} \quad (\text{A.17})$$

For simplification, the force equation is divided by Mb and the moment equations are divided by Mb^2 . The system becomes:

$$\begin{aligned}
 & \begin{bmatrix} 1 & S_\alpha/Mb & S_\beta/Mb \\ S_\alpha/Mb & I_\alpha/Mb^2 & I_\beta/Mb^2 + (c-a)S_\beta/Mb \\ S_\beta/Mb & I_\beta/Mb^2 + (c-a)S_\beta/Mb & I_\beta/Mb^2 \end{bmatrix} \begin{Bmatrix} \ddot{h}/Mb \\ \ddot{\alpha} \\ \ddot{\beta} \end{Bmatrix} \\
 & + \omega_\alpha^2 \begin{bmatrix} (\omega_h/\omega_\alpha)^2 & 0 & 0 \\ 0 & I_\alpha/Mb^2 & 0 \\ 0 & 0 & I_\beta/Mb^2(\omega_h/\omega_\beta)^2 \end{bmatrix} \begin{Bmatrix} h \\ \alpha \\ \beta \end{Bmatrix} \\
 & + \omega_\alpha^2 \begin{bmatrix} 2\zeta_h(\omega_h/\omega_\alpha)^2 & 0 & 0 \\ 0 & 2\zeta_\alpha(I_\alpha/Mb^2) & 0 \\ 0 & 0 & 2\zeta_\beta \end{bmatrix} \begin{Bmatrix} \dot{h}/b \\ \dot{\alpha} \\ \dot{\beta} \end{Bmatrix} = \begin{Bmatrix} Q_h/Mb \\ Q_\alpha/Mb^2 \\ Q_\beta/Mb^2 \end{Bmatrix} \quad (\text{A.18})
 \end{aligned}$$

This matrix system can be simplified by considering dimensionless parameters.

- $x_\alpha = S_\alpha/Mb$ which represents the dimensionless distance from the center of gravity to the elastic axis
- $x_\beta = S_\beta/Mb$ which represents the dimensionless distance from the center of gravity of the flap to the elastic axis of the flap
- $r_\alpha^2 = I_\alpha/Mb^2$ which represents the dimensionless radius of gyration of the airfoil
- $r_\beta^2 = I_\beta/Mb^2$ which represents the dimensionless radius of gyration of the flap

By substituting these parameters equation A.18 becomes:

$$\begin{aligned}
& \begin{bmatrix} 1 & x_\alpha & x_\beta \\ x_\alpha & r_\alpha^2 & r_\beta^2 + (c-a)x_\beta \\ x_\beta & r_\beta^2 + (c-a)x_\beta & r_\beta^2 \end{bmatrix} \begin{Bmatrix} \ddot{h}/Mb \\ \ddot{\alpha} \\ \ddot{\beta} \end{Bmatrix} \\
& + \omega_\alpha^2 \begin{bmatrix} (\omega_h/\omega_\alpha)^2 & 0 & 0 \\ 0 & r_\alpha^2 & 0 \\ 0 & 0 & r_\beta^2(\omega_h/\omega_\beta)^2 \end{bmatrix} \begin{Bmatrix} h \\ \alpha \\ \beta \end{Bmatrix} \\
& + \omega_\alpha^2 \begin{bmatrix} 2\zeta_h(\omega_h/\omega_\alpha)^2 & 0 & 0 \\ 0 & 2\zeta_\alpha r_\alpha^2 & 0 \\ 0 & 0 & 2\zeta_\beta(\omega_h/\omega_\beta)^2 \end{bmatrix} \begin{Bmatrix} \dot{h}/b \\ \dot{\alpha} \\ \dot{\beta} \end{Bmatrix} = \begin{Bmatrix} Q_h/Mb \\ Q_\alpha/Mb^2 \\ Q_\beta/Mb^2 \end{Bmatrix}
\end{aligned} \tag{A.19}$$

This development has considered a linear structure 3DOF structure which corresponds to the flap-TMD configuration presented in the paper. The 2DOF case would simply be:

$$\begin{aligned}
& \begin{bmatrix} 1 & x_\alpha \\ x_\alpha & r_\alpha^2 \end{bmatrix} \begin{Bmatrix} \ddot{h}/Mb \\ \ddot{\alpha} \end{Bmatrix} + \omega_\alpha^2 \begin{bmatrix} (\omega_h/\omega_\alpha)^2 & 0 \\ 0 & r_\alpha^2 \end{bmatrix} \begin{Bmatrix} h \\ \alpha \end{Bmatrix} + \omega_\alpha^2 \begin{bmatrix} 2\zeta_h(\omega_h/\omega_\alpha)^2 & 0 \\ 0 & 2\zeta_\alpha r_\alpha^2 \end{bmatrix} \begin{Bmatrix} \dot{h}/b \\ \dot{\alpha} \end{Bmatrix} \\
& = \begin{Bmatrix} Q_h/Mb \\ Q_\alpha/Mb^2 \end{Bmatrix}
\end{aligned} \tag{A.20}$$

In the case of the flap-NES configuration, an additional nonlinear term f_{nl} appears in the stiffness matrix :

$$K_s = \omega_\alpha^2 \begin{bmatrix} (\omega_h/\omega_\alpha)^2 & 0 & 0 \\ 0 & r_\alpha^2 & 0 \\ 0 & 0 & r_\beta^2 + f_{nl}(\omega_h/\omega_\beta)^2 \end{bmatrix} \quad (\text{A.21})$$

$$f_{nl} = r_\beta^2 \eta_\beta \beta^3 \quad (\text{A.22})$$

Where η_β is the ratio of the cubic to the linear stiffness.

APPENDIX B – THEODORSEN MODEL

The aerodynamic functions given by Theodorsen model in terms of reduced frequency are given as follows:

$$\begin{aligned} \tilde{Q}_h(k) = -2\pi q_\infty b \left[\frac{t_0^2 \ddot{h}}{b} + t_0 \dot{\alpha} - (c-a)t_0^2 \ddot{\alpha} - \frac{T_4}{\pi} t_0 \dot{\beta} - \frac{T_1}{\pi} t_0^2 \ddot{\beta} \right] - 4\pi q_\infty b C(k) \left[\frac{t_0 \dot{h}}{b} \right. \\ \left. + \alpha + (0.5 - a)t_0 \dot{\alpha} + \frac{T_{10}}{\pi} \beta + \frac{T_{11}}{2\pi} t_0 \dot{\beta} \right] \end{aligned} \quad (\text{B.1})$$

$$\begin{aligned} \tilde{Q}_\alpha(k) = -2\pi q_\infty b^2 \left[-(c-a) \frac{t_0^2 \ddot{h}}{b} + (0.5 - (c-a))t_0 \dot{\alpha} + (0.165 + (c-a)^2)t_0^2 \ddot{\alpha} \right. \\ \left. + \frac{T_4 + T_{10}}{\pi} \beta + \frac{T_1 - T_8 - (c-a)T_4 + 0.5T_{11}}{\pi} t_0 \dot{\beta} \right. \\ \left. - \frac{(c-a)T_1 + T_7}{\pi} t_0^2 \ddot{\beta} \right] \\ + 4\pi b^2 q_\infty (0.5 + (c-a))C(k) \left[\frac{t_0}{b} + \alpha + (0.5 - (c-a))t_0 \dot{\alpha} + \frac{T_{10}}{\pi} \beta \right. \\ \left. + \frac{T_{11}}{2\pi} t_0 \dot{\beta} \right] \end{aligned} \quad (\text{B.2})$$

$$\begin{aligned} \tilde{Q}_\beta(k) = -q_\infty b^2 \left[-2T_1 \frac{t_0^2 \ddot{h}}{b} - 2(T_1 + T_4(0.5 - (c-a)) + 2T_9)t_0 \dot{\alpha} + 4T_{13}t_0^2 \ddot{\alpha} + \right. \\ \left. \frac{2}{\pi}(T_5 - T_4T_{10})\beta - \frac{T_4T_{11}}{\pi} t_0 \dot{\beta} - 2\frac{T_3}{\pi} t_0^2 \ddot{\beta} \right] - 2q_\infty b^2 T_{12} C(k) \left[\frac{t_0 \dot{h}}{b} + \alpha + (0.5 - \right. \\ \left. (c-a))t_0 \dot{\alpha} + \frac{T_{10}}{\pi} \beta + \frac{T_{11}}{2\pi} t_0 \dot{\beta} \right] \end{aligned} \quad (\text{B.3})$$

The Theodorsen function $C(k)$ is given as a function of Hankel functions:

$$C(k) = \frac{H_1^{(2)}(k)}{H_1^{(2)}(k) + iH_0^{(2)}(k)} \quad (\text{B.4})$$

Where $H_n^{(2)}(k)$ are Hankel functions of second order n , which can be expressed as Bessel functions:

$$H_n^{(2)}(k) = J_n(k) - iY_n(k) \quad (\text{B.5})$$

Functions T_n depend on the geometric characteristic of the wing and can be expressed as:

$$T_1 = -\frac{1}{3}(2 + c^2)\sqrt{1 - c^2} + c * \arccos(c) \quad (\text{B.6})$$

$$T_2 = c(1 - c^2) - (1 + c^2)\sqrt{1 - c^2} \arccos(c) + c(\arccos(c))^2 \quad (\text{B.7})$$

$$T_3 = -\left(\frac{1}{8} + c^2\right) (\arccos(c))^2 + \frac{1}{4}c(7 + 2c^2)\sqrt{1 - c^2} \arccos(c) - \frac{1}{8}(1 - c^2)(5c^2 + 4) \quad (\text{B.8})$$

$$T_4 = -\arccos(c) + c\sqrt{1 - c^2} \quad (\text{B.9})$$

$$T_5 = -(1 - c^2) - (\arccos(c))^2 + 2c\sqrt{1 - c^2} \arccos(c) \quad (\text{B.10})$$

$$T_6 = T_2 \quad (\text{B.11})$$

$$T_7 = -\left(\frac{1}{8} + c^2\right) \arccos(c) + \frac{1}{8}c(7 + 2c^2)\sqrt{1 - c^2} \quad (\text{B.12})$$

$$T_8 = -\frac{1}{3}(2c^2 + 1)\sqrt{1 - c^2} + c * \arccos(c) \quad (\text{B.13})$$

$$T_9 = \frac{1}{2} \left[\frac{1}{3}(1 - c^2)^{3/2} + aT_4 \right] \quad (\text{B.14})$$

$$T_{10} = \sqrt{1 - c^2} + \arccos(c) \quad (\text{B.15})$$

$$T_{11} = (1 - 2c) \arccos(c) + (2c + 1)\arccos(c) \quad (\text{B.16})$$

$$T_{12} = (2 + c)\sqrt{1 - c^2} - (2c + 1)\arccos(c) \quad (\text{B.17})$$

$$T_{13} = -\frac{1}{2}(T_7 + (c - a)T_1) \quad (\text{B.18})$$

$$T_{14} = \frac{1}{16} + \frac{1}{2} * a * c \tag{B.19}$$

REFERENCES

1. Collar, A.R., *The first fifty years of aeroelasticity*. Aerospace, 1978. **2**(5): p. 12-20.
2. Garcia-Fogeda Nunez, P. and F. Arevalo Lozano, *Introduccion a la aeroelasticidad*, ed. S.L. Ibergarceta publicaciones. 2014, Madrid.
3. Afonso, F., et al., *A review on non-linear aeroelasticity of high aspect-ratio wings*. Progress in Aerospace Sciences, 2017. **89**.
4. Raghavan, B. and M. Patil, *Flight Dynamics of High Aspect-Ratio Flying Wings*, in *AIAA Atmospheric Flight Mechanics Conference and Exhibit*. 2006: Keystone, Colorado.
5. Sicard, J. and J. Sirohi, *Modeling of the Large Torsional Deformation of an Extremely Flexible Rotor in Hover*. AIAA Journal, 2014. **52**: p. 1604-1615.
6. Noll, T.E., et al., *Investigation of the Helios Prototype Aircraft Mishap in Mishap Report*. 2004, NASA.
7. Arévalo, F., *Aeroelasticidad de una aeronave en presencia de no linealidades estructurales concentradas*, in *Ingenieria Aeronautica*. 2008, E.T.S.I. Aeronáuticos (UPM): Madrid.
8. Strogatz, S.H., *Nonlinear Dynamics and Chaos with application in physics, biology, chemistry and engineering*. 2015: Boulder, CO :Westview Press, a member of the Perseus Books Group.
9. Dimitriadis, G., *Introduction to Nonlinear Aeroelasticity* ed. J.W.S. Ltd. 2017.
10. Sandford, M.C., I. Abel, and D.L. Gray, *Development and demonstration of a flutter-suppression system using active controls*. NASA Technical Report ed. S. Mechanics. 1975.
11. Borglund, D. and J. Kuttenukeuler, *Active wing flutter suppression using a trailing edge flap*. Journal of Fluids and Structures, 2002. **16**(3): p. 271-294.
12. Yu, M. and H. Hu, *Flutter control based on ultrasonic motor of a two-dimensional airfoil section*. Journal of Fluids and Structures, 2012. **28**: p. 89-102.
13. Han, J.H., J. Tani, and J. Qiu, *Active flutter suppression of a lifting surface using piezoelectric actuation and modern control theory*. Journal of Sound and Vibration, 2006. **291**: p. 706-722.
14. Moses, R.W. *Active vertical tail buffeting alleviation on an f/a-18 model in a wind tunnel*. in *Proceedings of the Second Joint NASA/FAA/DOD Conference on Aging Aircraft*. 1998. Williamsburg, VA.
15. Filho, A., et al., *Flutter suppression of plates using passive constrained viscoelastic layers*. Mechanical Systems and Signal Processing, 2016. **79**.
16. Malher, A., *Amortisseurs passifs non linéaires pour le contrôle de l'instabilité de flottement*, in *Mecanique*. 2016, Université de Paris-Saclay: France.

17. Mesenguer, J., et al., *Aerodinamica Civil: efectos del viento en edificaciones y esttructuras*. 2013: Ibergarceta Publicaciones, SL, Madrid.
18. Hartog, J.P.D., *Mechanical vibrations*, ed. B.C. McGraw-Hill. 1934, New York.
19. Asami, T. and O. Nishihara, *Closed-form exact solution to h_{∞} optimization of dynamic vibration absorbers (application to different transfer functions and damping systems)*. Journal of Vibration and Acoustics, 2003. **125**(3): p. 398–405.
20. Habib, G. and G. Kerschen, *Suppression of limit cycle oscillations using the nonlinear tuned vibration absorber*. Proceedings mathematical, physical, and engineering sciences 2015. **471**.
21. Verstraelen, E., *Aeroelastic limit cycle oscillations mitigation using linear and nonlinear tuned mass dampers*, in *Department of Aerospace and Mechanical engineering*. 2018, University of Liège.
22. Lee, Y.S., et al., *Passive non-linear targeted energy transfer and its applications to vibration absorption: a review*. Proceedings of the Institution of Mechanical Engineers, Part K: Journal of Multi-body Dynamics., 2008. **222**(2): p. 77-134.
23. Vakakis, A.F., et al., *Nonlinear Targeted Energy Transfer in Mechanical and Structural Systems. 2 Vols*. Solid Mechanics and its Applications, 2009. **156**.
24. E. Gourdon, N.A.A., C.A. Taylor, C.H. Lamarque, S. Pernot, *Nonlinear energy pumping under transient forcing with strongly nonlinear coupling: Theoretical and experimental results*. Journal of Sound and Vibration, 2007. **300**(3-5): p. 522-551.
25. Georgiades, F. and A.F. Vakakis, *Passive targeted energy transfers and strong modal interactions in the dynamics of a thin plate with strongly nonlinear attachments*. International Journal of Solids and Structures, 2009. **46**(11-12): p. 2330-2353.
26. Nucera, F., et al., *Application of broadband nonlinear targeted energy transfers for seismic mitigation of a shear frame: Experimental results*. Journal of Sound and Vibration, 2008. **313**(1): p. 57-76.
27. Ahmadabadi, Z.N. and S.E. Khadem, *Nonlinear vibration control and energy harvesting of a beam using a nonlinear energy sink and a piezoelectric device*. Journal of Sound and Vibration, 2014. **333**(19): p. 4444-4457.
28. Gourc, E., *Etude du contrôle passif par pompage énergétique sous sollicitation harmonique : Analyses théoriques et expérimentales*, in *Génie Mécanique, Mécanique des Matériaux* 2013, INSA: Toulouse.
29. Mehmood, A., A.H. Nayfeh, and M.R. Hajj, *Effects of a non-linear energy sink (NES) on vortex-induced vibrations of a circular cylinder*. Nonlinear Dynamics, 2014. **77**(3): p. 667-680.
30. Guo, H., et al., *Aeroelastic supression of an airfoil with control surface using nonlinear energy sink*. Nonlinear Dynamics, 2018. **94**: p. 857–872.
31. Bichiou, Y., M.R. Hajj, and A.H. Nayfeh, *Effectiveness of a nonlinear energy sink in the control of an aeroelastic system*. Nonlinear Dynamics, 2016. **86**: p. 2161–2177.

32. Yan, Z., S.A. Ragab, and M.R. Hajj, *Passive control of transonic flutter with a nonlinear energy sink*. Nonlinear Dynamics, 2018. **91**(1): p. 577-590.
33. Tian, W., et al., *Passive control of nonlinear aeroelasticity in hypersonic 3-D wing with a nonlinear energy sink*. Journal of Sound and Vibration, 2019. **462**.
34. Hubbard, S.A., et al., *Transonic aeroelastic instability suppression for a swept wing by targeted energy transfer*. Journal of Aircraft, 2014. **51**(5): p. 1467-1482.
35. Spalart, P.R. and V. Venkatakrishnan, *On the role and challenges of CFD in the aerospace industry*. The Aeronautical Journal, 2016. **120**(1223): p. 209–232.
36. Farhat, C. and M. Lesoinne, *Two efficient staggered algorithms for the serial and parallel solution of three-dimensional nonlinear transient aeroelastic problems*. Computer Methods in Applied Mechanics and Engineering, 2000. **182**: p. 499–515.
37. Beckert, A. and H. Wendland, *Multivariate interpolation for fluid-structure-interaction problems using radial basis functions*. 2001. **5**(2): p. 125-134.
38. Farhat, C., M. Lesoinne, and P. Le Tallec, *Load and motion transfer algorithms for fluid/structure interaction problems with non-matching discrete interfaces: Momentum and energy conservation, optimal discretization and application to aeroelasticity*. Computer Methods in Applied Mechanics and Engineering, 1998. **157**(1-2): p. 95-114.
39. Piperno, S., C. Farhat, and B. Larrouturou, *Partitioned procedures for the transient solution of coupled aroelastic problems Part I: Model problem, theory and two-dimensional application*. Computer Methods in Applied Mechanics and Engineering, 1995. **124**: p. 79-112.
40. Farhat, C. and M. Lesoinne, *Improved staggered algorithms for the serial and parallel solution of three-dimensional non linear transient aeroelastic problems*. Computer Methods in Applied Mechanics and Engineering, 2000. **182**(3): p. 499-515.
41. Amar, L., *Nonlinear passive control of an aeroelastic airfoil, simulations and Experimentations*. 2017, Toulouse University.
42. Theodorsen, T., *General theory of aerodynamic instability and mechanism of flutter*. NACA Technical Report, 1935. **496**.
43. Sears, W.R., *Some aspects of non-stationary airfoil theory and its practical application*. Journal of the Aeronautical Sciences, 1941. **8**: p. 104-108.
44. O'Neil, T., H. Gilliatt, and T. Strganac, *Investigations of aeroelastic response for a system with continuous structural nonlinearities*, in *37th Structure, Structural Dynamics and Materials Conference*. 1996, AIAA: Salt Lake City,UT,U.S.A. p. 1996-1390.
45. Conner, M.D., et al., *Nonlinear behavior of a typical airfoil section with control surface freeplay: a numerical and experimental study*. . Journal of Fluids and Structures, 1997. **11**(1): p. 89-109.
46. Jones, R.T., *Operational treatment of the nonuniform-lift theory in airplane dynamics*. NACA Technical Notes, 1938. **667**.
47. Wagner, H., *Über die Entstehung des dynamischer Auftriebes von Tragflügeln*. Z. angew. Math. u. Mech. , 1925. **5**: p. 17-35.

48. Fung, Y.C., *An Introduction to the Theory of Aeroelasticity*, ed. I. John Wiley and Sons. 1955, New York, NY.
49. Erickson, L.L., *Panel methods: An introduction*. NASA Technical Paper 2995, 1990.
50. Hess, J.L. and A.M.O. Smith, *Calculation of non-lifting potential flow about arbitrary three dimensional bodies*. Journal of Ship Research, 1964. **8**(4).
51. Albano, E. and P. William, *A doublet-lattice method for calculating lift distributions on oscillating surfaces in subsonic flows*. AIAA Journal, 1969. **7**(2): p. 279-285.
52. Rodden, W.P., *The Development of the Doublet-Lattice Method*, in *International Forum on Aeroelasticity and Structural Dynamics*. 1997.
53. Murua, J., R. Palacios, and J.M.R. Graham, *Applications of the unsteady vortex-lattice method in aircraft aeroelasticity and flight dynamics*. Progress in Aerospace Sciences, 2012. **55**: p. 46-72.
54. Katz, J. and A. Plotkin, *Low-Speed Aerodynamics*. Cambridge University Press. 2001.
55. Parenteau, M. and E. Laurendeau, *A general modal frequency-domain vortex lattice method for aeroelastic analyses*. Journal of Fluids and Structures, 2020. **99**.
56. Anderson, J.D., *Fundamentals of aerodynamics*, ed. T.M.-H. Education. 2010.
57. Dadone, A., B. Fortunato, and A. Lippolis, *A fast Euler solver for two- and three-dimensional internal flows*. Computers & Fluids, 1989. **17**(1): p. 25-37.
58. Kwak, D., et al., *A three-dimensional incompressible Navier-Stokes flow solver using primitive variables*. AIAA, 1986. **24**(3): p. 390-396.
59. Spalart, P.R., *Philosophies and fallacies in turbulence modeling*. Progress in Aerospace Sciences, 2015. **74**: p. 1–15.
60. Jameson, A., *Time dependent calculations using multigrid, with applications to unsteady flows past airfoils and wings*. AIAA, 1991.
61. Simpson, R.J.S. and R. Palacios, *Numerical aspects of nonlinear flexible aircraft flight dynamics modeling*, in *54th AIAA/ASME/ASCE/AHS/ASC Structures, Structural Dynamics, and Materials Conference*. 2013: Boston, Massachusetts.
62. Zhiyin, Y., *Large-eddy simulation: Past, present and the future*. Chinese Journal of Aeronautics, 2015. **28**(1): p. 11-24.
63. Sagaut, P., *Large Eddy Simulation for Incompressible Flows: An Introduction*. Scientific Computation. 2005: Springer.
64. Moin, P. and K. Mahesh, *Direct numerical simulation: A Tool in Turbulence Research*. Annual Review of Fluid Mechanics, 1998. **30**: p. 539-578.
65. Garrick, I.E. and W.H. Reed, *Historical Development of Aircraft Flutter*. Journal of Aircraft, 1981. **18**(11): p. 897-912.
66. Bisplinghoff, R.L., H. Ashley, and R.L. Halfman, *Aeroelasticity*. New York: Dover Publications, 1996.

67. Fernandez-Escudero, C., et al., *Comparison of low, medium and high fidelity numerical methods for unsteady aerodynamics and nonlinear aeroelasticity*. Journal of Fluids and Structures, 2019. **91**.
68. Rao, V.M., et al., *Adaptive aeroelastic vibration suppression of a supersonic airfoil with flap*. Aerospace Science and Technology, 2006. **10**(4): p. 309-315.
69. Borglund, D. and J. Kuttentkeuler, *Active wing flutter suppression using a trailing edge flap*. Journal of Fluids and Structures., 2002.
70. Yu, M. and H. Hu, *Flutter control based on ultrasonic motor of a two-dimensional airfoil section*. Journal of Fluids and Structures, 2012. **28:89 - 102**.
71. Tsushima, N. and W. Su, *Flutter suppression for highly flexible wings using passive and active piezoelectric effects*. Aerospace Science and Technology, 2017. **65**: p. 78-89.
72. Moses, R.W., *Active vertical tail buffeting alleviation on an f/a-18 model in a wind tunnel*. 1999.
73. Cunha-Filho, A.G., et al., *Flutter suppression of plates subjected to supersonic flow using passive constrained viscoelastic layers and Golla–Hughes–McTavish method*. Aerospace Science and Technology, 2016. **52**: p. 70-80.
74. Malher, A., *Amortisseurs passifs non linéaires pour le contrôle de l'instabilité de flottement*, in *Mécanique*. 2016, Université de Paris-Saclay: France.
75. Jain, P.C., *Tuned mass dampers for flight vehicle components subjected to rocket noise*. Aerospace Science and Technology, 2011. **15**(3): p. 175-182.
76. Carpineto, N., W. Lacarbonara, and F. Vestroni, *Hysteretic tuned mass dampers for structural vibration mitigation*. Journal of Sound and Vibration, 2014. **333**(5): p. Journal of Sound and Vibration.
77. Gutierrez Soto, M. and H. Adeli, *Tuned Mass Dampers*. Archives of Computational Methods in Engineering, 2013. **20**(4).
78. Habib and Kerschen, *Suppression of limit cycle oscillations using the nonlinear tuned vibration absorber*. In Proc. R. Soc. A. The Royal Society 2015. **471**.
79. Lee, et al., *Passive non-linear targeted energy transfer and its applications to vibration absorption: a review*. Proceedings of the Institution of Mechanical Engineers, Part K: Journal of Multi-body Dynamics., 2008.
80. Pennisi, G., et al., *Experimental investigation and analytical description of a vibro-impact NES coupled to a single-degree-of-freedom linear oscillator harmonically forced*. Nonlinear Dynamics, 2017. **88**: p. 1769–1784
81. Vakakis, A.F., et al., *Nonlinear Targeted Energy Transfer in Mechanical and Structural Systems*. Solid Mechanics and its Applications, ed. Springer. 2008.
82. Georgiades, F. and A. Vakakis, *Passive targeted energy transfers and strong modal interactions in the dynamics of a thin plate with strongly nonlinear attachments*. International Journal of Solids and Structures, 2009. **46**(11-12): p. 2330-2353.

83. Nucera, F., et al., *Application of broadband nonlinear targeted energy transfers for seismic mitigation of a shear frame: Experimental results*. Journal of Sound and Vibration, 2008. **313**(1-2): p. 57-76.
84. Ahmadabadi, Z. and S. Khadem, *Nonlinear vibration control and energy harvesting of a beam using a nonlinear energy sink and a piezoelectric device*. Journal of Sound and Vibration, 2014. **333**(19): p. 4444-4457.
85. Gourc, E., *Etude du contrôle passif par pompage énergétique sous sollicitation harmonique : Analyses théoriques et expérimentales*, in *Mechanic Engineering*. 2013, INSA: Toulouse.
86. Mehmood, A., A. Nayfeh, and M. Hajj, *Effects of a non-linear energy sink (NES) on vortex-induced vibrations of a circular cylinder*. Nonlinear Dynamics, 2014. **77**(3): p. 667-680.
87. Andrienne, T., et al., *Energy harvesting from different aeroelastic instabilities of a square cylinder*. Journal of Wind Engineering and Industrial Aerodynamics, 2018. **172**(164-169, ISSN 0167-6105).
88. Selwanis, M., et al., *Wind tunnel demonstration of galloping mitigation with a purely nonlinear energy sink*. . 2020.
89. Bernhammer, L.O., et al., *Aeroelastic Control Using Distributed Floating Flaps Activated by Piezoelectric Tabs*. Journal of Aircraft, 2013. **50**(3): p. 732-740.
90. Zhang, S. and Z. Wang, *Dynamic Distributed Morphing Control of an Aeroelastic Wing for a Small Drone*. 2019. **56**(6): p. 2324-2341.
91. Gourc, E., et al., *Experimental Investigation and Design Optimization of Targeted Energy Transfer Under Periodic Forcing*. Journal of Vibration and Acoustics, 2014. **136**(2).
92. Yin, X., X. Song, and Y. Liu, *Vibration Suppression of Wind/Traffic/Bridge Coupled System Using Multiple Pounding Tuned Mass Dampers (MPTMD)*. 2019. **19**(5).
93. Sean, A., et al., *Targeted Energy Transfer Between a Model Flexible Wing and Nonlinear Energy Sink*. Journal of Aircraft, 2010. **47**: p. 1918-1931.
94. Ahmadabadi, Z.N. and S.E. Khadem, *Nonlinear vibration control and energy harvesting of a beam using a nonlinear energy sink and a piezoelectric device*. Journal of Sound and Vibration, 2014. **333**: p. 4444-4457.
95. Afonso, F., et al., *A review on non-linear aeroelasticity of high aspect-ratio wings*. Progress in Aerospace Sciences, 2017. **89**: p. 40-57.
96. Breitbach, E., *Effects of structural non-linearities on aircraft vibration and flutter*, in *Advisory Group for Aerospace Research and Development 1978*: Neuilly-Sur-Seine.
97. Thomas, J.P., E.H. Dowell, and K.C. Hall, *Nonlinear Inviscid Aerodynamic Effects on Transonic Divergence, Flutter and Limit-Cycle Oscillations*. AIAA Journal, 2012. **40**(4): p. 638-646.
98. Dowell, E., J. Edwards, and T. Strganac, *Nonlinear Aeroelasticity*. Journal of Aircraft, 2003. **40**(5): p. 857-874.

99. Lee, B.H.K., Y.S. Price, and Y.S. Wong, *Nonlinear aeroelastic analysis of airfoils: bifurcation and chaos*. Progress in Aerospace Sciences, 1999. **35**(3): p. 205-334.
100. Zhao, Y.H. and H. Hu, *Aeroelastic analysis of a non-linear airfoil based on unsteady vortex lattice model*. Journal of Sound and Vibration, 2004. **276**: p. 491-510.
101. Kholodar, D.B., *Nature of Freeplay-Induced Aeroelastic Oscillations*. Journal of Aircraft, 2014. **51**: p. 571-583.
102. Thomson, W.T., *Theory of vibration with applications*. CRC Press. 2018.
103. Edwards, J.W., *Unsteady aerodynamic modeling for arbitrary motions*. AIAA Journal, 1979. **17**(4): p. 365-374.
104. Levesque, A.T., et al., *An overset grid 2D/Infinite swept wing URANS solver using Recursive Cartesian Virtual Grid method*, in *53rd AIAA Aerospace Sciences Meeting*. 2015, AIAA: Kissimmee, Florida.
105. Spalart, P.R. and S.R. Allmaras, *A one-equation turbulence model for aerodynamic flows*, in *30th Aerospace Sciences Meeting and Exhibit 1992*: Reno, NV, U.S.A.
106. Yang, S., et al., *Computation of the Flows over Flapping Airfoil by the Euler Equations*, in *43rd AIAA Aerospace Sciences Meeting and Exhibit*. 2005.
107. Sicot, F., et al., *Time-Domain Harmonic Balance Method for Turbomachinery Aeroelasticity*. AIAA Journal, 2014. **52**(1): p. 62-71.
108. Murua, J., *Flexible aircraft dynamics with a geometrically-nonlinear description of the unsteady aerodynamics*, in *Department of Aeronautics*. 2012, Imperial College London.